A MASTER–SLAVE SYNCHRONIZATION METHOD FOR A SAW BASED ON–BOARD PROCESSING SATELLITE SYSTEM

by

Ning Zhang

A thesis submitted to
the Department of Electrical and Computer Engineering
in conformity with the requirements
for the degree of Doctor of Philosophy

Queen's University
Kingston, Ontario, Canada
September 1998

0-612-35987-5

Abstract

Synchronized FDMA inputs from earth terminals to a SAW based on–board, multicarrier, demodulator (MCD) reduces overall satellite system complexity. The synchronization problem of multiple uplink terminals to a geosynchronous (GEO) regenerative satellite processor, with a time–division multiplexed (TDM) downlink, is studied in this thesis. The method considered uses channel probing to provide an uplink propagation delay estimate which can be used by a ground terminal to adjust its transmitter clock phase to ensure synchronization to the satellite clock when the signal is received by the on–board receiver. This method is named transmitter timing recovery and the central concept is to provide global synchronization without the use of a satellite based beacon signal. The method used is based on master–slave synchronization theory, where the satellite is regarded as the master and the terminal as the slave.

Two possible timing offset indicators, the estimated bit error probability and the estimated uplink signal amplitude, which can be used to calculate the timing offset, are identified and examined in the thesis. The estimation methodology follows the maximum likelihood estimation (MLE) principle.

The uplink bit error probability can be estimated to an accuracy of $1/16th$ of a symbol interval with probability larger than 0.9 with at least a 4000–symbol long probing sequence for SNR = 4 dB. The uplink signal amplitude is a better indicator in terms of estimation efficiency because in order to get the same estimation probability it requires a 100–symbol probing sequence with operation SNR > 5 dB. The detected uplink signal amplitude is

estimated at the output of an on–board MCD. A properly designed probing signal provides a linear relationship of amplitude vs. timing offset on the average. MCD outputs with AWGN at the input are studied in detail. The magnitude distribution follows a Rician pdf. A magnitude estimate is sent to the original terminal in order to have a time–delay estimate that is free of the phase offsets in the MCD.

The performance measures used for the time–delay estimate are (1) the pdf of this estimate, (2) the variance of this estimate, and (3) the number of probing symbols required to get less than 0.5 dB penalty of E_b/N_0 in the on–board processor bit error rate due to timing errors with the given timing resolution of $T/16$. For the worst–case of a one–half symbol time of error, the magnitude estimate algorithm produced satisfactory synchronization 98% of the time. This result is for a 10 dB link E_b/N_0 and use of a 4–bit quantizer to transmit the timing error estimate on the downlink TDM channel.

A computer simulation of a complete processing satellite and a communicating terminal shows the interactions between the recovered downlink clock and uplink timing estimate. This simulation includes all aspects of timing recovery, carrier recovery, filtering and data detection in both the terminal and the satellite on–board processor. The delay estimate algorithm is proved workable in this practical system configuration, whereas, in earlier work in this thesis, it could be analysed in restricted situations. The requirement for the downlink to allow the proper operation of the uplink delay estimate is obtained from simulation. The simulated BER results show that with this transmitter timing recovery mechanism used, no significant SNR penalty can be observed with a probing sequence of length 100-symbols.

Acknowledgements

I would like to take this opportunity to thank my supervisor Dr. Peter J. McLane, for all his help, without which I could not have reached this stage of my thesis work. His comments, suggestions, and guidance are invaluable. He is, if not more than, truly a supervisor in all sense of the word being a good listener, guide, and source of insight and encouragement. I am grateful that I could conduct some of my thesis work off–campus at the Communications Research Centre (CRC) from where I obtained direct exposure to the latest developments of satellite communications technology and in particular, SAW processor development.

I would also like to acknowledge financial support from Com Dev Ltd. of Cambridge, Ontario, the Federal Department of Communications and Queen's University. I would like to express my appreciation to Mr. Chun Loo for granting me a platform for computer simulation at CRC and providing me helpful guidance in my research work. Dr. Norman Secord, formerly of CRC, and now with Nortel is also thanked for discussions on synchronization to satellite based SAW implemented MCDs.

I would like to thank the computer managers of this department and all my friends, for all the help and support which carried me through this work.

Specially, I would like to thank Prof. Blostein for suggesting and outlining the material in the Appendix B.

On top of all, my gratitude to my wife Lintao for her loving support and constant encouragement without that the work can not possibly be done.

Contents

List of Figures

List of Tables

List of Symbols and Abbreviations

AWGN	Additive White Gaussian Noise
A/D	Analog to Digital Conversion
ASK	Amplitude Shift Keying
BER	Bit Error Rate
BPSK	Binary Phase Shift Keying
BSC	Binary Symmetric Channel
BW	Bandwidth
CDMA	Code Division Multiple Access
CFT	Chirp Fourier Transform
CMC	Convolve Multiply Convolve
CODEC	COder/DECoder
CR	Cramér–Rao
CRB	Cramér–Rao Bound
D/A	Digital to Analog Conversion
dB	decibel
DD	Decision–Directed
DLL	Delay Locked Loop
DPLL	Digital Phase Locked Loop
DSC	Discrete Symmetrical Channel
DSP	Digital Signal Processing

DQPSK	Differential QPSK
DSAM	Detected Signal Amplitude Method
EPM	Error Probability Method
FDM	Frequency Division Multiplexing
FDMA	Frequency Division Multiple Access
FIR	Finite Impulse Response
FT	Fourier Transform
GEO	Geosynchronous Earth Orbit
HPA	High Power Amplifier
IC	Integrated Circuit
ICI	Inter–Channel Interference
IF	Intermediate Frequency
IIR	Infinite Impulse Response
ISI	Inter–Symbol Interference
Kbps	Kilo–bits per second
LEO	Low Earth Orbit
LF	Loop Filter
Mbps	Mega–bits per second
MCD	MultiCarrier Demodulator
MCM	Multiply Convolve Multiply
MEO	Medium altitude Earth Orbit
MF	Matched Filter
MHz	Mega Hertz
ML	Maximum Likelihood
MLE	Maximum Likelihood Estimate
MSE	Mean Square Error

NRZ	Non Return to Zero
PCM	Pulse Code Modulation
PCN	Personal Communication Networks
PCS	Personal Communication Services
PD	Phase Detector
PDF/Pdf/pdf	probability density function
PLL	Phase Locked Loop
PN	Pseudo Noise
PSK	Phase Shift Keying
PSTN	Public Switched Telephone Network
QPSK	Quadrature Phase Shift Keying
RC	Raised Cosine
RF	Radio Frequency
RHS	Right Hand Side
RMS	Root–Mean–Square
Rx	Receiver
SAW	Surface Acoustic Wave
SCPC	Single Channel Per Carrier
SNR	Signal–to–Noise Ratio
SNRE	Effective SNR
TDM	Time Division Multiplexing
TDMA	Time Division Multiple Access
TWTA	Travelling Wave Tube Amplifier
Tx	Transmitter
TxTR	transmitter timing recovery
USEQ	Uplink Signal Estimated and Quantized

USQE	Uplink Signal Quantized and Estimated
VCO	Voltage Controlled Oscillator
VLSI	Very Large Scale Integrated circuit
VSAT	Very Small Aperture Terminal

a	normalised effective signal amplitude without noise
$\widehat{a}$	estimate of a
A	input signal amplitude without noise
$A(\delta_d)$	function for correcting delay error bias
α	probability of incorrect estimate
$\alpha_{k,m}$	modulating phase in the m-th symbol interval for the k-th channel
B	signal bandwidth in Hertz
D	Symbol timing offset
$\widehat{D}$	Estimate of the symbol timing offset
$e(n)$	error signal from timing detector
$E[x]$	expectation of random variable x
E_b	energy per bit
E_b/N_0	energy per bit to noise spectral density ratio
$\mathrm{erfc}(x)$	complementary error function
f	frequency
$\overline{E}_k$	Average symbol energy
Δf	frequency difference between carrier and local oscillator
$F(x)$	Fourier transform of function $f(t)$
$f_X(x)$	probability density function
$g(p)$	function that maps p to timing offset D
$h_0(t)$	time response of a SAW device

$H(f)$	frequency response of the pulse shaping filter
$H(z)$	loop filter transfer function
I_k	symbol integral
$I_{k-\frac{1}{2}}$	timing integral
I_l	lower limit of CRB confidence interval
I_R	Cramér–Rao bound
I_u	upper limit of CRB confidence interval
l_i	quantization levels
$l(i)$	local synchronization PN sequence
$L(x)$	likelihood function
λ	normalised timing offset
M	number of quantization levels
n	sample value of Gaussian random variable
N	length of probing sequence (symbols)
N_e	number of errors in a received probing sequence
N_0	one-sided noise power spectrum
p	bit error probability
$\bar{p}$	average bit error probability due to timing offset
p_d	downlink bit error probability
p_u	uplink bit error probability
$p(k)$	probability mass function
$P(X=k)$	discrete probability at $X=k$
P_e	bit error rate
P_{diff}	bit error rate with differential encoding
q	quantization step size
$Q(x)$	Q–function, defined as $Q(x)=\frac{1}{\sqrt{2\pi}}\int_x^\infty \exp(-\frac{t^2}{2})dt=\frac{1}{2}\text{erfc}(x)$

$Q'(x)$	Differentiation of $Q(x)$ with respect to x
r	random signal magnitude with Rician distribution
$r(i)$	received signal samples
$\mathrm{Sa}(x)$	sinc function defined as $\mathrm{Sa}(x) = \frac{\sin x}{x}$
$\tilde{S}_{km}(\tau)$	output of the k-th channel for the m-th input symbol
σ^2, σ_x^2	variance of Gaussian random variable
σ_z^2	variance of an estimate
θ	phase of the received signal
Θ	uniformly distributed phase angle
Φ	phase information in the received signal
s	variable of Laplace transform
τ	propagation delay
τ_i	LF parameters
T	symbol period in seconds
t_0	sampling instant
T_{off}	true timing offset
T_e	estimated timing offset
$\overline{T}_e$	mean of the estimated timing offset
T_r	residual timing offset
$\overline{T}_r$	mean of the residual timing offset
u	half of the estimated confidence interval
$u_{\alpha/2}$	half of the normalised estimated confidence interval
μ	chirp rate of a SAW device in rad/s
ω	angular frequency
$\mathrm{Var}[x]$	variance of random variable x
$w(t)$	weighing function applied to the impulse response of a SAW device

x	sample value of the received signal
X	random variable of Gaussian or geometric type
$X_{corr}(t)$	cross correlation function between local and incoming sequence
z	Z–transform variable

Chapter 1

Introduction

1.1 Motivation

Around the world, wireless personal communication services are expanding [1]. It is predicted that in ten years, 60 percent of all communications will be wireless [2]. The ultimate goal of personal communication systems is to allow people to access truly global mobile communications services through a hand–held digital terminal [3]. Such terminals will be able to transmit not only voice but also a variety of new digital services, such as multimedia [4]. Demands for digital transmission will be increasing in future telecommunication networks and such networks must also be very versatile in order to handle the requirement of the diverse services that could be introduced. There is no doubt that optical fiber communication systems are the future mode of transmission for public switched telecommunication networks (PSTN), especially for trunk systems. The ability to exchange various kinds of information with any one regardless of time zone and geographical location is where PCS (personal communication service) is applicable [3]. The transportable/land–mobile satellite system provides a very good means for network access for low population density areas and those countries where terrestrial cellular infrastructures are not well established [5]. Satellite communication networks have an advantage in providing digital links at a required capacity between any possible geographical location without constraints on terrestrial network structures or distance. Satellite communications is still the only effective and economic means for maritime or remote communication systems. In addition to the obvious advantages in providing global personal communications, some unique capabilities for satellite systems are in providing temporary links for unplanned expansions of existing networks. The communication satellite also has an inherent advantage over other transmission media in the ability to readily provide point–to–multipoint communications. For example, in the broadcasting area, especially direct–to–home broadcast with 18–inch dishes, multimedia digital radio provides a good example why satellites are still an important part of future communications networks [6].

Now, these two types of systems, the optical fiber system and the satellite/mobile system, can be complementary. The expansion of the optical fiber system does not mean the end of satellite communication systems. Instead, the use of satellite in radio communications appears to be increasing rapidly in the areas of direct–to–home broadcasting, mobile/PCS and thin–route applications [7]. Research on how to provide mobile satellite services has been very active in recent years [8–11]. It is advantageous to integrate satellite and terrestrial mobile systems if a real global coverage is desired [12]. In Table 1.1 [13], some operational and proposed mobile satellite systems with voice and data support are listed. The orbit types, operations schedule, services, and access methods are given in the table.

Although wide–band, single–carrier TDMA (Time Division Multiple Access) uses satellite capacity efficiently and is cost effective for earth stations with large traffic volumes, it is not so for earth stations with small traffic volumes. This is because TDMA requires a high peak–to–average energy ratio from the earth station transmitters, which reduces their efficiency. As noted in the last paragraph, since large volume, high speed data will be handled more by optical fiber networks than by satellite networks, it is reasonable to predict that satellite networks will be used more for the purpose of linking mobile users or

System	Orbit	Services	Multiple Access	Operations Schedule
MSAT	GEO	Voice, Data, FAX, Paging	FDMA/TDMA	In service
INMARSAT-M	GEO	Voice, Data, FAX	TDMA	In service
GLOBALSTAR	LEO	Voice, Data, FAX, Paging	CDMA	1998
IRIDIUM	LEO	Voice, Data, FAX, Paging	FDMA/TDMA	1998
ODYSSEY	MEO	Voice, Data, FAX, Paging	CDMA	1998

Table 1.1: Characteristics of Mobile Satellite Systems

remote users than for PSTN services. Because of the limitation of radio wave bandwidth, the raw data rate of wireless equipment, in general, will not be extremely high. Therefore, the narrow–band, multicarrier FDMA (Frequency Division Multiple Access) technique can satisfy the demand for digital transmission in earth stations with small traffic volumes because it reduces HPA (High Power Amplifier) power and antenna size so as to enable direct access to a satellite from user terminals. This is why VSATs (very small aperture terminals) use FDMA rather than TDMA in most application [14]. Though the cost of the satellite repeater is amortized over a large number of users, higher efficiency is attained by driving the transponder in the non–linear region and this operation can further reduce users' cost. Therefore, a TDM downlink is preferred. A new satellite system which can take advantages of both multiple access techniques is desired, and the fact that the combination of the two multiple access techniques improves total system performance, not only the power efficiency, is illustrated in [15, 16].

To make it possible to combine these two techniques, on–board signal processing is required. The on–board processor can perform a number of processing tasks such as the decoding of uplink signals for uplink noise cancellation, demodulation to baseband of uplink signals to allow storage and routing, switching of signals between multiple spot beam zones, and digital beam forming [5, 17]. In a conventional satellite system, which works in a bent–pipe mode as shown in Fig. 1.1, received signals are amplified on the satellite and re–transmitted on the satellite downlink. The satellite is just an amplifier in the sky. The fixed terminals and network control center are connected to the PSTN (not shown in the figure) if necessary. In such systems the uplink and downlink modulation formats are the same and the noise on the uplink is also transmitted on the downlink. To maintain the downlink SNR, a high quality amplifier is required on–board the satellite.

Future satellites will have the capability of on–board processing [15]. In a processing satellite, the received uplink signals are demodulated on–board the satellite and then remodulated for downlink transmission. The structure of such a satellite system is shown

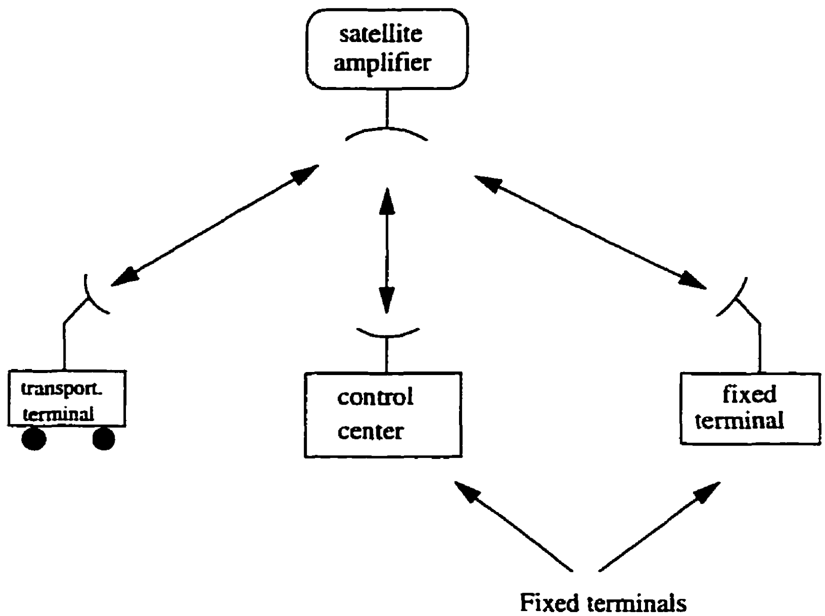

Figure 1.1: Bent–pipe Satellite System

in Fig. 1.2. Though the system configuration looks similar to the system in Fig. 1.1, the satellite is regenerative this time, and therefore, some restrictions may apply to the terminal access to the satellite even when a FDMA uplink is used. The situation depicted in Fig. 1.2 represents small earth terminals accessing the satellite with a FDMA uplink signal format while assuming a regenerative satellite is used in the system. The downlink signal format is TDM. Synchronized uplink signals are desired to reduce payload complexity. This FDMA uplink and TDM downlink configuration is exactly one of the regenerative satellite systems discussed earlier. In such a configuration, the satellite demodulates the uplink signals to baseband and then remodulates these baseband signals into TDM format for downlink transmission. A lot of work has been devoted to this topic [18–20]. Processing satellites can improve the overall system performance because the uplink and the downlink are isolated by the satellite and thus, the uplink and downlink can be optimized separately. In addition, the regenerative system is more flexible than the bent–pipe system. For instance, on board routing of signals can be realized in a regenerative satellite architecture.

An FDMA uplink is desirable because of its simplicity. Each terminal illustrated in

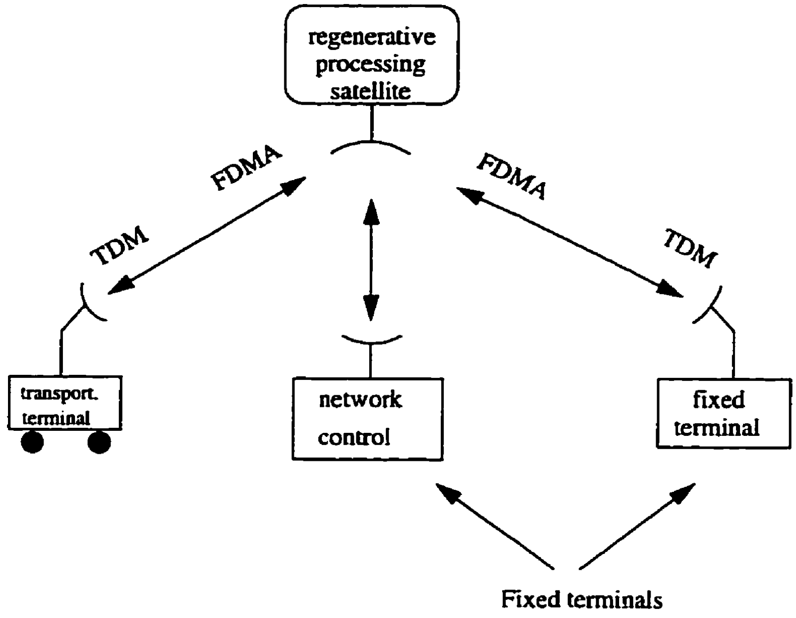

Figure 1.2: Structure of the Processing Satellite System

Fig. 1.2 operates with its unique carrier frequency. Frequencies would be assigned by a control center on a demand basis. The demand assignment will increase the efficiency of using the scarce frequency spectrum when the system is based on frequency division multiplexing. Since each terminal has a unique frequency, the uplink terminal symbol rate can be quite low, thus leading to a low–complexity terminal.

A typical configuration of this kind of processing satellite system is given in [21]. The system has 24 PCM channels in both links with transmission rate of 64 Kbps for each PCM channel. It uses FDMA on the uplink and TDM on the downlink operating at an aggregate data rate of 1.544 Mbps. The ground terminals can be fixed or transportable.

To further increase the system capacity, time–domain multiplexing can be done for each channel in the FDMA frequency assignment. One just assigns a fixed number of time–slots per FDMA carrier signal. When users at the same frequency are time division multiplexed in such a manner, the uplink is said to have a FDMA/TDMA access. The link data rate is kept at, for example 64 Kbps per FDMA channel, however, the per–user, TDMA rate is lower, as will be shown below. New source coding techniques are known to reduce the bit rate required to represent source information with minimum distortion. For instance if an 8 Kbps speech coder is used, for example using adaptive predictive coders [22], 8 such voice channels per FDMA carrier could be time–multiplexed. Similar techniques have been used in the digital cellular system for North America where three users [23], and with more sophisticated CODECs, up to six, are time multiplexed on each cellular system carrier frequency [24]. One should note that if say 8 users at 8 Kbps are time multiplexed onto a single 64 Kbps FDMA channel, each user must transmit data in their time slot at 64 Kbps. The net rate per user is $64/8 = 8$ Kbps as a particular user is assigned one time slot out of eight time slots which constitutes one FDMA carrier frame.

The satellite downlink for the hybrid FDMA/TDMA uplink will still be operated in TDM mode. This link is power limited. The single carrier TDM downlink allows a satellite high power amplifier (TWTA – the travelling wave tube amplifier) to operate at peak power while avoiding intermodulation distortion. The drawback of using TDM in the satellite downlink with low per user data rate is that the earth terminal receivers must be able to operate at a transmission rate of, for a 24 FDMA uplink channels, 1.544 Mbps which is 24 times higher than the uplink transmission rate of 64 Kbps.

This thesis develops and analyzes a global synchronization procedure for the hybrid FDMA/TDMA uplink, TDM downlink processing satellite system [25]. The synchronization will reduce the payload complexity because a simple Fourier transform can be directly performed by SAW devices [26] and this device forms the core of the multicarrier demodulator on–board the satellite. The performance of such a procedure will be investigated by studying the performance of both links in terms of bit error rate. Master–slave synchronization techniques, with the satellite as master and the terminal as slave, will be used to provide a global synchronization system. The time synchronization of a terminal to a processing satellite that uses the SAW devices as a multicarrier demodulator is the fundamental problem considered in this thesis.

1.2 Processing Satellite System

Though the theory presented in this thesis may be applied to not only satellite systems, a processing satellite communication system is used as a test bed. As mentioned in the last section, the uplink rate is 64 Kbps for each channel. If TDMA is used for the uplink, each terminal would be required to send each symbol with a much shorter duration in order to multiplex all users using a single carrier with a multiplexed data rate of 1.544 Mbps while if FDMA is used, only 64 Kbps per FDMA carrier is required which greatly reduces the complexity of the ground terminal and consequently reduces the cost of the system.

The satellite in this system is in geosynchronous orbit. Though media attention has focused on those well–known proposed big LEO and MEO systems such as Iridium, Globalstar, and Odyssey, the only commercially available satellite systems providing mobile services are GEO systems [27]. For example, TMI Communications, a Canadian company, is providing both voice and data services through MSAT launched in 1995. There are also several newly announced GEO systems [27] to compete with terrestrial cellular and PCN. Therefore, the GEO satellite is a very suitable choice for the test system. The techniques presented in the thesis for system synchronization could be applied to an LEO or MEO system. However, some of the system parameters would have to change to cover this situation.

As mentioned in [28], it is unlikely that a single wireless network will provide all services that will evolve. The processing satellite system discussed here is designed to provide thin route services at a relatively low date rate. The system is circuit switch oriented with voice communication as the main service. It is desirable that the ground terminals depend as little as possible on other systems while they are still simple and reliable. The access to the satellite from a ground terminal is FDMA. The downlink from satellite to terminal is TDM.

The system can be divided into ground terminal part and satellite part. To focus the work on the satellite–terminal synchronization issue, well–proven techniques are integrated into the related subsystems as much as possible. As an example, the timing recovery system in the ground terminal uses the algorithm developed by Gardner [29] as a timing error detector.

The center of this processing satellite system is the on–board processor, which demodulate multiple FDMA uplink signals in a block fashion. There are two basic approaches to realize an on–board, multicarrier demodulator. One is the transmultiplexer approach [30] and the other is the chirp transform approach [20]. The traditional channelized, on–board, demodulation of FDMA signals is not considered as an appropriate approach because it will require a large and expensive satellite pay–load for a large number of uplink channels [20].

The transmultiplexer approach to on–board demultiplexing is adapted from the idea of the FDM–TDM transmultiplexer used in terrestrial transmission facilities [31] and is depicted in Fig. 1.3. Digital to analog conversion is needed to convert the digital output from Fig. 1.3 to a waveform. The transmultiplexer for on–board processing uses a polyphase network combined with a FFT to perform frequency to time sequence conversion. The chirp transform approach gets a time sequence from a multi–frequency signal by performing the frequency chirp transform on the signal [32]. A SAW based Chirp Fourier Transform (CFT) processor [33] on–board the satellite is assumed in this thesis. The SAW processor realizes the chirp transform and consequently gives the time sequence we desire for TDM downlink transmission. The advantages of a SAW device are its small size, ruggedness to solar radiation, stable characteristics over a wide temperature range and high reliability [26]. The SAW processor can map a group of frequency signals occupying different bandwidths (*i.e.* a FDM signal) to a time series as illustrated in Fig. 1.4. In Fig. 1.4, the input signal is frequency multiplexed, therefore signals are vertically (as shown in the figure) stacked in the time domain. After processing by chirp Fourier transform, signals with different frequencies are dispersed and compressed in time. A time domain sampling converts the dispersed frequency multiplexed signals to time division multiplexed signals which is perfect for operation of the TDM downlink. The total bandwidth and time occupied by these signals are the same in the uplink and the downlink. QPSK modulation is assumed for the system. The theory of the operations depicted in Fig. 1.4 are quite involved and are given in [34]. Some material on the use of SAW processor theory that is pertinent to this thesis is given in section 3.3.

If the total bandwidth of all k FDMA uplink signals is B, with symbol period T, each uplink channel has bandwidth B/k. Then the converted TDM signal will have a frame length T and each time slot has bandwidth B and time duration T/k. A necessary condition of operation of the simple CFT is that the input signals be synchronized at the satellite processor input on a symbol length basis [35], though there are articles discussing the unsynchronized MCD [36]. This synchronous requirement allows the SAW processor on–board the satellite to provide matched filtering for all input signals at one time [37].

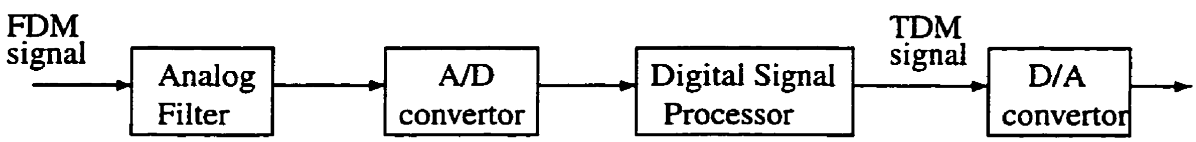

Figure 1.3: Fundamental elements of a Transmultiplexer

1.3 Synchronized Clocks

The system timing and carrier synchronization requirement that will be used in the thesis can be specified by referring to Fig. 1.5, which shows the clock flow of the system illustrated in Fig. 1.2. The earth terminals, either fixed or transportable, send data symbols that are synchronized to the satellite signal processing clock by requirement. Each symbol must be within one signal processing window of the satellite processor in order to allow the processor to properly perform the CFT on all signals. In the test system, the satellite uplink demodulator works at 64 Kbps. The satellite clock is embedded in the downlink

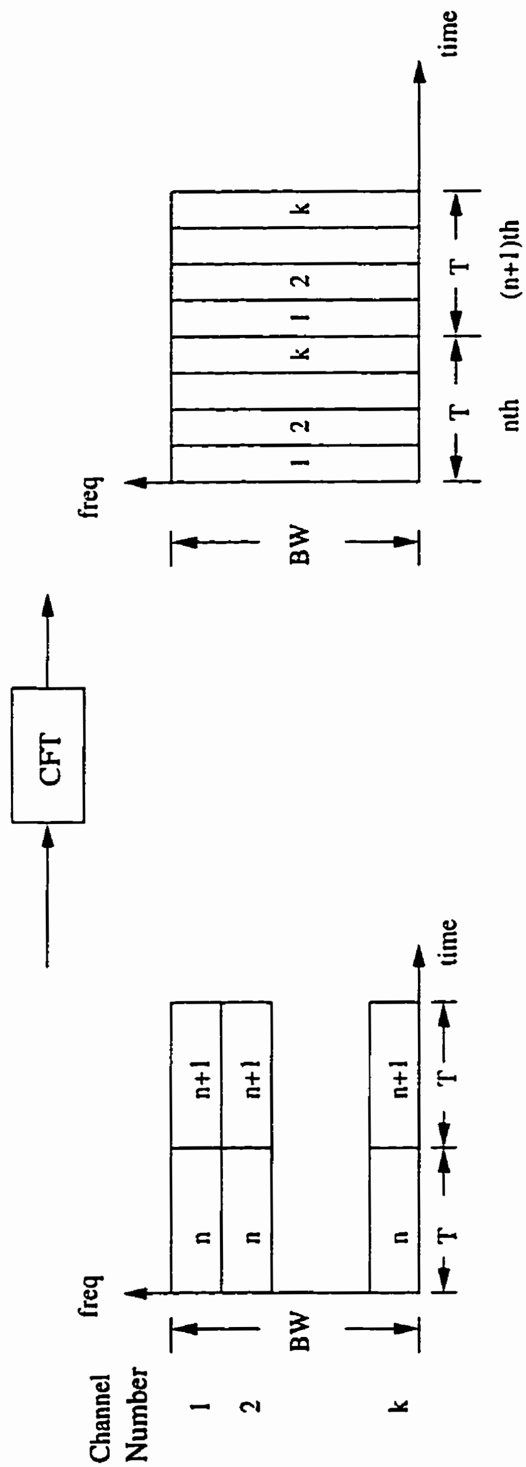

Figure 1.4: CFT processor maps frequency signals to time sequence

transmission system. That is, the terminal clock frequency is derived from the 1.544 Mbps downlink signal from the master satellite clock by the *Clock Freq. Estimate* as shown in Fig. 1.5. It is then reduced in frequency to the one suitable for a transmission data rate of 64 Kbps and altered in phase based on a delay estimation from the *Delay Estimate* block for the transmission path to the satellite. The *ERROR MONITOR per TERMINAL* block in Fig. 1.5 will be the key block studied in this thesis. This block provides the ground terminals with the delay estimation information which will be used to compensate for the uplink propagation delay. Here the delay estimate means to estimate a modulo–T delay throughout the thesis, the propagation delay estimate means modulo–T delay estimate. This process represents a master–slave global synchronization scheme with the satellite as the master and the terminal as the slave. Finally, to demodulate data both on the ground and in the satellite, carrier recovery must take place in both locations if coherent detection is required. The on–board demodulator needs to store carrier phase information for individual channels since all uplink channels are not carrier phase synchronized. A digital phase locked loop will be suitable for this purpose.

The whole system is a master–slave synchronization system with the satellite operating as master and the ground terminals as slaves. The goal of the thesis is to develop and test such a master–slave synchronization system for a processing satellite application. The key issue here is how to synchronize the forward path, that is the uplink, of each terminal in such a system. A large time–delay between satellite and terminal is the major obstacle to be overcome in system design. In summary, this thesis will address the fundamental problem of synchronizing a terminal to the satellite clock without a separate clock signal being broadcast by the satellite.

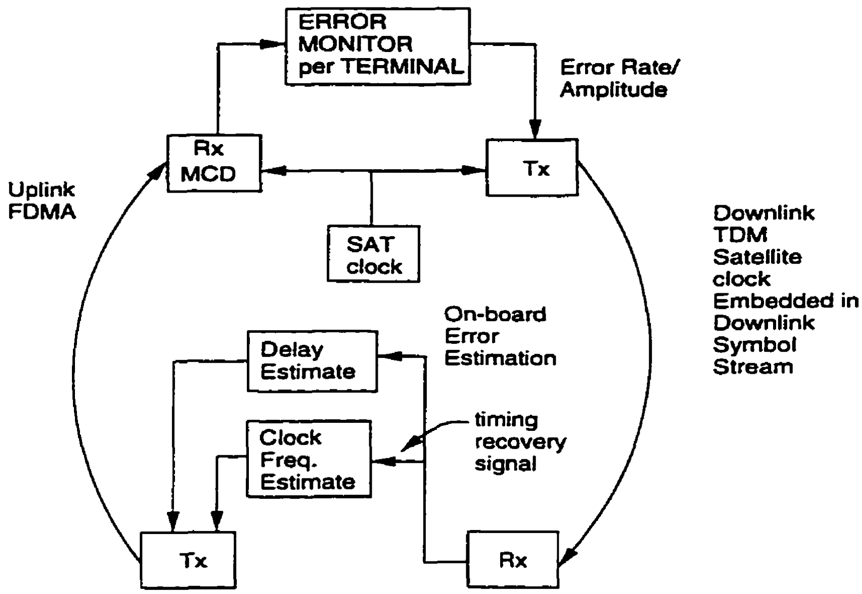

Figure 1.5: Signals of the Processing Satellite System

1.4 Literature Review

Some papers and books related to the topics of synchronization methods, network synchronization – including propagation delay estimation, satellite multiple access techniques, on–board satellite signal processing and digital signal processing using SAW devices are reviewed in this section. These topics are closely related to the study of a regenerative processing digital satellite communication system. The literature review here provides a complete background knowledge for such a system.

It is anticipated in [15] that future communication satellites will have a powerful processing capability. One possible type of on–board processing is when the satellite performs signal regeneration as mentioned by Loo, *et al* in [20]. A regenerative satellite demodulates the uplink signals and re–formats them for downlink transmission. The FDMA uplink, TDM downlink configuration studied in [20] has a satellite uplink which uses a single carrier per channel (SCPC) FDMA to take the advantage of the high efficiency, in the non–linear region, of a high power amplifier.

Most new communication systems take advantage of digital technology which requires information be encoded to digital bits prior to transmission. Digital communication theories can be found in [38]. A digitized network is more versatile than an analog network, where data compression can be used for efficiently utilizing the wireless channel. Sundberg *et al* in [23] described the dual–mode TDMA cellular system for the North American cellular system. This system can expand the capacity of the current analog system by at least three fold. The hybrid FDMA/TDMA system studied in this thesis employs a similar idea to reduce the per user bandwidth to increase the total system capacity while using the same total system bandwidth.

In digital communication networks, synchronization is essential. At the receiver, to coherently demodulate a modulated digital signal, a local reference carrier is required. This reference carrier must have nearly the same frequency and phase as the modulated carrier. The process of producing this reference carrier is called carrier synchronization. Digital receivers also require a clock synchronized to the received bit stream to control the integrate-and-dump detection filters or to control the timing of the output bit stream [39]. This is the clock synchronization problem for the receiver. In [40], the problem of carrier phase estimation and symbol timing estimation for carrier–type synchronous digital signal is examined. A number of carrier and bit synchronization schemes can be found in [40]. Mathematical treatment of general estimation theory including carrier and clock synchronization can be found in [41] and [42]. In [43] a low cost technique of frequency reference distribution within a VSAT network is illustrated. The idea in that paper is to use hub oscillator as a master frequency as we used for the regenerative satellite system. A testing setup in a laboratory environment is given. The paper shows that a very good quality transmit signal at Ku–band can be regenerated from the data clock from a distant hub. Plenty of papers addressing the timing and carrier recovery issues can be found in [44–48]. A paper that compares most non–data–aided symbol timing recovery techniques for digital satellite communications can be found in [11].

To synchronize remotely located clocks, as the case of a regenerative satellite communication system, the propagation delay should be known either through an external method or using the information from the received signals. In [49] a model motivated by the maximum–likelihood (ML) estimation is suggested. In the paper the propagation delay estimation is achieved through a pseudo–noise (PN) code phase modulated onto the carrier. The model is valid for a Gaussian noise environment. It is primarily concerned with satellite communication channels. The mathematical model discussed in [49] is used as a reference in this thesis. A delay locked loop (DLL) can be used to provide the estimation of time delay between two nodes in a communication network, which is shown in [50]. Although, the goal is not to derive a phase detector or a digital receiver using the maximum–likelihood principle, MLE is used for the timing error estimate in this thesis. This timing error estimate is really the estimation of the uplink propagation delay. The papers, [47, 48, 51, 52], show how ML principle can be used to approach a specific problem. More papers can be found in [53, 54]. This thesis follows the guidelines provided by these papers.

A combined receiver sample timing and frequency offset estimation algorithm discussed in [55] is developed for VLSI implementation. The algorithm is suitable for a QPSK or ASK receiver. This paper gives an example of the power of digital signal processing. This technique depends on received symbols and performs best if the received symbols are random.

In addition to the carrier and clock synchronization at each receiver, the network synchronization problem of distributing time and frequency among many remote locations, should be studied as well. In [56], a complete treatment to the network synchronization problem is given. The paper begins by providing a classification of networks. Since the time and frequency waveform transmitted between nodes suffers propagation delay, some form of ranging system is discussed in order to compensate for these delays. A mathematical model of a synchronization network is also presented.

In a satellite communication system, multiple access means the shared use of a satellite transponder. There are only three basic forms of multiple access from the channel–oriented view. They are frequency–division multiple access (FDMA), time–division multiple access (TDMA) and code–division multiple access (CDMA). In FDMA users occupy distinct frequency bands in the same transponder passband. In TDMA the transponder is shared by non-time overlapping signals from many earth stations. In CDMA, signals from many stations occupy the same frequency band at the same time, but are distinguished by their detailed phase structure. Comparison among these multiple access methods is given in [3, 57–59]. The main advantage of FDMA is its simplicity. With digital signals, TDMA and CDMA allow more sharing of hardware of the system. TDMA is better used for high speed systems. CDMA is more robust to interferences. For very high speed digital systems, spectrum spreading may not be practical due to the limit of the hardware bandwidth. Some studies on the multiple access for the third generation cellular mobile radio systems are reported in [60]. The trend indicated in the paper is the use of combinations FDMA, TDMA, and CDMA in various ways.

The system studied in this thesis uses TDM to serve higher satellite downlink data rate. FDMA is used for the uplink. Since in TDMA, the satellite transponder is shared by multiple signals in different time slots, the requirement for synchronization is clear. In [61], several synchronization methods for TDMA are discussed. The synchronization methods discussed in [61] can be classified as frame synchronization methods since TDMA needs a special synchronization for its frames. The strict requirement of synchronization for a TDMA system provides a solid ground for the processing satellite system mentioned in last section because in this system the uplink rate is far more slower than that of a high speed TDMA system. Thus the timing requirement is relatively less demanding.

A generalized frame synchronizer is discussed by Robertson in [62]. The frame synchronizer performs maximisation of a likelihood function then gives several alternative frame starting positions. This method effectively improves the synchronization performance. This paper is introduced here because in the present study, the downlink signal will provide a master clock. An improved synchronization technique will provide a more stable and accurate clock for uplink timing.

A software based TDMA station will enable users to implement very complex frame structures [63]. A TDMA station has been developed for use in a number of advanced communications experiments in [63]. The system has the features of flexibility, adaptability and expandability. This paper will help us in designing our downlink TDM frame in the study.

The FDMA and TDM configuration network is a kind of digital network with FDMA on the uplink and TDM on the downlink. In general, synchronization is required in such a system. Ananasso in [64] indicates that symbol synchronization at the input of an on board processor can greatly simplify the processor structure and reduce its implementation complexity. In this paper, a detailed FDMA/TDM on–board processing payload is given. The impact of possible carrier/clock synchronization strategies on both user terminal and on–board MCD complexity are shown. This paper confirms the value of studying synchronization in the regenerative satellite system. Our master–slave model stems from this paper.

Ananasso *et al* in [65] studied the clock synchronous multicarrier demodulator for multi–frequency TDMA communications satellites in [65]. Though the work is initiated for the large volume high speed system using multi–frequency TDMA, it provides a good look at the on–board processing satellite system. The steady–state clock synchronization and carrier recovery are studied in [65]. A closed–loop master–slave strategy is used for clock synchronization and the carrier phase is recovered through frame–to–frame coherence.

In [16], two promising methods of realizing FDMA/TDM satellite communication system are given. They are transmultiplexer and SAW based CFT. The transmultiplexer method was studied in [20, 30] and [16]. The SAW group demodulator was studied by Traynor in [66]. The mathematical analysis of a SAW based group demodulator can be found in [67, 68]. In these papers, Loo gives the analytical and numerical results of MCM (multiply–convolve–multiply) and CMC (convolve–multiply–convolve) SAW CFT structures. He shows that MCM and CMC are not exact equivalents of each other as previously claimed in other articles. With the idea of on–board processors in mind, the proper synchronization procedure will be considered according to the specific type of processor. In this thesis, the SAW based processor is considered. In the following papers, one can find more on the SAW operation principle, its applications and advantages in space applications.

Jack, *et al* [34] address the theory, design and applications of SAW Fourier transform processors. The application of individual SAW–based processors to spectrum analysis, network analysis, beamforming, and frequency–hopped waveform synthesis is discussed and demonstrated. It is a very good tutorial paper for systems based on SAW devices.

The application of SAW devices in space communications is treated in [69]. The paper aims at presenting the most recent applications of SAW devices to RF signal processing in satellite communication systems. Ananasso [69] first explained the principles of SAW operation. Then he described some possible signal processing applications such as delay lines, bandpass filters, multicarrier demodulators and matched filter receivers in this paper. More SAW applications to on–board signal processing can be found in [70]. In [70], an on–board multicarrier demodulator for a 9.6 Kbps QPSK carrier and a processor for filtering, routing and beam setting for flexible transparent repeaters are described.

The advantages of a SAW device are its small size, ruggedness to solar radiation and stable characteristics over temperature and reliability. These properties are described in [26]. The SAW on–board processor was studied by Shaw *et al* in [33]. This processor is to be used in a FDMA/TDM configured processing satellite system. A necessary condition of operation for this type of processor is that the input signals are synchronized at the satellite input. The symbol timing problem has been studied in [35, 71]. DSP techniques mentioned in [35] can be found in [72].

The symbol timing problem was studied by Simon in [73]. The steady–state phase noise performance of an absolute type of early–late gate bit synchronizer is developed. Gardner studied the bit synchronizer and gave a more efficient algorithm for detection of timing error of BPSK or QPSK data stream in [29]. The algorithm presented in [29] uses mid-pulse to mid-pulse integral to detect timing error and uses a data integral to find data transition directions. The data integral can also be used for data detection. This helps to reduce the complexity since only two samples are needed in the whole algorithm for detecting one symbol. Koblents studies Gardner's timing error detection algorithm applied to various modulation schemes in [74]. He concluded that this algorithm is best when used for bandlimited signals with excess bandwidth factors ranging from 100% to 60%. This thesis considers the recovery of the downlink TDM clock from the downlink TDM signal by using Gardner's zero crossing timing error detector. Koblents' results are used to set the downlink modem signal pulse shape in this thesis. While Gardner presents his algorithm more as an analog approach, [75] shows a joint optimization of the synchronizer with respect to both pattern and Gaussian noise in the context of a full–digital modem. The authors of [75] claim that the optimized prefilter improves the performance in terms of steady–state clock jitter, even with remarkably simple FIR prefilters with a small number of taps.

In [76], Payzin evaluated a bit synchronizer intended for operation with NRZ coded binary signals by using a finite state Markov chain model. Because of the discrete nature of the digital control signals, this model is very useful for the analysis of a digital control signal for the controlled clock or controlled oscillator. The performance of the synchronizer as a data detector is given in this paper. Payzin's method of analysis based on a Markov chain model has been used in this thesis to analyze the performance of our global synchronization system. Performance analysis through digital computer simulation is also performed and agreement with analysis is demonstrated in this paper [76].

Further mathematical tools related to the study of probability can be found in [77,78]. Related papers with computer simulations can be found in [79]. According to the authors, simulation is a useful tool for the design and analysis of communication links. To develop a simulation, there are several steps one should follow. The first step is to develop a model of the system under study. Second, identify the signal processing operation using a mathematical model and then define the simulation products, *i.e.* the set of outputs required from the simulation. Finally, one should select a proper tool to implement the simulation. This tool can either be a software package or a general purpose computer language and depends on the task to be performed. More computer simulation related material can be found in [80, 81]. The simulation results are evaluated using confidence interval with criteria from [82].

1.5 Simulation Approach

The performance of one system should be examined by some means. One possible test is simulation [44]. Computer simulation provides dynamic performance determination which is not readily obtained by analysis. For instance, when the effects of severe band limiting, multipath, and non–linearity must be considered in a communications system, computer simulation can be a very valuable tool [79].

Though subsystems such as the PLL and the timing recovery subsystem can be studied through analysis [83], it is more suitable to use computer simulation to find the interactions and the behaviour of those sub–systems when they are integrated into one complete communication system as suggested in [79]. The purpose of the computer simulation is not only to confirm the theoretical results from the analysis, but also to provide results which are not available from the analysis.

In this thesis, Monte–Carlo simulation is used to obtain all acquisition probabilities and BER performance results. To avoid repeating the same results in the sequel the general accuracy of the Monte–Carlo results is presented in this section. The confidence intervals of these simulation results are given as plus or minus a percentage of the mean of the results with a preset confidence probability. The relationship of the number of simulations required, the confidence intervals and the confidence probabilities can be found in the Appendix of [82]. In this thesis, the simulations of the probability of acquisition usea a confidence probability of 95% for an acquisition probability of 98% with a confidence interval of $\pm 5\%$ of the mean. These conditions represet a requirement of simulation length longer than 3000 and in the simulation, 5000 runs are performed to get the statistics of the probability of acquisition. For the BER simulations, with 95% certainty, all simulated BERs are within 20% to 30% of the mean value. For a BER of 1×10^{-5} with 95% certainty, to get BER simulation results confined to 25% of the mean value, a length of 130×10^5 was used.

The system simulation uses 16 samples per symbol to discretize the timing errors and as such the corrected symbol timing error resolution is $T/16$. For instance, successful acquisition is declared when this timing error is attained. More implementation details can be found in section 6.3 of Chapter 6. Complete individual subsystem test results are given in that section as well.

1.6 Goal of Thesis

In order to present the goal of this thesis the reader is referred to Fig. 1.2. The transportable terminal would access the processing satellite through a FDMA uplink. The goal of the thesis is to develop a closed–loop control system for the terminal to acquire access to the satellite. The satellite processes data from a number of users on every uplink modulation symbol period. The terminal must synchronize its transmission with the symbol integration time interval for the MCD in the processing satellite. This time interval is the duration, T, of one modulation symbol.

A related goal is to have a reliable acquisition system of low complexity. As such, the symbol timing frequency used on–board the satellite is estimated from the downlink signal, which avoids using a satellite beacon signal which wastes precious satellite energy. This downlink is TDM and has N times the symbol rate of the uplink terminal symbol rate for each of N ground terminals which represents the system capacity. A thin route system involving $N = 24$ terminals was studied in i [21]. It is further assumed that all users are in the same antenna beam from the satellite and, as such, a single terminal can receive all N TDM downlink slots. Hence there is much downlink information with which to estimate the symbol clock frequency on–board the satellite. As such, a master–slave procedure is used with the satellite as the master and the terminal as the slave. The second issue is to estimate the uplink propagation delay modulo the symbol period. This is done by sending a probing sequence from the transportable terminal during the acquisition period. Minimal length of the probing sequence is desired in order to minimize the acquisition period for a prescribed probability of acquisition of, for example, 98%. This issue is the main focus of the thesis. The probing signal is a known data signal to the accessing terminal and if it is not aligned with the satellite processing time window, the satellite detection performance will be poor. A measure of this performance is sent on the TDM downlink, in quantized form, to give an error measurement signal for correcting the next attempt at acquisition. This closed–loop system is the main study in the thesis.

An AWGN channel is considered on the up– and down–links of the system. As such, over the acquisition period, the satellite and the terminal are assumed stationary. The acquisition period is usually only about 200 symbols sent as say, 64Kbps, and as such, it takes only 3.125 msec for an acquisition. This time is added to the basic up– and down–link propagation delay of 250 msec to get the overall delay of 253 msec. The satellite and the terminal are assumed stationary over this time period.

Multipath fading or shadowing are not considered because that would be a subject for the mobile terminal case. Furthermore, uplink timing estimation through the data payload portion of the uplink frame via a tracking algorithm is not considered. Only the acquisition portion of the the uplink frame is considered in this thesis with the probability of acquisition as the performance measure.

1.7 Contributions of the Thesis

The main contributions of the thesis are:

1. Development of a timing acquisition procedure for the satellite–terminal that is based completely on master–slave synchronization concepts using measurements on a high rate TDM downlink signal. For instance, tables of expected orbit data are not used. All timing corrections are made in the terminal and the global synchronization does not require a separate beacon signal to get satellite clock information. The newly developed timing recovery algorithm reduces the ground terminal complexity.

2. The frequency of the master satellite timing clock is estimated through timing recovery of the fast downlink TDM signal. This establishes the uplink symbol rate per FDMA channel.

3. The timing phase of the uplink symbol clock is estimated via time–delay estimation on the satellite–terminal signal path. A channel probing technique is presented for this purpose and is the major result in the thesis.

4. For the channel probing scheme, the phase of the uplink FDMA symbol clock is estimated using the Maximum Likelihood Estimation (MLE) criterion and is based on the measured amplitude outputs of the MCD on–board the satellite. The theory of SAW based MCD's is used to derive the timing error correction algorithm to be used in the terminal for the system synchronization technique. The impact of quantization on this estimate is examined as the estimate must be sent to the terminal via the TDM satellite downlink.

5. A complete system simulation for the global synchronization of a terminal to a processing satellite has been designed and tested. The simulation involves system simulation for

   (a) downlink timing recovery,

   (b) downlink carrier recovery,

   (c) uplink modulation, delay estimate, and compensation,

   (d) satellite MCD detection and carrier recovery, and

   (e) downlink modulation and quantization,

and as such a complete closed loop system is represented to evaluate performance of the algorithm studied in this thesis.

1.8 Presentation Outline

The first chapter provides general ideas on using a regenerative satellite to improve system performance, the advantage of using computer simulation to study a complex communication system and a review of the related literature.

The next two chapters provide background information on a regenerative communications satellite. The basic configuration of the system is given in these chapters. The system design philosophy is also explained. Chapter 2 describes the essential parts of a ground terminal. Chapter 3 shows the satellite's communications payload with some detailed material of the on–board processor. A synchronization scheme derived from this processor is going to be studied in this thesis.

In Chapter 4, the problem of an uplink timing estimate is identified and the transmitter timing recovery (T_XTR) is illustrated. Useful mathematical tools are included in this chapter. A complete theoretical treatment of this timing estimate is presented. A timing offset estimation algorithm based on the estimation of uplink sample BER using maximum likelihood estimation (MLE) is analyzed and simulated.

In Chapter 5, an estimation approach to obtain the uplink propagation delay estimate is presented. The performance of the algorithm is examined under different conditions and compared with a BER based method presented in Chapter 4. This method is considered the more promising estimation scheme because of its better performance and is chosen for further tests in the complete communication system simulation.

Chapter 6 presents a complete system simulation. It includes the simulation model design, test and verification. Verification is done by comparing the simulation results of the individual functions with their theoretical counterparts. The computer simulation of a specific system with QPSK on both uplink and downlink with the uplink delay estimation algorithm embedded is performed. The simulated system has 24 FDMA uplink channels with 64 Kbps for each channel and TDM downlink of 1.544 Mbps.

Chapter 7 summarizes results from previous chapters, states the conclusions for the study and gives suggestions for future work.

Appendix A shows the possibility of using the synchronization method presented in the thesis to a hybrid FDMA/TDMA uplink, TDM downlink processing satellite system.

Chapter 2

Ground Terminals

In this chapter, the ground terminal of the proposed processing satellite system is studied as part of the complete satellite system. A brief review on each of its subsystems is given.

2.1 Role of the Ground Terminal

The satellite system synchronization to be studied is based on a master–slave structure shown in Fig. 2.1. In the figure, the satellite clock is designated as the master clock of the system. The ground terminal is the slave in this system. The ground terminal tries to synchronize its clock to the downlink clock by comparing a delayed local copy to the received one. If the system is used purely for the purpose of one way synchronization, as illustrated in [56], where the master clock is distributed to a number of slave nodes, the simple master–slave structure will suffice. When reverse transmission is used as well, as in any two–way communication system, the master must receive a signal from the slave. The synchronization problem emerges if the alignment between the input clock from the slave and the clock waveforms of the master are required, as would be the case in any two–way communication system, with a reasonable delay between transmitter and receiver. This is the case for the regenerative satellite system to be studied. The ground terminals used in

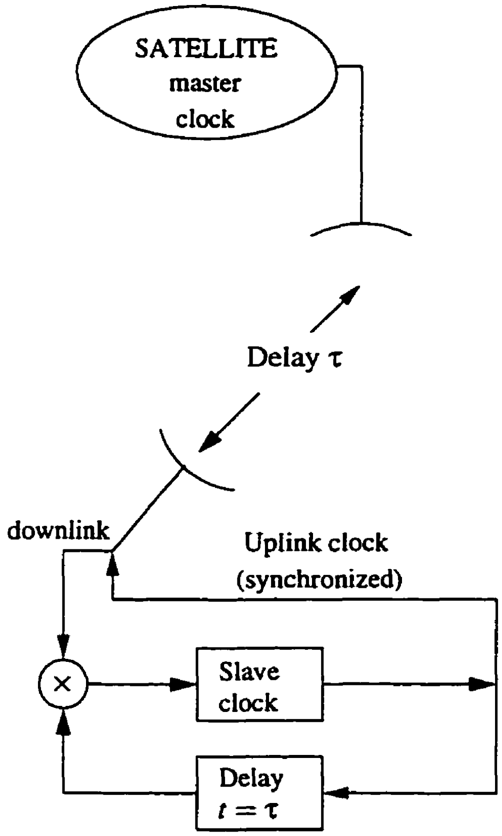

Figure 2.1: Master–slave Synchronization Mechanism

the system are controlled by the satellite, which is designated as a master in the processing satellite system, in terms of carrier and clock recovery. The ground terminals retrieve carrier frequency and clock frequency references from the downlink data bearing signals [43]. Though it is designated as a slave in the whole system, the ground terminal provides necessary adjustment for the clock phase for the satellite uplink in order that the uplink information symbols arrive in the processing period of the multi–carrier demodulator on–board the satellite. This mechanism provides transmitter timing recovery (T_XTR). This capability is provided through the communication between satellite and ground terminals before the system starts a normal full duplex communication process.

It is worthwhile to indicate that the synchronization of the uplink is not achieved through pulling the satellite clock phase to the ground terminal's clock phase. That is, the network is not mutually synchronized. The satellite clock dictates all system clocks as it is regarded as the master in the master–slave system. The uplink clock must be synchronized, in both frequency and phase, to the master clock when the uplink signal leaves ground terminal's transmitter.

The carrier frequency is synchronized by referring the uplink carrier to the recovered downlink carrier. This synchronization guarantees the proper mapping of the FDMA signal to the proper time slot when the on–board processor translates the uplink FDMA signals to the TDM downlink signals. The phase synchronization is performed on–board the satellite using the on–board PLL shown later in Fig. 6.16.

2.2 Terminal Configurations

There are various configurations which have the characteristics of the ground terminal as mentioned in the last section. Depending on the resources a terminal uses, the terminal can be configured to use side information for the purpose of uplink synchronization, or the terminal and satellite are placed in a closed loop as suggested by [64]. It is also possible to use some complicated signal processing techniques [36] to get rid of the restrictions on the data rates and the synchronization requirement. Since the unsynchronized payload is not the main interest of this project, this approach will not be discussed any further.

The interest of this study is in finding a simple and efficient master/slave synchronization scheme which requires the minimum resources from side information to provide system path information for the purpose of synchronization. The scheme used in this thesis is based on an master–slave architecture with some synchronization information exchanges.

One of the basic functions of the ground terminal is to retrieve information from the satellite downlink. This task is implemented by a digital receiver with carrier phase and symbol timing recovery, as depicted in Fig. 2.2. The downlink receiver uses a discrete decision–directed phase locked loop (DD-DPLL) for the purpose of carrier recovery. A discrete phase sampling clock controlled by the timing recovery loop constitutes of a timing error detector described by Gardner in [29] and some related functions. The timing error detector takes two samples from the receiver's matched filter output for each symbol and one of the two samples can also be used for signal detection. This type of timing error detector has been studied experimentally by Koblents in [74] for mobile satellite, voice–rate modems. The discrete type PLL has been investigated by Hung in [30]. This part of the terminal is illustrated in Fig. 2.2. The block called phase rotator is equivalent to a carrier frequency down-convert or with non–coherent phase between two signals. The carrier recovery is placed after timing recovery because Gardner's timing error detector is immune from the presence of carrier phase and slowly varying frequency offset.

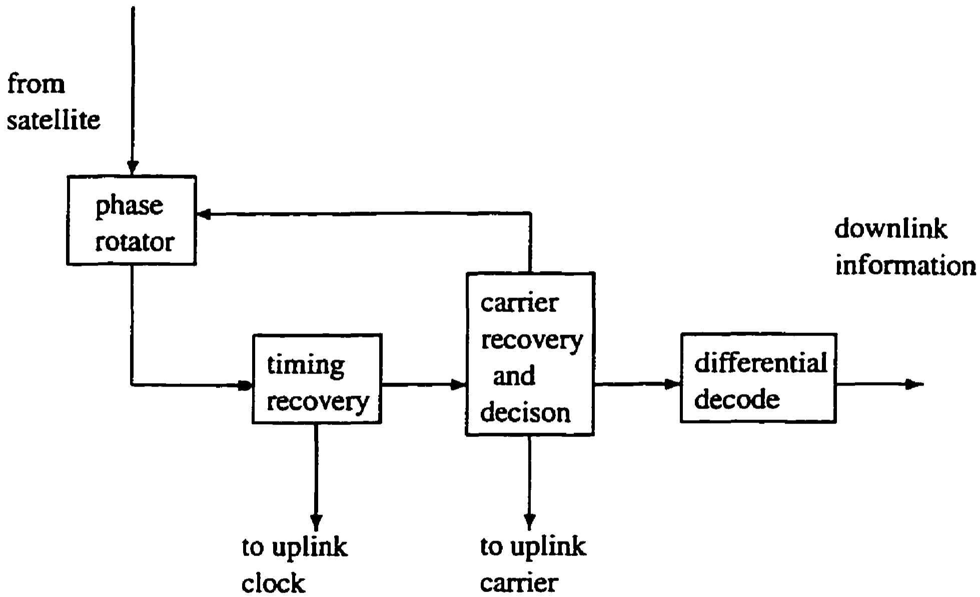

Figure 2.2: Downlink Receiver

The carrier recovery circuit requires a signal decision as well since the phase detector is decision directed. The recovered carrier phase is applied to the incoming signal to reduce the phase fluctuation going into the timing recovery circuit. This arrangement improves the timing recovery performance. The carrier recovery circuit performs phase tracking per symbol period. The recovered timing clock controls the sampling instant of the carrier recovery circuit.

Since the carrier frequency and the clock are recovered by the downlink receiver for the coherent demodulation of the downlink signal, it is possible to use them as reference signals for the uplink transmitter. This is similar to a master–slave synchronization scheme. The advantage of such a configuration is that no satellite processing is required to obtain a reference signal. The reference signal comes from the downlink. The downlink signal is available to all the ground terminals in the satellite antenna coverage area. If all the terminals are synchronized to the downlink, then one stable source used on–board the satellite provides a good reference to all the terminals.

The ground terminal uses the recovered carrier as the reference for the uplink carrier. This relationship between the downlink and uplink signals assures the carrier frequency accuracy in the uplink signal. The clock phase will be controlled in such a way that the signal arrives in the satellite demodulator with its symbol boundary aligned with the satellite demodulator clock. The adjustment of uplink clock phase requires the information of propagation delay between the satellite and the ground terminal. The method of obtaining the delay information will be discussed in detail in later chapters. Here just assume the information is available to the ground terminal. This part of the ground terminal is illustrated in Fig. 2.3. The uplink modulator uses normal QPSK modulation with a rectangular pulse shape. The transmitting clock phase is controlled by the propagation delay information. All the uplink signals are nearly time–aligned at the input of the satellite demodulator when synchronization has been achieved.

2.3 Ground Terminals in the Satellite System

The combination of the sub–systems of the ground terminal discussed above, plus the uplink transmitter, results in a block diagram of the complete ground terminal given in

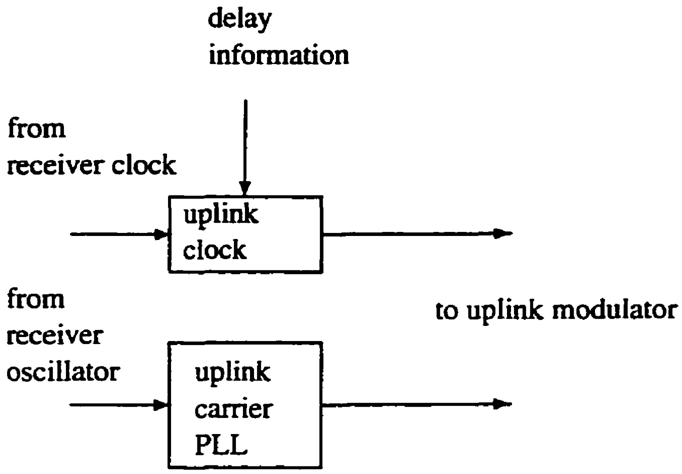

Figure 2.3: The Control part of a Ground Terminal

Fig. 2.4. In the diagram, three separate sub–systems are interconnected and the synchronization control signals are fed from receiver to the uplink transmitter.

This terminal functions as follows. When the terminal is in the standby mode, it monitors the satellite downlink. When active, the downlink carrier and clock are recovered and are available to the uplink transmitter of the ground terminal. When the terminal initiates a call, the recovered carrier and clock are used as references for the uplink path to the satellite. The transmitter clock phase is adjusted according to the estimate of the uplink propagation delay that is estimated on–board satellite and transmitted to the ground terminal via TDM downlink. The purpose of this adjustment is to compensate for the propagation delay between the transmitter and the receiver. The delay compensation adjustment of the transmitter clock phase is within one symbol period T. One approach to implement this compensation is to let the satellite on–board processor examine an uplink probe signal and get a delay estimate from this signal. The delay compensation error is then transmitted to the terminal via the satellite TDM downlink. The ground terminal picks up this information, then transmits another probing signal with the transmitter clock phase adjusted according to the information from the satellite to confirm the synchronization. If the correction is in the wrong direction as would be indicated by a larger timing error mea-

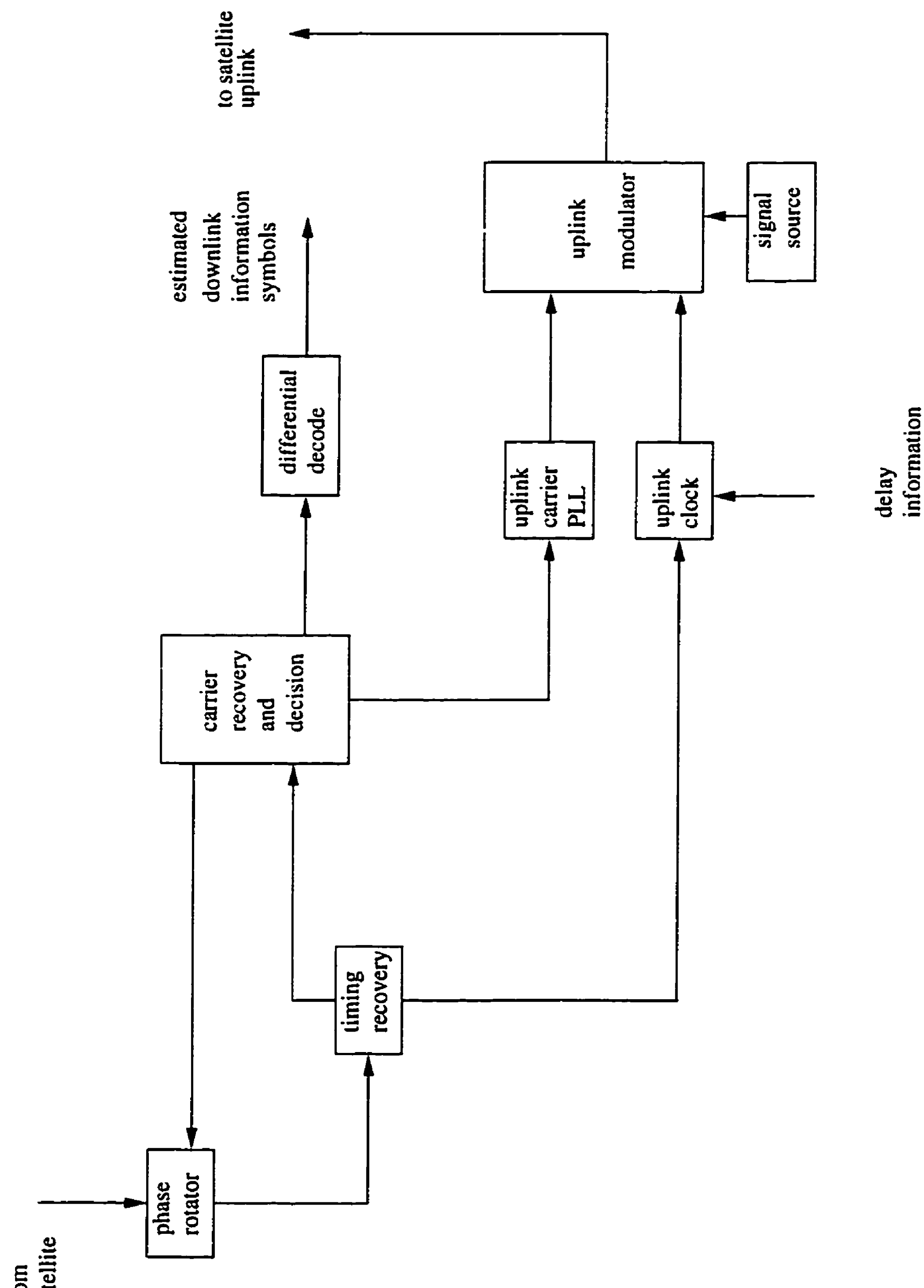

Figure 2.4: Block diagram of a Ground Terminal

surement, the process should be repeated one more time in the opposite direction to confirm that timing is properly aligned.

In this chapter, the ground terminal configuration and operation were introduced. The satellite portion of the system will be introduced next chapter.

Chapter 3

The Satellite

In this chapter, the satellite portion of the system is introduced to give readers a complete picture of the overall system under investigation.

3.1 Processing Satellite

Use of a processing satellite improves system performance [64] and use of on–board processing allows for independent optimization of uplink and downlink parameters [36]. The processing satellite under investigation in this project is for the low to medium volume of traffic with a relatively low data rate compared to a gigabits per second transport systems. A typical application would involve 24 uplink channels with FDMA access and each transmitted PCM signal at 64 kbps, and a T1 (1.544 Mbps) downlink operated in a TDM mode. These parameters are typical "thin route" system parameters in satellite communications.

This processing satellite takes FDMA signals on the uplink, converts them to a single high speed data stream, then transmits the data on a TDM downlink. Traditional analog filter banks cannot be used for the on–board demultiplexing due to mass and volume constraints. Alternative solutions based on Fourier transform techniques have been developed for on–board demultiplexing/demodulation [16]. In such a FDMA uplink and TDM downlink configuration, the ground terminals can transmit signals at high power without the problem of intermodulation even when operating its high power amplifier in saturation because it is a single carrier system. On the satellite side, since the signal is transmitted by TDM and each channel takes a time slot, the amplifier is in a single carrier mode and can operate in the non–linear region. Therefore, such a system has high efficiency in the usage of power amplifiers.

3.2 Satellite Configuration

The communication payload from a modulation perspective of the satellite consists of the down–converter, the on–board multicarrier demodulator, the downlink modulator, and up–converter. A block diagram showing the interconnection of these sub–systems is given in Fig. 3.1.

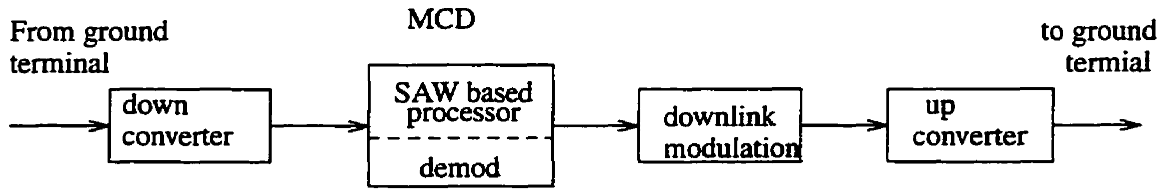

Figure 3.1: Satellite Communication Payload

The down–converter converts carrier frequency of the uplink signal to the intermediate frequency (IF) where the SAW based on–board processor is operating at. The selection of the IF depends on the material used for the SAW device substrates and varies in a wide range from 50 MHz to 400 MHz [5]. The SAW based processor that motived this study has a center frequency of 70 MHz [37]. The frequency relative to the center of the SAW processor bandwidth is reserved for this process. That is the down–converter simply shifts the signal spectrum to the SAW's operating frequency band.

The signal from the down–converter is fed to the on–board processor for demultiplexing and demodulation. The SAW based MCD performs the Fourier transform on the input signal resulting in the spectrum of the signal mapped to the output of the processor as a function of time. That is, the spectrum in the frequency domain is represented by a time domain waveform. Because the spectrum of the input signals reveals the relative positions of different carrier frequencies of the uplink signals, the MCD output provides these input FDMA carriers as a time domain multiplexed signal. Thus, this device is ideal for a FDMA to TDM transformation which is required in the processing satellite system since the downlink is operated in TDM mode. Given a constant phase input at a given frequency, the output signal phase is constant at a specific time and this time is given as

$$t_0 = \frac{\omega}{\mu} \tag{3.1}$$

where ω is the frequency relative to the center frequency of the SAW processor and μ is the chirp rate of the on–board SAW filter. The value, t_0, is the sampling time when the output signal has a constant phase if the modulation is removed. This sampling instant corresponds to the peak output magnitude of this device when the uplink timing and frequency are properly synchronized. This constant phase, considered as an offset, can be tracked by a phase locked loop following the SAW processor and thus can be removed for coherent demodulation. The topic of phase tracking will be discussed in more detail in the later chapters. However, some results on this topic can be found in [37]. A block diagram of the multicarrier demodulator is given in Fig. 3.2. The demodulation is performed by a decision directed digital PLL as shown later in Fig. 6.16 and it is taken from [37] with some minor modifications. The output of the MCD is either sent to the delay estimation block in the set–up and tracking mode, or is sent to the DD–DPLL in the data mode as illustrated in Fig. 3.2. The estimated information is transmitted through the TDM downlink to the corresponding ground terminal as the demultiplexed/demodulated signals are sent to all ground terminals through the downlink circuit. If error correction coding is used in the uplink, then the error correction process can be performed on the bit stream. The delay estimation process and

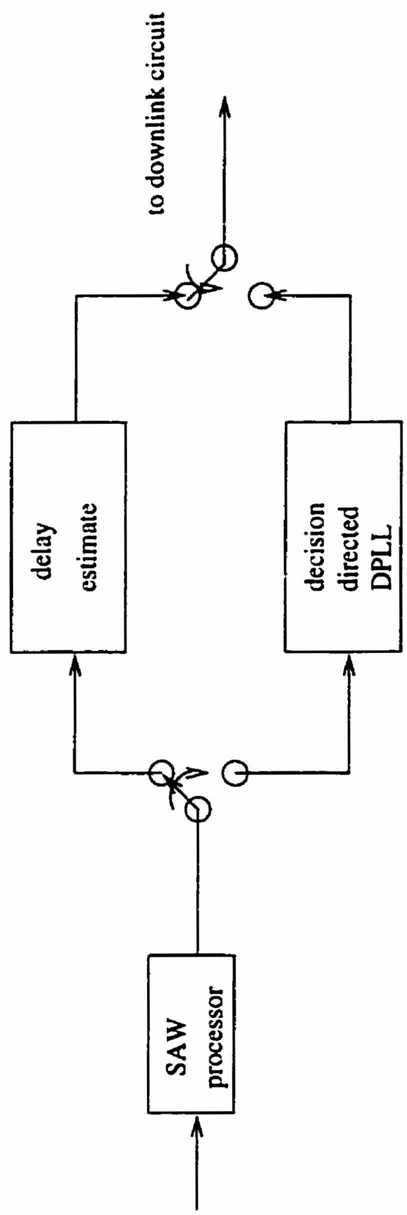

Figure 3.2: Block Diagram of Multicarrier Demodulator

the demodulation process using a DPLL are switched according to a pre–defined schedule. When the delay estimate is obtained from the demodulated signal, instead of using the output of the MCD directly, as will be discussed later in the next chapter using the BER as the timing error indicator, the delay estimate block should be placed after the DPLL block.

The SAW processor is the key part of the processing satellite system under investigation. In Fig. 3.2, the block named *delay estimate* is the core of this thesis. The theory used in this block and the simulation implementations are explained in the next section. Right now, readers only need to know that the propagation delay of the satellite uplink is going to be determined by the system itself.

The downlink modulation uses QPSK with the baseband signal pulse filtered to square–root raised cosine pulse shape. The receivers of ground terminals have the same filters matched to this pulse shape.

3.3 SAW Processor

Since the system is based on an on–board processor using SAW devices to perform a chirp Fourier transform (CFT), it is necessary to take a close look on how the SAW processor works.

3.3.1 CFT Principles

The SAW chirp Fourier transform (CFT) is a Fourier transform valid for a certain bandwidth and over a finite time interval [70]. This subsection gives the general form of CFT. More properties of CFT are discussed in the next subsections. The CFT can be derived from the usual Fourier integral as follows. The usual Fourier integral is

$$F(\omega) = \int_{-\infty}^{\infty} f(\tau)\exp(-j\omega\tau)d\tau. \tag{3.2}$$

For the CFT, the relationship between frequency and time is a linear chirp as

$$\omega = \mu t \tag{3.3}$$

where μ is the chirp rate having the dimension of rad/s^2. The derivation of the CFT starts by substituting for ω with μt in (3.2) and noting that

$$-2t\tau = (t-\tau)^2 - t^2 - \tau^2.$$

Then equation (3.2) becomes

$$F(\mu t) = \int_{-\infty}^{\infty} f(\tau) \exp(j\frac{\mu}{2}((t-\tau)^2 - t^2 - \tau^2))d\tau. \tag{3.4}$$

By re–arranging the terms in the exponential, the integral in (3.4), becomes

$$F(\mu t) = \exp(-j\frac{\mu t^2}{2}) \int_{-\infty}^{\infty} [f(\tau)\exp(-j\frac{\mu\tau^2}{2})] \exp(j\frac{\mu(t-\tau)^2}{2})d\tau. \tag{3.5}$$

In (3.5), the $[f(\tau)\exp(-j\frac{\mu\tau^2}{2})]$ term is recognized as an multiplication of $f(\tau)$ and $\exp(-j\frac{\mu\tau^2}{2})$. Then, from the definition of convolution integral [38], the function in the square brackets is convolved with $\exp(j\frac{\mu\tau^2}{2})$. Finally, the convolution integral times another function $\exp(-j\frac{\mu t^2}{2})$, gives the right–hand–side of (3.5). Therefore, equation (3.5) shows that a chirp Fourier transform (CFT) is implemented with two multipliers and one convolver. Since the convolution is performed between two multipliers, this scheme is called the multiply–convolve–multiply (MCM) configuration. This derivation is similar to the one given in [34] and a block diagram for the MCM is shown in Fig. 3.3.

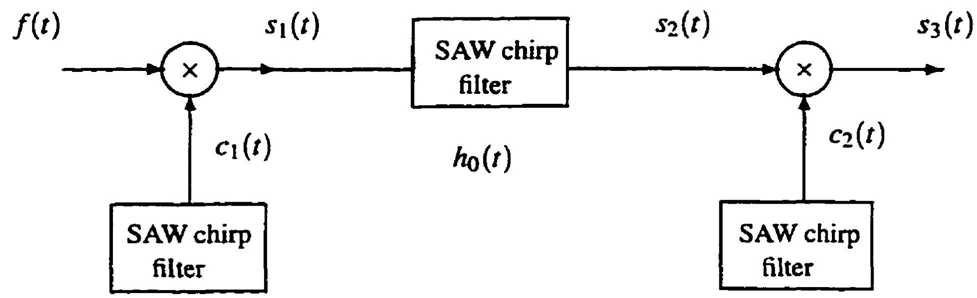

Figure 3.3: Illustration of MCM CFT configuration

In the figure above, $c_1(t)$ and $c_2(t)$ are the multiplying chirp waveforms and $h_0(t)$ is the impulse response of a chirp filter. All three functions have the waveform representation

$$h_0(t) = w(t)\cos(\omega_0 t \pm \frac{\mu}{2}t^2 + \theta)$$

where $w(t)$ is a *weighting* function which is set to one in this study, ω_0 is the center frequency of the SAW device and the $\pm$ sign indicates that it is either an *up–chirp* or a *down–*

chirp. An up–chirp means that the frequency increases as time increases. θ is a phase constant and it can be set to an arbitrary value. In case of coherent detection of a PSK signal, θ represents the modulation information when it appears in the input signal. $s_i(t)$ are the signals at the corresponding output points in Fig. 3.3.

3.3.2 Comments on Chirp Lengths

In [34], it is said that a longer chirp length in a MCM configuration is required to properly perform the Fourier transform. Such a configuration is best for the purpose of taking a Fourier transform. The points can be explained as follows.

The output of the chirp filter ($s_2(t)$ in Fig. 3.3) contains the Fourier transform of the input signal. Because of the relationship of frequency and time through the linear chirp, the frequency spectrum can be spanned on the time axis. To display the spectrum without amplitude distortion, a flat response is required over this frequency range. This flat response is obtained only if the filter chirp length is longer than the input signal length. A conceptual diagram shows this comment is given in Fig. 3.4. If one thinks of this process in terms of a convolution, since both signals are time gated, the convolution of these two signals leads to the outputs shown in Fig.3.4. In "output (1)", the filter length is $T_d = T$.

From this figure, it is clear that a filter length of $T_d = 2T$ is the best for the purpose of processing a chirp signal with length T. This is because the input signal needs T seconds to be totally moved into the filter (for the period $[0, T]$ shown in "output (2)" of Fig. 3.4). This period does not provide a correct transform spectrum amplitude. In the next T seconds, we can sample the spectrum at the output of the filter. Then there is a tail that lasts for T seconds for the signal to be moved out of the filter. A longer filter length provides the same spectrum but since extra taps which are not used to provide useful signals are given here, only the noise is increased. Consequently the signal–to–noise ratio is reduced.

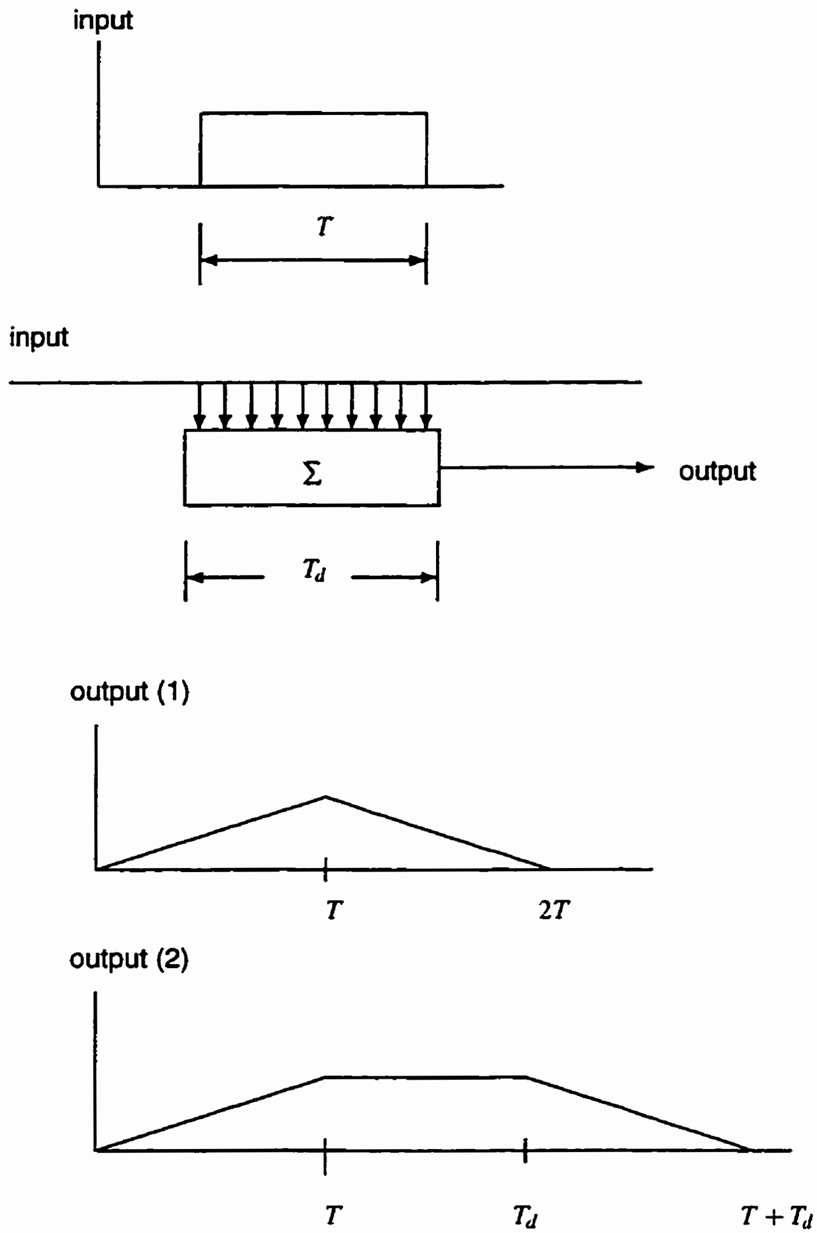

Figure 3.4: Filter Chirp Length Requirement

3.3.3 Pulse Compression and Processing Capacity

The signal pulse duration is compressed after passing through a chirp filter. Let the 3 dB pulse width of the output pulse be $\tau_p(3\ \mathrm{dB})$, then the pulse width is given as

$$\tau_p(3\ \mathrm{dB}) = \frac{0.89}{B} \tag{3.6}$$

where B is the bandwidth of the input chirp signal in Hertz, $B = \mu T/2\pi$. Then the input pulse is compressed by a ratio of $k = T/\tau_p = BT/0.89$. To reduce the inter–symbol interference, a more rigorous pulse width is defined. It is a 4 dB pulse width.

$$\tau_p(4\ \mathrm{dB}) = \frac{2\pi}{\mu T} = \frac{1}{B} \tag{3.7}$$

and this leads to the pulse compression ratio of $k = BT$. The term BT is called time bandwidth product. This pulse compression ratio determines the number of frequency channels the multicarrier demodulator can process. It is clear that with a pulse with definition of (3.7), the processor can process less signals than for the case represented by (3.6). To reduce the effects of sidelobes, a windowing function is usually used. The windowing will further increase the pulse width and consequently reduce the number of channels that can be processed.

3.3.4 CMC Configuration

The CMC arrangement can provide a Fourier transform as well as shown in [34,67]. The distinct advantage of the CMC arrangement over the previously discussed MCM configuration is that C–M–C has a larger time bandwidth product. In other words, given the same time bandwidth product, CMC offers higher processor frequency resolution and bandwidth.

Loo in [67] shows that a CMC configuration with finite chirp length can perform a CFT on the input signal with a desired output. For a wideband system, the CMC configuration will be the ultimate choice. More relevant discussions on how the processor operates can be found in [37,68].

3.3.5 Simulation Results

A brief simulation has been performed using Matlab to illustrated the MCM CFT. In the simulation, all operations are assumed to be ideal.

Parameters used in the simulation are:

$$\begin{aligned} \mu &= 100\, rad/s^2 \\ \omega_0 &= 80\, rad/s \\ \text{frequency range} &= [30, 130] \\ \text{signal duration} &= 1\, sec \\ \text{chirp duration} &= 2\, sec \end{aligned}$$

The impulse response of this CFT processor gives desired gate function ranging from $[-50, 50]$ in radian frequency, centered at ω_0 as expected. Then a chirp signal gated to one second with carrier frequency of ω_0 given as

$$x(t) = \exp j(\omega_0 t - \frac{\mu t^2}{2})$$

is fed to the processor. The output is centered at ω_0. It is a sinc function since the input is a rectangular pulse times the linear chirp signal. The plot is shown in Fig. 3.5. To read this figure and subsequent figures, the x–axis is the relative frequency, therefore, the zero frequencies in the plots correspond to ω_0. A reading of -50(rad) from the plots corresponds to a real frequency of 30(rad), etc.

A single frequency signal with a frequency other than ω_0 (which is $30\, rad/s$) is also processed by the CFT. The result is shown in Fig. 3.6. It can be seen from the plot that the peak of the plot is located at the corresponding frequency. Then, a multi–frequency signal is processed by the CFT to simulate the processing of FDMA signal. The plot is given in Fig. 3.7. All frequencies are revealed by the peaks in the plot.

Finally, the chirp rate μ is changed from $100\, rad/s^2$ to $200\, rad/s^2$ to show the effect of chirp rate on the bandwidth of a CFT processor. It is clear from Fig. 3.8 that a CFT processor with larger μ has larger pulse width compression on the input signal. Therefore, it

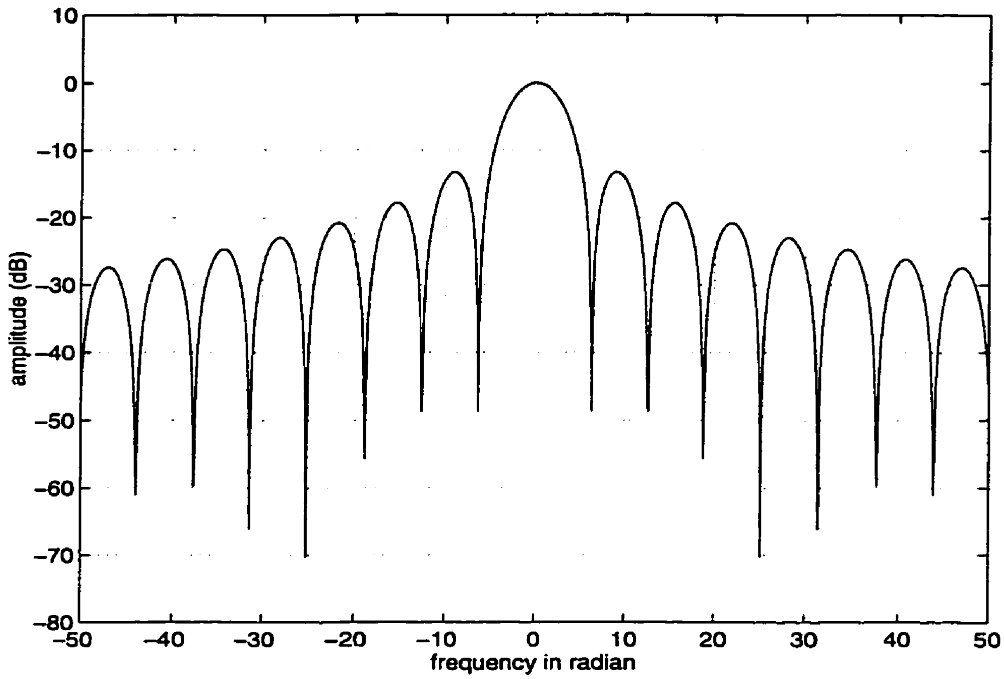

Figure 3.5: Single Frequency Input Signal

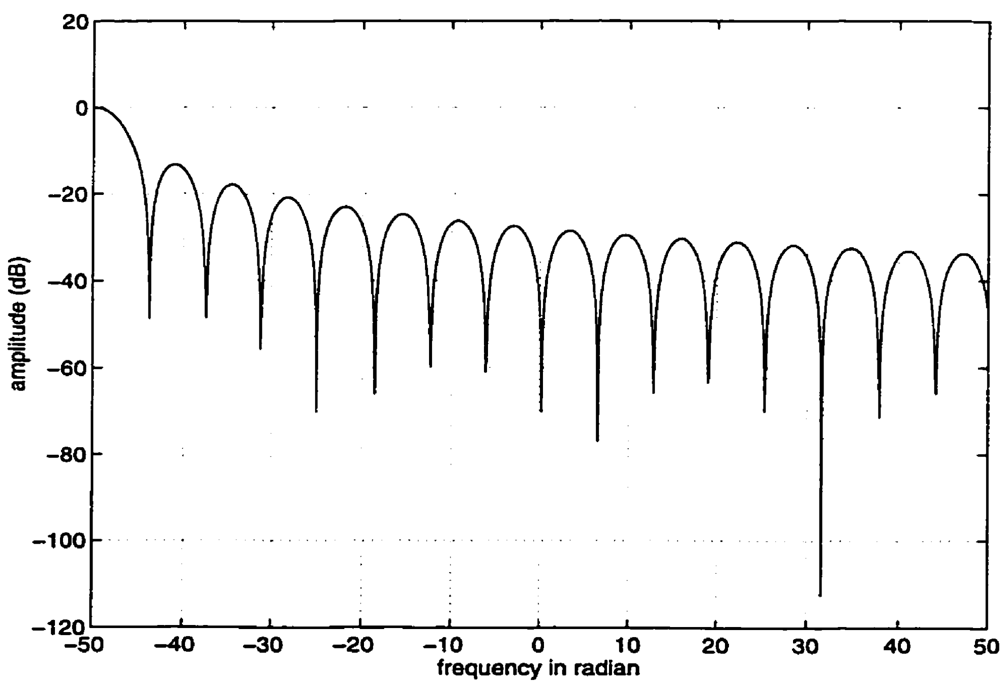

Figure 3.6: Single Frequency Input Signal ($\omega \neq \omega_0$)

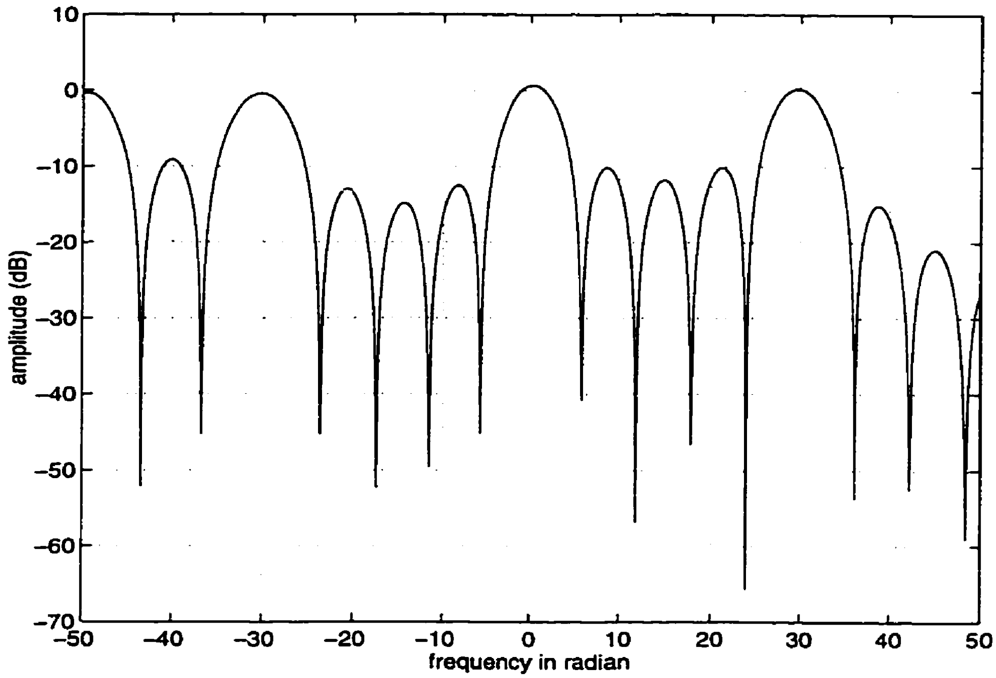

Figure 3.7: Multi–frequency Input Signal

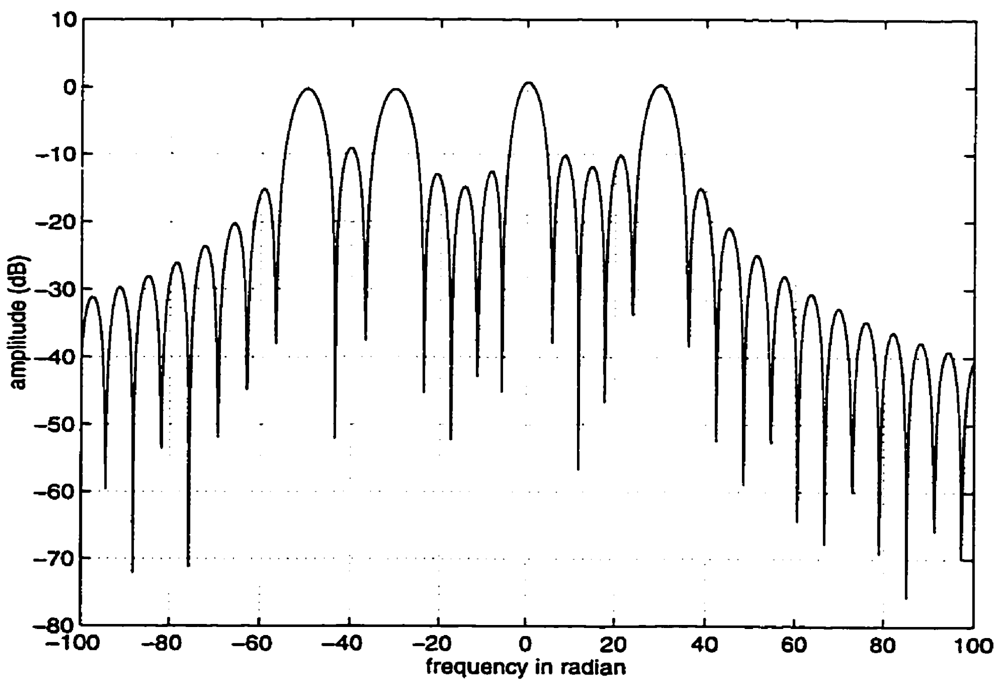

Figure 3.8: Multi–frequency Input Signal with Larger μ

can process a wider input signal bandwidth, which means that more frequency multiplexed channels can be processed simultaneously.

The output of the MCM configured on–board MCD is further studied and the relationship of timing offset and the processor output is established in section 4.3.1. The same processor is used in the system simulation in Chapter 6. To demodulate multiple uplink signals, time alignment among uplink signals is required in order to be able to sample the output of the processor directly [26]. The timing error measurement of uplink signals for a MCD using a SAW device is the central theme of this thesis and it will be treated in much detail in the following chapters.

The system which motivated the study of the synchronization algorithm based on measuring uplink signals from the output of the MCD was presented in the previous chapter and this chapter. In the next chapter, the synchronization algorithm will be studied in detail through theoretical derivation and computer simulations.

Chapter 4

Delay Estimate (1)

This chapter studies the uplink synchronization of a ground terminal and the satellite on–board processor. The synchronization is achieved by compensating for the uplink propagation delay in the ground terminal's transmitter. One method of delay estimation is demonstrated theoretically. Simulations are performed to confirm the theoretical analysis in this chapter.

4.1 Conceptual Approach

In normal communication systems the clock and carrier are recovered at the receiver. Fig. 4.1 depicts a typical synchronized system where the system synchronization is implemented by digital circuits. The dashed box at the receiver indicates that a data decision is used to help generate the error measurement signal. If a decision–directed structure is not used, the decision block is moved out of the synchronization loop. Synchronization is obtained by the adjustment of the local oscillator's phase which is controlled by the error signal generated by comparing the input signal and a local reference signal.

The situation is different for the processing satellite system studied in this thesis. The traditional receiver side tracking synchronization schemes would fail in such a system since multiple uplink signals have different phases and therefore, one on–board clock cannot track all the uplink clocks at one time. Hence, if the receiver cannot perform symbol synchronization, the transmitter must do it. The approach is illustrated in Fig. 4.2. In the figure, the transmitter clock phase is adjusted in such a way that it arrives at the receiver aligned with the receiver clock phase. The dashed line which connects the receiver and the error signal generator means that it is possible to use the information from the receiver to control the clock of transmitter.

Since the clock phase is directly related to the propagation delay, if the delay, which is obtainable from ranging systems, is known, the clock phase can be adjusted precisely. It is also possible to find the delay information by the satellite receiver through processing of the received signal. The idea of obtaining the propagation delay on the uplink directly is considered in this chapter through finding a timing error indicator from the input uplink signal to the on–board processor. Then, either the delay is computed on–board the satellite and the ground terminal is informed or the information of the uplink is transmitted to the ground directly, perhaps, for the further estimation. If such a timing error indicator is observed at the ground terminal instead of on–board the satellite, the downlink transmission link must be considered in determining the uplink delay estimation.

One obvious timing error indicator is the bit error rate (BER) at the receiver in the

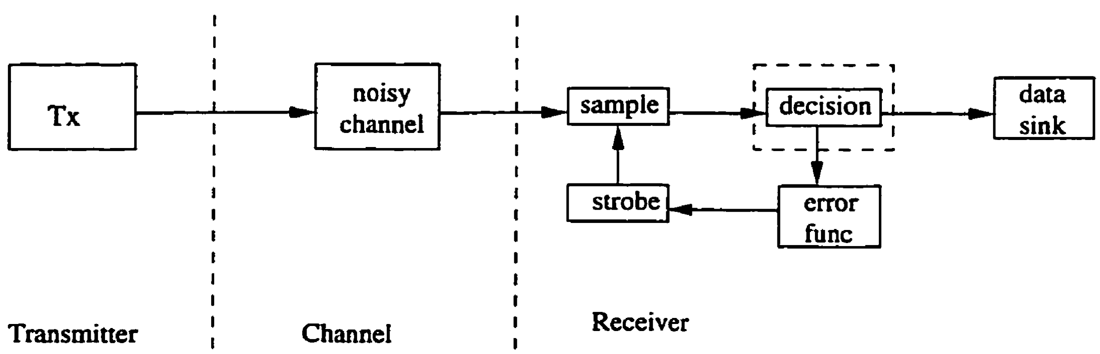

Figure 4.1: Synchronization Subsystem

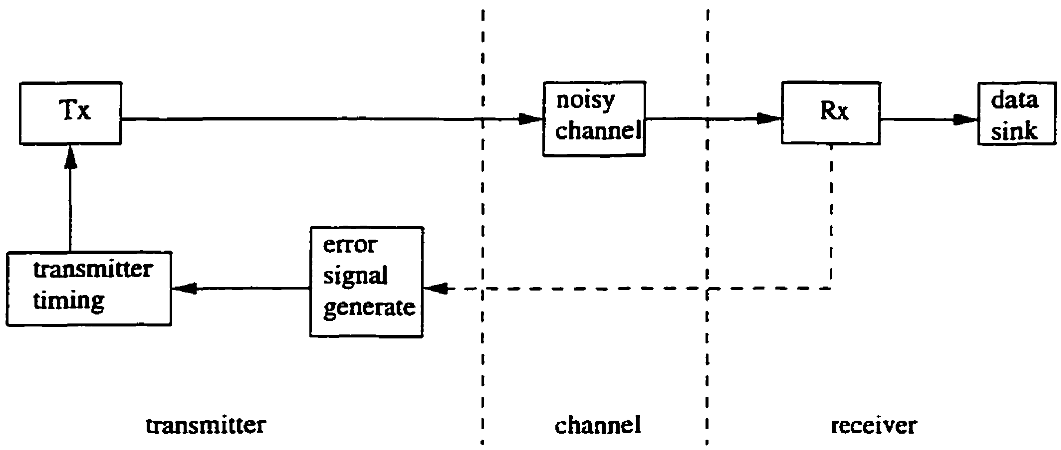

Figure 4.2: Transmitter Timing Recovery

satellite. For any timing error larger than zero, the BER is larger than that for the correct timing case. Before proceeding to derive the delay estimation method based on this BER indicator, some tools to be used in the analysis are introduced in the next section.

4.2 Mathematical Tools

Some frequently used random variables in this thesis are described in this section. For a more complete discussion of random variables, please refer to [77] and [78]. The theory for the maximum likelihood estimation (MLE) method is presented here as well.

4.2.1 Discrete Random Variables

Suppose that an experiment, or a trial, whose outcome can be either a *true* or a *false*, is performed. Let $X = 1$ represents a *true* outcome and $X = 0$ a *false* outcome. Then the probability mass function of X is given by

$$\begin{aligned} p(0) &= P\{X=0\} &= 1-p \\ p(1) &= P(X=1) &= p \end{aligned} \tag{4.1}$$

where p, $0 \leq p \leq 1$, is the probability that the experimental result is a *true*.

This random experiment is called Bernoulli trail. A random variable X is said to be a Bernoulli random variable if its probability mass function is given by equations in (4.1) for some $p \in (0, 1)$ [78].

Now, if the trial is performed independently N times, each of which results in a *true* with probability p and *false* with probability $1-p$, the random variable X represents the number of successes in N trials and is said to be a *binomial random variable* with parameters (N, p) [77,78]. Thus, the Bernoulli random variable is a special case of binomial random variablewith parameters $(1, p)$.

The probability mass function of a binomial random variablehaving parameters (N, p) is given by

$$p(k) = \binom{N}{k} p^k (1-p)^{N-k} \qquad k = 0, 1, 2, \cdots, N. \tag{4.2}$$

The summation of Eqn. (4.2) is the expansion terms of binomial

$$(p + (1-p))^N = 1 \qquad \text{as} \quad k = 0, 1, 2, \cdots, N.$$

For $k = 0$, $p(0) = (1-p)^N$ and a recursive approach to calculate all the discrete probabilities in (4.2) is derived as follows:

$$\begin{aligned} \frac{p(k)}{p(k-1)} &= \frac{P(X=k)}{P(X=k-1)} = \\ &= \frac{\frac{N!}{(N-k)!k!} p^k (1-p)^{(N-k)}}{\frac{N!}{(N-k+1)!(k-1)!} p^{k-1} (1-p)^{(N-k+1)}} \\ &= \frac{(n-k+1)p}{k(1-p)} \end{aligned}$$

for $k = 1, 2, \cdots, N$. Therefore, given probability p, all $p(k)$ can be obtained. As an example, a binomial random variablewith parameter $(100, 0.2)$ is plotted in Fig. 4.3.

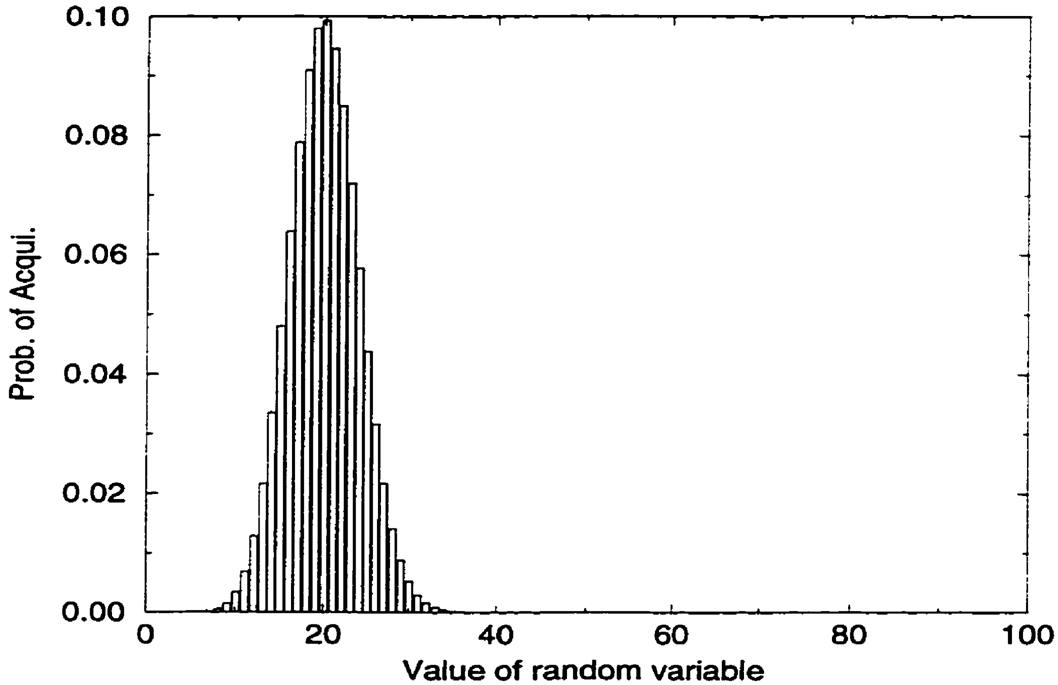

Figure 4.3: Probability mass distribution of a binomial random variable with parameter $(100, 0.2)$

4.2.2 Continuous Random Variables

Let X be a random variable. Variable X is called a continuous random variable if there exists a non–negative function f, defined for all real $x \in (-\infty, \infty)$, having the property that for any set B of real numbers

$$P\{X \in B\} = \int_B f_X(x)dx. \tag{4.3}$$

The function f_X is called the ***probability density function*** (pdf) of the random variable$X$. In the last subsection, the probability distribution is described by mass functions since those variables are discrete. To simplify the names of different functions without causing confusion, hereafter pdf is used for all types of random variables.

Equation (4.3) says that the probability that X will be in B may be obtained by integrating the pdf function $f_X(x)$ over the set B. If the set B contains all values X will take, then the probability is 1 as shown by (4.4)

$$P\{X \in (-\infty, \infty)\} = \int_{-\infty}^{\infty} f_{\mathbf{X}}(x)dx = 1. \tag{4.4}$$

A Gaussian, or normal, random variable is defined by pdf

$$f_{\mathbf{X}}(x) = \frac{1}{\sqrt{2\pi}\sigma} e^{-(x-\mu)^2/2\sigma^2} \qquad -\infty < x < \infty \tag{4.5}$$

where the parameters μ and σ^2 are the mean and the variance of a Gaussian random variable X respectively.

If X and Y are two independent, identically distributed (*iid*) Gaussian random variables with zero mean and variance σ^2, the joint density function of new random variables $R = \sqrt{X^2+Y^2}$ and $\Theta = \tan^{-1} Y/X$ is given by

$$f_{\mathbf{R},\Theta}(r,\theta) = \frac{r}{2\pi\sigma^2} e^{-r^2/2\sigma^2} \qquad 0 < r < \infty, \quad 0 < \theta < 2\pi \tag{4.6}$$

where Θ is uniformly distributed over $(0, 2\pi)$. R is the magnitude of the signal obtained from two independent quadrature components X and Y where both have the pdf in (4.5). As r and θ are independent, the pdf of the magnitude is obtained by integrating (4.6) from 0 to 2π with respect to θ. The magnitude follows the Rayleigh distribution [77].

$$f_{\mathbf{R}}(r) = \frac{r}{\sigma^2} e^{-r^2/2\sigma^2} \qquad 0 < r < \infty. \tag{4.7}$$

If at least one of the two Gaussian random variableshas a non–zero mean, the magnitude distribution becomes Rician as given in (4.8) [77]:

$$f_{\mathbf{R}}(r) = \frac{r}{\sigma^2} \exp\left(-\frac{r^2+a^2}{2\sigma^2}\right) I_0\left(\frac{ra}{\sigma^2}\right) \qquad 0 < r < \infty \tag{4.8}$$

where a is the mean of one random variablewhile the other random variablehas zero mean or is the amplitude from both components. When $a = 0$, (4.8) becomes (4.7). All three pdfs of continuous random variables described above are plotted in Fig. 4.4 with the same parameters a and σ.*

*Rayleigh pdf is produced with $a = 0$ using (4.8)

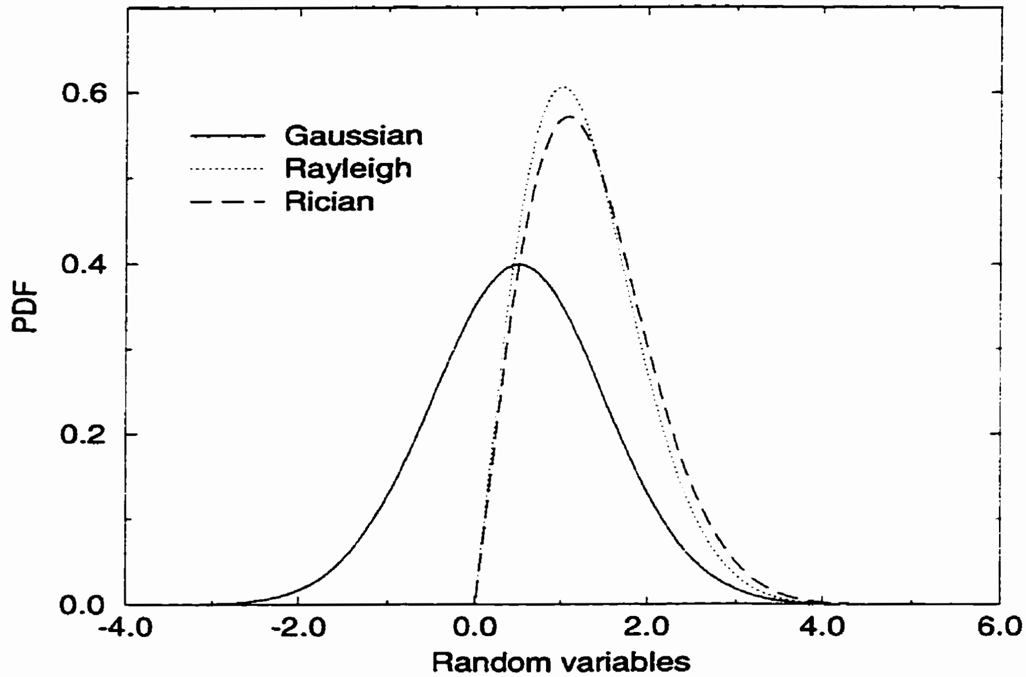

Figure 4.4: Graph of pdf of Continuous Random Variables ($a = 0.5, \sigma = 1$)

4.2.3 Estimation Theory

In this thesis, the synchronization problem is identified as the estimation of a non–random but unknown parameter, namely the propagation delay. A well established estimation procedure to perform the estimation is Maximum Likelihood Estimation (MLE).

Follow the work of Van Trees in [41], the estimation model is defined by four parts.

Parameter Space. The output of the source is a parameter. This parameter can be either random or deterministic but unknown.

Probabilistic Mapping from Parameter Space to Observation Space. It generates points in the observation space in accordance with the probability law specified.

Observation Space. This corresponds to a set of N observations. Each set can be thought of a point in an N–dimensional space. The point is denoted by a vector $\mathbf{r}$.

Estimation Rule. This is how the observation is related to the parameter to be estimated. A function of $\widehat{a}(\mathbf{r})$ is used to denote this estimation rule.

MLE involves study of the conditional probability $p_{\mathbf{R}|A}(\mathbf{r}|a)$ where a is a parameter from the parameter space A. The basic idea is to find the most likely parameter which will lead to the current observation without any a priori knowledge of the parameter.

If the observation of the parameter space is from a single experiment, one needs N such experiments to establish the N–dimensional vector. On the other hand, if the experiment itself is a repeated N trial, then the pdf can be used to perform the estimate directly. In general, the conditional probability $p_{\mathbf{R}|A}(\mathbf{r}|a)$ is viewed as a function of a, where a is the only unknown parameter to be estimated. This probability function is called the *likelihood function* denoted by

$$L(a) = p_{\mathbf{R}|A}(\mathbf{r}|a). \tag{4.9}$$

The estimate depends on the observation vector $\mathbf{r}$

$$\widehat{a} = \widehat{a}(r_1, r_2, \cdots, r_N) = \widehat{a}(\mathbf{r}). \tag{4.10}$$

$\widehat{a}$ is a random variable because all the observations, $\mathbf{r}$, are random variables.

There is no straightforward minimization procedure that will lead to the minimum variance unbiased estimate [41]. Therefore, any estimate should be examined by a set of criteria.

The first criterion is the expectation of the estimate. Using the definition of expectation in [77]

$$E[\widehat{a}(\mathbf{r})] = \int_{-\infty}^{\infty} \widehat{a}\, p_{\mathbf{R}|A}(\mathbf{r}|a) d\mathbf{r} \tag{4.11}$$

The possible values of this expectation can be grouped into three classes

- $E[\widehat{a}(\mathbf{r})] = a$, for all values of a. The estimate is called *unbiased*.

- $E[\widehat{a}(\mathbf{r})] = a + b$, where b is not a function of a. The estimate is said to have a *known bias*, b. Simple subtraction removes this bias.

- $E[\widehat{a}(\mathbf{r})] = a + b(a)$, as b is a function of a, it is undetermined. The estimate is said to have an *unknown bias*.

Because the estimate is a random variable, even for an unbiased estimate, a single result may be far away from the true value. Therefore, the variance of the estimate should be examined. The variance of an random variable$x$ is by definition [77]

$$\mathrm{Var}[x] = E\{x^2\} - (E\{x\})^2. \tag{4.12}$$

Therefore, the variance of the estimate is

$$\mathrm{Var}[\widehat{a}(\mathbf{r}) - (a + b(a))] = E\{[\widehat{a}(\mathbf{r}) - a]^2\} - b^2(a). \tag{4.13}$$

The second term is zero if the estimate is unbiased. For two unbiased estimates, the one with smaller variance is said to be more efficient. The estimate will have a variance no less than a non-zero positive number. This number is referred as *Cramér–Rao bound* (CRB). The theorem given below, applies to estimation of non–random parameters

Theorem. If $\widehat{a}(\mathbf{r})$ is any unbiased estimate of a, then

$$\mathrm{Var}[\widehat{a}(\mathbf{r}) - a] \geq (E\{[\frac{\partial \ln p_{\mathbf{R}|A}(\mathbf{r}|a)}{\partial a}]^2\})^{-1} \tag{4.14}$$

or, equivalently,

$$\mathrm{Var}[\widehat{a}(\mathbf{r}) - a] \geq (-E\{[\frac{\partial^2 \ln p_{\mathbf{R}|A}(\mathbf{r}|a)}{\partial a^2}]\})^{-1} \tag{4.15}$$

where the following conditions are assumed to be satisfied,

$$\frac{\partial \ln p_{\mathbf{R}|A}(\mathbf{r}|a)}{\partial a} \quad \text{and} \quad \frac{\partial^2 \ln p_{\mathbf{R}|A}(\mathbf{r}|a)}{\partial a^2} \tag{4.16}$$

exist and are absolutely integratable [41]. Equation (4.14) or (4.15) are commonly referred as the *Cramér–Rao inequality.* The expectations in both inequalities are the CRB. Any estimate that satisfies the bound with an equality is called an *efficient* estimate.

4.3 BER as an Uplink Timing Error Indicator

The propagation delay estimation based on monitoring the sample BER with a known input probing signal is discussed in this section. In the following chapters, unless for link BER test purposes, the BER is used to denote the sample bit error rate. The relationship between the BER and the timing offset is derived first. The imperfect channel which causes errors in the bit decision is represented by a binary symmetric channel (BSC) model with the probability of making incorrect decision p as shown in Fig. 4.5. The parameter p in the figure is the link probability of bit error. An equal probability of transmitting 0 or 1 is assumed on the uplink.

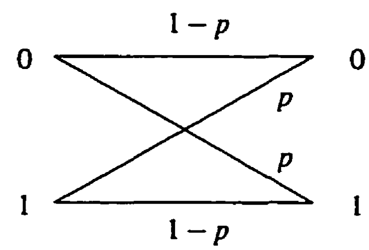

Figure 4.5: The Binary Symmetric Channel Model

A limitation to the BER as an uplink timing error measurement is that this function depends as well on carrier phase offset errors at the satellite receiver. The presentation to follow assumes perfect coherence in the satellite receiver and thus carrier phase offsets are neglected. Later, a better estimate of uplink timing that is robust relative to the carrier phase offset errors is developed.

4.3.1 Processor Outputs

In section 3.3, the general form of the CFT was presented. In this subsection, the CFT given by (3.5) from subsection 3.3.1 is applied to a QPSK modulated signal and the output of this process is given. Our goal is to derive an expression for timing measurement error from the received uplink signal.

The CFT of the input signal spans a finite time interval, as such, it is more appropriate to write the CFT output as

$$F(\mu t) = \int_{-\frac{T}{2}}^{\frac{T}{2}} f(\tau)\exp(-j(\mu t)\tau)d\tau \tag{4.17}$$

where now the transform is over one modulation symbol period. When the input to the processor is a data sequence with phase carrying the information, following the derivation in [35], one gets the output for the k-th channel for the m-th input symbol, denoted $\tilde{S}_{km}(\tau)$, with a time offset T_e included, from equation (4) in [35] as

$$\tilde{S}_{km}(\tau) = A_k T e^{j\phi_k}\{e^{j\alpha_{k,m}}\mathrm{sinc}(\frac{\beta T}{2}) + [e^{j\alpha_{k,m-1}} - e^{j\alpha_{k,m}}]\frac{e^{j\frac{\beta T}{2}} - e^{j\beta(\frac{T}{2}-T_e)}}{j\beta T}\}e^{-j\beta mT} \tag{4.18}$$

for $T_e > 0$. When A_k is the input signal amplitude and T is the symbol length, T_e and ϕ_k are the unknown timing and phase offsets, respectively. Also, $\alpha_{k,m}$ is the modulating phase in the m-th symbol interval for the k-th channel and ω_k is the angular frequency offset with respect to the center frequency. Finally, β is defined as $\beta = \mu(\tau - mT) - \omega_k$. $\tilde{S}_{km}(\tau)$ represents the Fourier transform of the input signal observed at time τ.

For $T_e < 0$, the output is given by [35]

$$\tilde{S}_{km}(\tau) = A_k T e^{j\phi_k}\{e^{j\alpha_{k,m}}\mathrm{sinc}(\frac{\beta T}{2}) + [e^{j\alpha_{k,m+1}} - e^{j\alpha_{k,m}}]\frac{e^{-j\beta(\frac{T}{2}-T_e)} - e^{-j\frac{\beta T}{2}}}{j\beta T}\}e^{-j\beta mT}. \tag{4.19}$$

The second terms within the square braces of equation (4.18) and equation (4.19) represent the interference introduced by the incorrect timing at the detection time. When timing is correct, or the two consecutive symbols are identical, this term vanishes. A complete discussion can be found in [35].

Further study of equation (4.18) and (4.19) shows that if the signal applied to the SAW processor changes phase by π every T as given in (4.20),

$$\alpha_{k,m-1} = \alpha_{k,m+1} = \alpha_{k,m} + \pi, \tag{4.20}$$

the $e^{j\alpha_{k,m-1}}$ (or $e^{j\alpha_{k,m+1}}$) term can be collapsed to $e^{j\alpha_{k,m}}$ multiplied by a negative sign as shown in (4.21) and (4.22),

$$e^{j\alpha_{k,m-1}} - e^{j\alpha_{k,m}} = -2e^{j\alpha_{k,m}}, \tag{4.21}$$

$$e^{j\alpha_{k,m+1}} - e^{j\alpha_{k,m}} = -2e^{j\alpha_{k,m}}. \tag{4.22}$$

By rearranging terms of dividing by $j\beta T$ in (4.18) and (4.19) as follows

$$\begin{array}{rcll} \frac{e^{j\frac{\beta T}{2}} - e^{j\beta(\frac{T}{2}-T_e)}}{j\beta T} & = & \frac{T_e}{T}\mathrm{sinc}(\frac{\beta T_e}{2})e^{j\frac{\beta}{2}(T-T_e)} & T_e \geq 0 \\ \frac{e^{-j\beta(\frac{T}{2}-T_e)} - e^{-j\frac{\beta T}{2}}}{j\beta T} & = & -\frac{T_e}{T}\mathrm{sinc}(\frac{\beta T_e}{2})e^{j\frac{\beta}{2}(T+T_e)} & T_e < 0, \end{array} \tag{4.23}$$

the whole output of (4.18) reduces to

$$\tilde{S}_{km}(\tau) = A_k T e^{j\phi_k} e^{j\alpha_{k,m}} \{\mathrm{sinc}(\frac{\beta T}{2}) - 2\frac{T_e}{T}\mathrm{sinc}(\frac{\beta T_e}{2})e^{j\frac{\beta}{2}(T-T_e)}\} e^{-j\beta mT} \qquad T_e \geq 0 \tag{4.24}$$

by applying conditions for $T_e > 0$ in (4.23). For $T_e < 0$, using (4.23), equation (4.19) is simplified to

$$\tilde{S}_{km}(\tau) = A_k T e^{j\phi_k} e^{j\alpha_{k,m}} \{\mathrm{sinc}(\frac{\beta T}{2}) + 2\frac{T_e}{T}\mathrm{sinc}(\frac{\beta T_e}{2})e^{j\frac{\beta}{2}(T+T_e)}\} e^{-j\beta mT} \qquad T_e < 0. \tag{4.25}$$

Further discussion can be concentrated on the $T_e > 0$ case given in (4.24) since both cases result in identical output amplitudes. The signal described by equation (4.24) is sampled when $\beta = 0$ or equivalently when $\tau = \omega_k/\mu + mT$. The sample is a complex value containing the modulation information and the unknown phase offset. The samples from different FDMA channels in sequence form the basis of the time multiplexed signal that becomes the TDM downlink signal. The phase offset ϕ_k in (4.24) and (4.25) can be removed in practice using a digital PLL following the MCD.

When the change phase by π signal is used as a probing signal, from (4.24) and (4.25), the signal amplitude at the sampling instant when $\beta = 0$ is

$$|\tilde{S}_{km}(\tau = \frac{\omega_k}{\mu} + mT)| = A_k T(1 - 2\frac{|T_e|}{T}). \tag{4.26}$$

By taking the absolute value of T_e as shown in (4.26), only half the symbol timing offset should be considered because the other half of the timing offset will yield identical results. From (4.26), the sampled signal amplitude is linearly related to the timing offset on the uplink. Due to the limitation of the output of the SAW based MCD, this relationship cannot identify the polarity of the timing offset.

When the output signal phase is treated as above, the BER becomes the function of the signal amplitude which is the true signal amplitude plus the white Gaussian noise in [25]. Let the noise power at the output of the MCD be σ^2. Then, the BER is given as a function of timing offset as

$$p = Q(\frac{A_k T(1 - 2|\lambda|)}{\sigma}) \tag{4.27}$$

where $\lambda = T_e/T$ is the normalized timing offset with respect to symbol period T and the Q function is defined as [21]

$$Q(x) = \frac{1}{\sqrt{2\pi}} \int_x^\infty \exp(-\frac{r^2}{2}) dr. \tag{4.28}$$

Finally, it is worthwhile to indicate that the noise power at the output of the MCD is [35]

$$\sigma^2 = \frac{N_0 T}{2}. \tag{4.29}$$

σ^2 is needed only for performance analysis and is not needed to realize the propagation delay estimate.

4.3.2 BER Computation

In a processing satellite system, the uplink and downlink bit decisions are independent. When both links are represented by the similar BSC channels shown in Fig. 4.5, the round trip link can be considered as two such a BSCs in a series connection and the round trip BER, therefore, can be calculated as

$$p = (1 - p_u)p_d + (1 - p_d)p_u \tag{4.30}$$

where the subscripts u and d indicate that the bit error rates are of the uplink or downlink respectively. The equation states that the round trip BER is the sum of the products of the probability of correct transmission on one link and the probability of error on the other link. When the BERs of both links are small, the product term $p_u p_d$ can be ignored. Then the round trip BER becomes

$$p \approx p_u + p_d. \tag{4.31}$$

This equation gives an approximation of the round trip BER. Because incorrect delay compensation on the uplink reduces the effective output signal level of the on–board processor as shown in (4.26), the uplink BER will be degraded as in (4.27). The downlink BER can be considered as a constant over the uplink acquisition period for a given SNR of the downlink since the timing and carrier recovery of the downlink receiver are performed at the ground terminal and the ground terminal receives the fast TDM downlink for all users. In reality, the downlink could always be regarded as on. On the other hand, the unknown propagation path delay at acquisition causes changes of the uplink BER, and thus also the round trip BER in (4.31), observed at the ground terminal. Further treatment of round trip BER will be given in the subsection 4.3.4. Now the round trip BER is related to the delay estimation on the sense of modulo T through (4.27), where T is the symbol period. The typical BER vs. time offset curve in an AWGN environment for signal to noise ratio, which is defined as

$$\text{SNR} = \frac{E_b}{N_0} = \frac{(A_k/\sigma)^2}{2} \tag{4.32}$$

of 4 dB is given in Fig. 4.6. In subsection 4.3.5, this curve, or its equivalent, equation

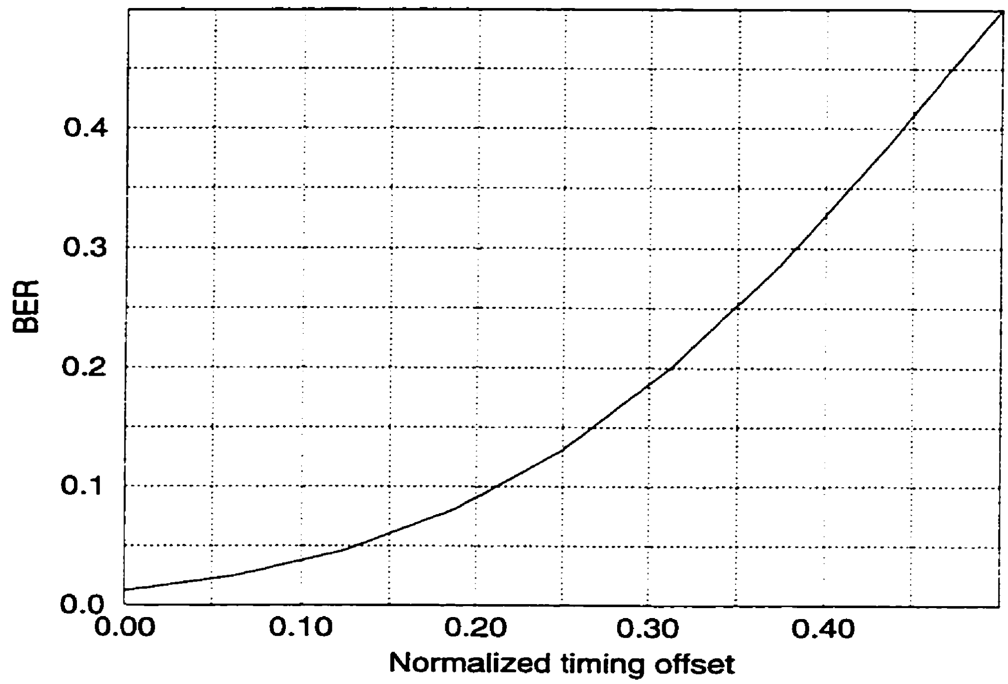

Figure 4.6: Bit Error Rate vs. Time Offset (SNR=4dB)

(4.27) is used to estimate the timing offset from the BER. A rectangular shaped pulse is assumed for the calculation. The timing offset is used as the argument. Because the curve is symmetric for the timing offset either leading or retarding from the correct timing point, only half of the measurement curve is plotted in Fig. 4.6. As the BER is a designed system parameter for a given SNR, once the BER is found not close to the expected value, it can be concluded that the delay estimation is incorrect. Hence, monitoring the BER can provide time offset information as once the BER with a timing offset is determined, the amount of the offset can be found from Fig. 4.6. This offset then can be compensated by setting a proper transmitting delay in the earth terminal.

The method of determining the BER is to interpret the error frequency as the BER. This method requires a known link SNR. To use this method, a given data sequence of N symbols is transmitted and the number of incorrect decisions, N_e, is counted. The ratio N_e/N is interpreted as the BER. The BER is essentially a probability of making error decisions on the individual symbols. If let p represent this error probability, then from Bernoulli's theorem (one of the law of large numbers [77])

$$\lim_{N\to\infty} P\{|\frac{N_e}{N} - p| < \varepsilon\} = 1 \tag{4.33}$$

where N is the number of symbols transmitted, N_e is the number of error decisions and ε is an infinitesimal positive number. In this case, symbol observations can be considered as independent trials. This theorem says that the error probability can be determined precisely only when the number of transmitted symbols is infinite.

In a real system only a finite number of symbols can be transmitted to estimate the value of p. It is desirable to minimize the number of symbols used for determining p as this process is an overhead to the system capacity when the process is associated with a call set up. In the following subsection, how p is estimated using a maximum likelihood estimation method is discussed.

4.3.3 Estimation of Error Probability p

First a random variableX_k is introduced to represent the symbol decision process at the receiver. The subscription k here indicates that it is the k-th symbol which is under consideration. The decision process is represented as

$$X_k = \begin{cases} 0, & \text{if } k\text{-th symbol is correct.} \\ 1, & \text{if } k\text{-th symbol is incorrect.} \end{cases}$$

Let p be the probability of making an incorrect decision, then a Bernoulli probability density function as given in (4.1) is obtained. This function can also be written as

$$P(X_k = x) = p^x(1-p)^{1-x} \qquad x = 0 \quad \text{or} \quad 1. \tag{4.34}$$

To find the probability of $x = 1$, N symbols are sent to the receiver and all N random variables are *iid*. The received symbols represent the samples obtained from a Bernoulli distributed population. As mentioned in section 4.2.3, the N–dimensional vector $\mathbf{x}$ in the observation space is obtained from these repeated trials. The joint pdf of these Bernoulli random variables is

$$\begin{aligned}
P(X_1 = x_1, X_2 = x_2, \cdots, X_N = x_n) &= P(X_1 = x_1)P(X_2 = x_2)\cdots P(X_N = x_N) \\
&= \prod_{i=1}^{N} p^{x_i}(1-p)^{1-x_i} \qquad x_i = 0 \quad \text{or} \quad 1. \\
\therefore \quad P(\mathbf{X} = \mathbf{x}) &= p^{N_e}(1-p).^{N-N_e} \qquad (4.35)
\end{aligned}$$

Where N_e is the number of incorrect decisions ($x_i = 1$) in N trials. It is a random variable. $\mathbf{X}$ is a random vector with N random variables X_k. $\mathbf{x}$ is the outcome vector of N trials. Equation (4.35) is the likelihood function as defined by (4.9) in section 4.2.3. The log–likelihood function for (4.35) is

$$L(p) = N_e \ln p + (N - N_e)\ln(1-p). \qquad (4.36)$$

The goal is to look for an estimate of p which maximizes (4.36). The maximum can be obtained by differentiating $L(p)$ with respect to p and setting the result equal to zero

$$\frac{\partial L(p)}{\partial p} = 0. \qquad (4.37)$$

The estimate of the error probability then can be solved from this equation and the result is

$$\widehat{p} = \frac{N_e}{N}. \qquad (4.38)$$

The estimated error probability is evaluated next. The number of errors in N trials obeys the binomial distribution as each decision is a Bernoulli random variable. From the observation space, the number of errors is a random variable with parameters (N, p)

$$P(X = N_e) = \binom{N}{N_e} p^{N_e}(1-p)^{N-N_e}. \qquad (4.39)$$

The expected value of N_e is

$$E[N_e] = Np \qquad (4.40)$$

and the variance of N_e is

$$\mathrm{Var}[N_e] = E[(N_e - E[N_e])^2] = Np(1-p). \tag{4.41}$$

Since N is a constant, the expected value of $\widehat{p}$ becomes

$$E[\widehat{p}] = \frac{E[N_e]}{N}. \tag{4.42}$$

Substituting (4.40) into the last equation and the mean of $\widehat{p}$ is obtained as

$$E[\widehat{p}] = \frac{Np}{N} = p. \tag{4.43}$$

Therefore, the estimate of p in (4.38) is *unbiased.* The time delay estimate can be computed from the bit error probability using (4.27). Since the resulting time estimate is MLE if the p estimate is MLE [42], the performance discussion of the estimate is based on the bit error estimate instead of working on the time estimate directly.

Next, the efficiency of the estimate is determined. The efficiency of the estimate is evaluated by its variance. The estimate is efficient when its variance equals the Cramér–Rao bound in equation (4.15). The Cramér–Rao bound is calculated from the log likelihood function. For the log likelihood function $L(p) = N_e \ln p + (N - N_e)\ln(1-p)$, the CRB is calculated using (4.15) by first taking the second order derivative of $L(p)$

$$\frac{\partial^2 L(p)}{\partial p^2} = -\frac{N_e}{p^2} - \frac{(N-N_e)}{(1-p)^2} \tag{4.44}$$

Then upon use of the binomial probability density function (4.2), the CRB, denoted below as I_R, is given by

$$I_R = (-E\{[\frac{\partial^2 L(p)}{\partial p^2}]\})^{-1} = \frac{p(1-p)}{N}. \tag{4.45}$$

The variance of the estimate can be calculated for this particular case as

$$\mathrm{Var}[\widehat{p}] = E[(\widehat{p} - E[\widehat{p}])^2] = E[(\frac{N_e}{N})^2] - p^2. \tag{4.46}$$

Since, by the binomial pdf in (4.2),

$$\begin{aligned} E[N_e^2] &= E[N_e(N_e-1)+N_e] = N(N-1)p^2+Np \\ &= Np(1-p)+(Np)^2 \end{aligned} \tag{4.47}$$

and substitution of (4.47) into (4.46) gives

$$\mathrm{Var}[\widehat{p}] = \frac{Np(1-p)+(Np)^2}{N^2} - p^2 = \frac{p(1-p)}{N}. \tag{4.48}$$

Therefore,

$$\mathrm{Var}[\widehat{p}] = I_R. \tag{4.49}$$

and the variance of the estimate equals its lower bound. The estimate of p in (4.38) is thus an efficient estimate.

In the next subsection, the effect of parameters such as p and N on the CRB is discussed.

4.3.4 Discussions of the Cramér–Rao bound

In subsection 4.3.2, the round trip BER was discussed briefly and in subsection 4.3.3, the estimation performance evaluation criterion was established. In this subsection, the BER estimation performance is discussed in detail. The discussion starts with the assumption that satellite downlink does not introduce any errors to the round trip BER. In this case, the uplink error probability p_u is non–zero and the downlink error probability p_d is zero. The round trip BER of (4.30) is simplified to

$$p = p_u. \tag{4.50}$$

The CRB I_R of the round trip error probability estimate in (4.45) will be

$$I_R = \frac{p(1-p)}{N} = \frac{p_u(1-p_u)}{N}. \tag{4.51}$$

In Fig. 4.7, the CRB given by (4.51) is plotted against the number of symbols observed while SNR, as defined in (4.32), is used as a parameter. As indicated in (4.27), timing

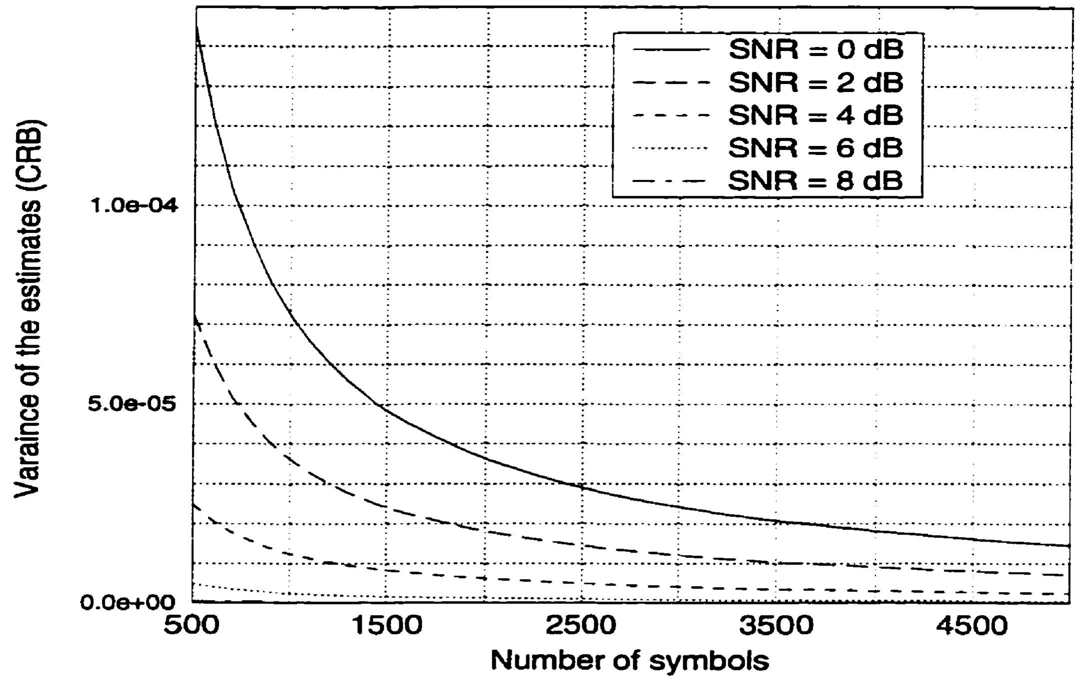

Figure 4.7: CRB Dependence on Number of Symbols and SNR

error reduces the effective link SNR, and of course increases the link bit error rate p. To illustrate the effect of probing sequence length on the variance of the estimate, without losing generality, a zero timing offset is used to produce Fig. 4.7. Different p_u's are used in the plot and the p_u's are determined by SNRs through (4.27) where $\lambda = 0$ is used when using this equation.

The results show that increasing the number of samples (or observed symbols) reduces the variance of the estimate. For a given sample size, N, the variance decreases as p decreases, or equivalently as the SNR increases. This is because when p is less than 0.5, I_R is a monotone function of p for a fixed value of N as shown by (4.45). In Fig. 4.8, the CRB given by (4.51) is plotted against SNR. Note here, to convert SNR to p, one must use equation (4.27). No timing error, *i.e.* $\lambda = 0$, is assumed in Fig. 4.8. Again, the curves show that a smaller lower bound is obtained for higher SNR and/or more samples used in the estimate of p. For $\lambda \neq 0$, the effective SNR would be lower and therefore one can expect larger variance with the same sample size.

Next, the error–free downlink assumption is removed which gives a non–zero p_d and

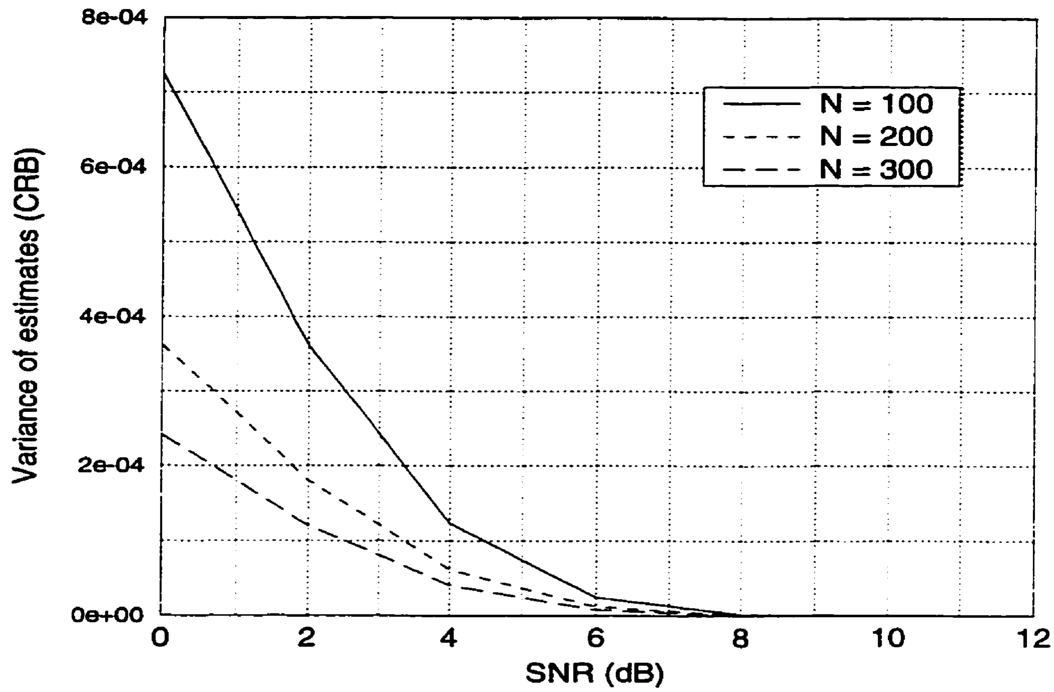

Figure 4.8: CRBs vs. SNR for various sampling size N

the round trip error probability is then governed by (4.52) below which is a rearrangement of (4.30) of subsection 4.3.2.

$$p = p_u + p_d - 2p_d p_u. \tag{4.52}$$

It is recognized from (4.52) that when using the round trip bit error rate p to represent the uplink error probability introduces an unknown bias (see page 54) to the estimate of p_u. The bias is $p_d - 2p_d p_u$, where p_u is the function of p_d. Since the uplink and downlink of the satellite channels can be collectively considered as a simple DSC channel with error probability of p, the estimate $\hat{p}$ is unbiased with regard to p. The CRB for $\hat{p}$ is derived first. Then the CRB can be grouped to the normal term due to p_u, and the disturbing term due to p_d. Here the normal term means the one containing the uplink timing error information only. The disturbing term is the one which introduces more uncertainty to the estimation. Substitution of p in (4.52) into (4.45) and the numerator in (4.45) becomes

$$p(1-p) = p_u + p_d - 2p_u p_d - (p_u + p_d - 2p_u p_d)^2$$

$$
\begin{aligned}
&= p_u - p_u^2 + p_d - p_d^2 - 4p_u p_d + 4p_u^2 p_d + 4p_u p_d^2 - 4p_u^2 p_d^2 \\
&= p_u - p_u^2 + p_d((1-2p_u)^2 - p_d(1-4p_u+4p_u^2)) \\
&= p_u(1-p_u) + (1-2p_u)^2 p_d(1-p_d).
\end{aligned}
$$

Then the CRB in (4.45) can be written as

$$
I_{R(\text{total})} = \frac{p_u(1-p_u)}{N} + \frac{(1-2p_u)^2 p_d(1-p_d)}{N}. \tag{4.53}
$$

The first term in (4.53) is the variance of the uplink error probability estimation given by (4.51) and the second term is the disturbance introduced by the imperfect downlink. When $p_d = 0$, (4.53) becomes (4.51). For $p_u \gg p_d$, the disturbance can be ignored. Then the CRB reduces to

$$
I_{R(\text{total})} = \frac{p_u(1-p_u)}{N} = I_{R(\text{up})}. \tag{4.54}
$$

This fact is demonstrated in Fig. 4.9 to Fig. 4.11. In these figures, $p_u = 1.25 \times 10^{-2}$ is fixed for a given uplink SNR = 4 dB while the p_d is varied with different SNRs. The results show that for $p_u \geq 10 \times p_d$, the resulting CRB of the round trip $\widehat{p}$ is very close to the CRB of the uplink $\widehat{p}_u$. It is clear, in Fig. 4.11, that p_d has almost no effect on the total CRB. This figure shows the case when SNR = 4 dB, $p_u = 1.25 \times 10^{-2}$ and $p_d = 2.16 \times 10^{-4}$ for SNR = 8 dB on the downlink. Equation (4.54) is thus justified.

Since the downlink BER is controllable from the system design phase it is considered as a known parameter. During the initial uplink timing acquisition period, $p_u \gg p_d$ and therefore, p_d has little impact on the estimation procedure. p_d is small because the downlink is synchronized in the receiver terminal. From (4.31), if p is considered as the estimate of p_u, the estimate is a biased one with the bias being p_d. For $p_u \geq 10\,p_d$, the bias can be ignored.

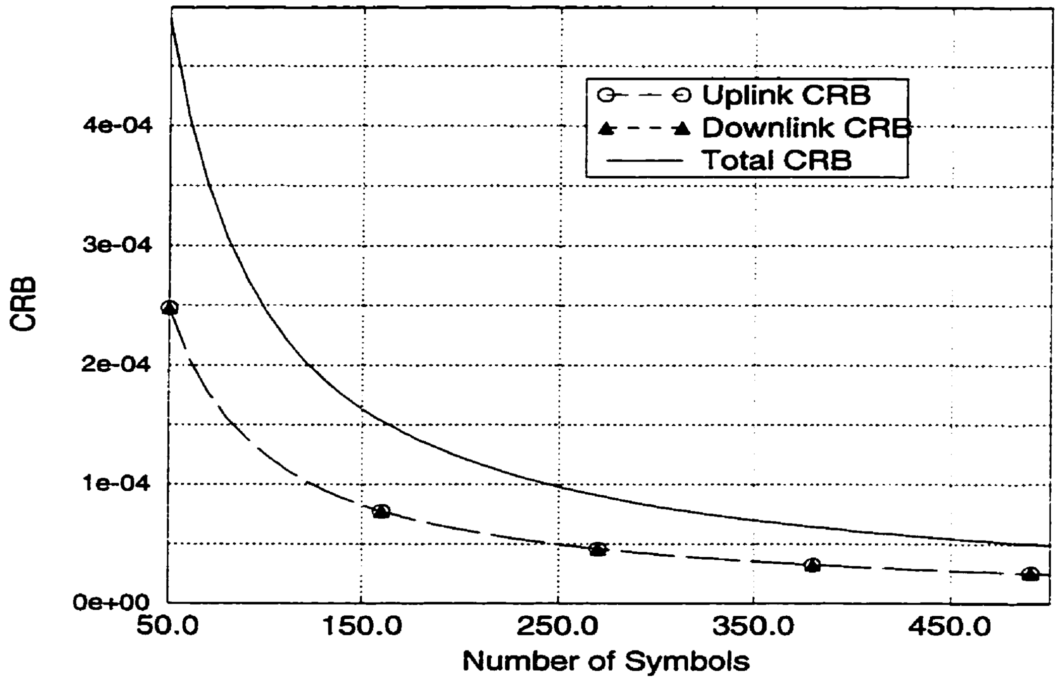

Figure 4.9: Comparison of the CRB of round trip $\widehat{p}$ and uplink CRB for $p_d = 1.25 \times 10^{-2}$

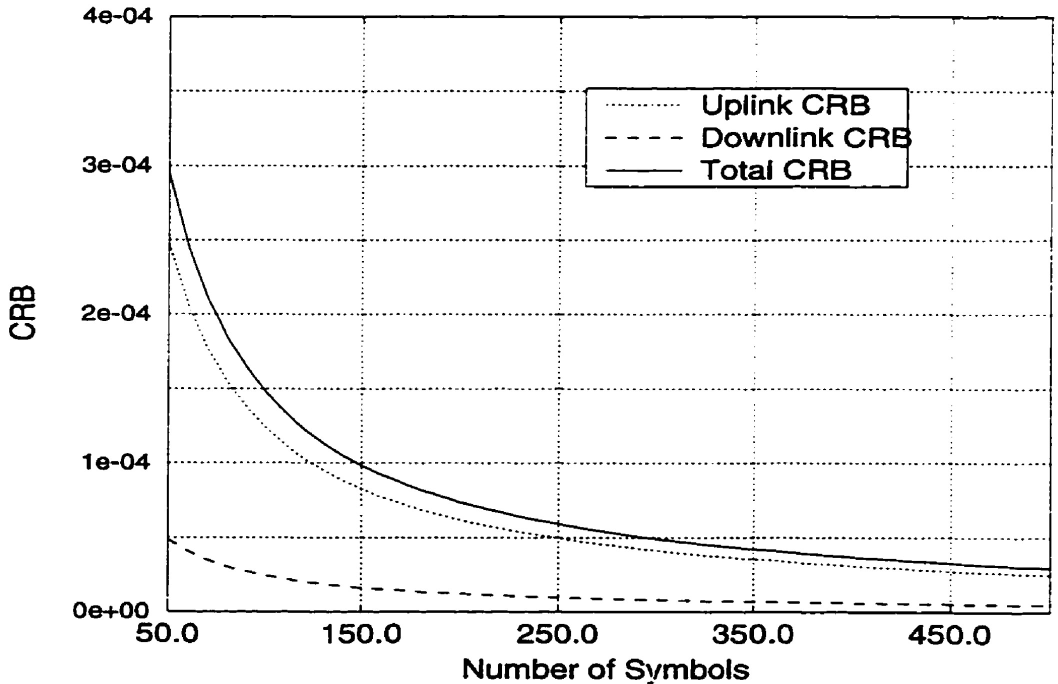

Figure 4.10: Comparison of the CRB of round trip $\widehat{p}$ and uplink CRB for $p_d = 2.45 \times 10^{-2}$

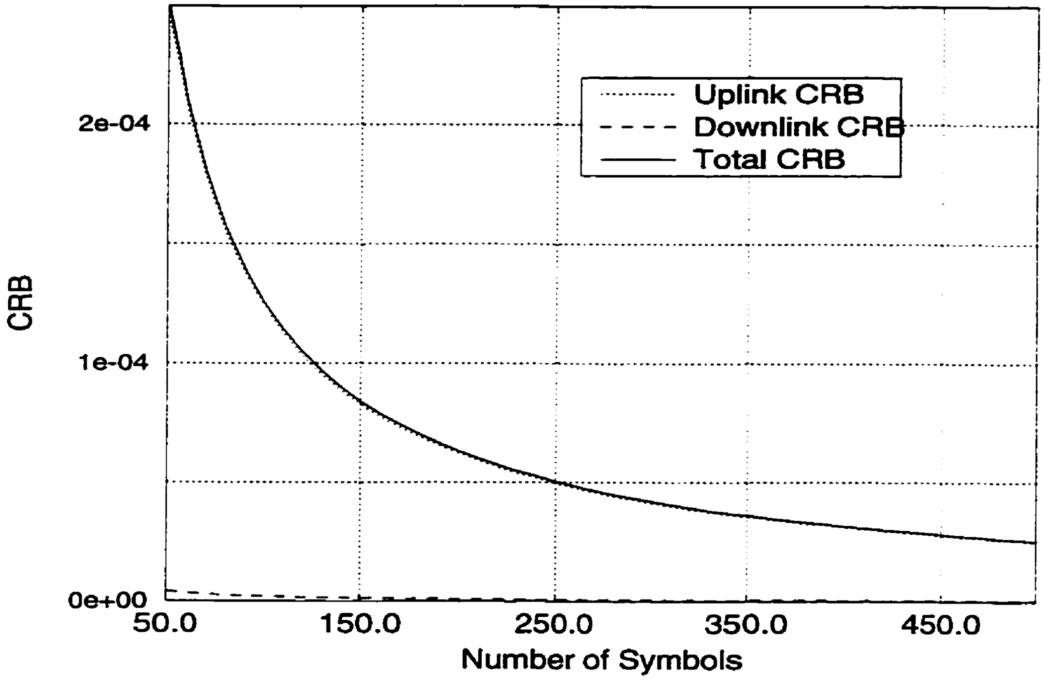

Figure 4.11: Comparison of the CRB of round trip $\widehat{p}$ and uplink CRB for $p_d = 2.16 \times 10^{-4}$

4.3.5 Estimation of Timing Error

After the uplink BER is estimated, it is possible to determine the timing offset from the optimum sampling instant using Equation (4.27) as was illustrated in Fig. 4.6. The timing estimate computed from p is maximum likelihood estimate [42]. Questions such as how accurate this estimation is, how fast the estimate is obtained, and what the SNR penalty is if there is remaining error are of interest. These questions are answered in this subsection.

The estimation procedure using the BER as an indicator is

1. Estimate the round trip BER at the ground terminal.

2. Compute timing offset from (4.27).

Let Q^{-1} denote the inverse function of (4.27). Then solve for the normalized timing offset as

$$\lambda = \frac{1 - kQ^{-1}(p)}{2}. \tag{4.55}$$

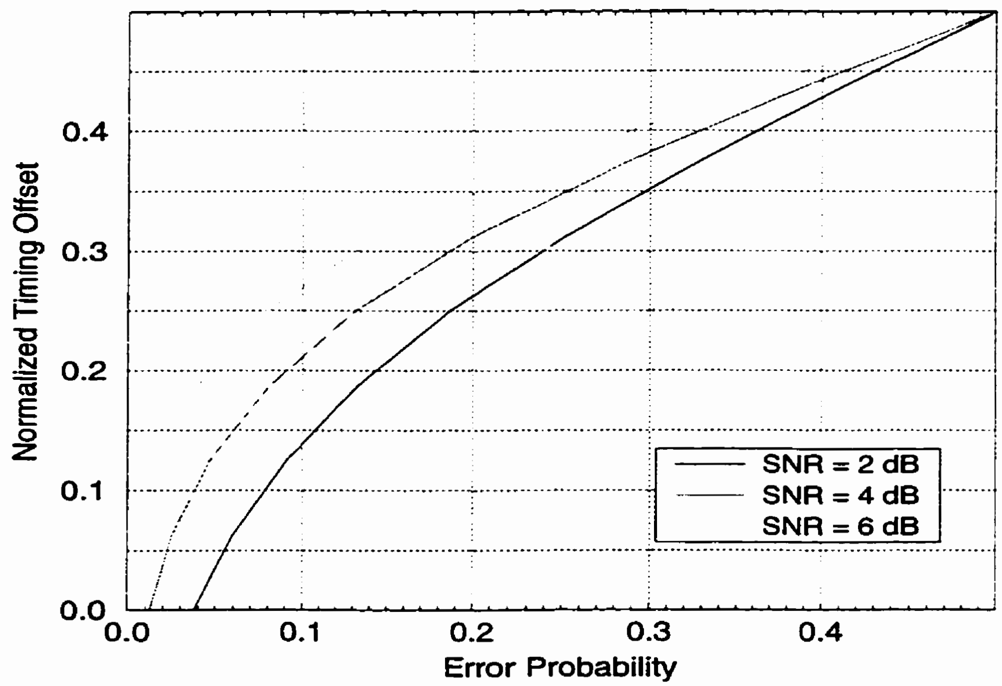

Figure 4.12: Offset as a function of BER

Here k is a constant which depends only on the system parameters such as the signal power, the symbol length and the channel noise. From (4.27), $k = \sigma/A_k T$. The timing offset can be computed from this function, which is plotted in Fig. 4.12 with different SNRs. Note that different SNRs lead to different curves. To get the estimate of the timing offset, the SNR must be specified. It is known that if $\widehat{p}$ is an ML estimate of p and $t = g(p)$ has a single valued inverse function, then $g(\widehat{p})$ is the maximum likelihood estimate of $g(p)$ [42]. Because the BER estimate is a random variable, the timing error estimate as a function of the BER is also a random variable. Since an ML estimate is asymptotically Gaussian [41], the probability of the estimate falling in a given interval can be calculated for a fixed number of samples. In other words, if the probability of the estimate falling in an interval is given, the variance of the estimate can be computed and the sample size can be determined from the variance according to the CRB given in (4.45).

The closeness of an unbiased or approximately unbiased estimate to its true value is discussed in subsection 4.3.4. From the previous figures, by noting that the BER itself is a relatively small value for a practical communication system, a large number of symbols is required to achieve a standard deviation less than or equal to 5 percent of the BER to be estimated. For example, to determine the range of the timing estimate, a testing SNR $= 4$ dB is specified. For a timing offset of $T/3$, using $N = 1000$ symbols, an error probability of $p = 2.23 \times 10^{-1}$, and $I_R = 1.73 \times 10^{-4}$, are expected. Then from Fig. 4.12, the timing estimate would be in a range of [0.32, 0.336]. Therefore, if the SNR is specified and an estimate is made close to the CRB, a delay estimate with small variances can be obtained.

In the previous section, the mean and the variance of the BER estimate have been determined and the approximate Gaussian pdf is readily given as [77]

$$f(\widehat{p}) = \frac{1}{\sqrt{2\pi}\sigma_p} \exp(-\frac{(\widehat{p}-p)^2}{2\sigma_p^2}) \tag{4.56}$$

where σ_p^2 is the variance of the estimate. It equals to the lower bound computed from Cramér–Rao inequality in (4.45) as

$$\sigma_p^2 = \frac{p(1-p)}{N}. \tag{4.57}$$

For simpler discussion, the estimate is normalized. The normalized random variable$x$ has zero mean and unity variance

$$x \triangleq \frac{\widehat{p}-p}{\sigma_p} \tag{4.58}$$

and is described by

$$f(x) = \frac{1}{\sqrt{2\pi}} \exp(-\frac{x^2}{2}) \tag{4.59}$$

where $f(x)$ is symmetrical about its mean value of 0. If the required probability of the normalized BER estimate in an interval $[-u_{\alpha/2}, u_{\alpha/2}]$ is $1-\alpha$, the value of $u_{\alpha/2}$ can be obtained by solving

$$\frac{\alpha}{2} = \int_{u_{\frac{\alpha}{2}}}^{\infty} f(x)dx \tag{4.60}$$

where $f(x)$ is the pdf given by (4.59). The remaining timing error is defined as zero if the estimate falls in the range of $[-u_{\alpha/2}, u_{\alpha/2}]$. Therefore the probability of timing is still incorrect after the correction based on the estimate is α. This value can be pre–defined in the system design phase. For example, if a confidence probability of 0.95 as $1-\alpha$ is specified, the required normalized interval $u_{\alpha/2}$ is 1.96. The actual error probability estimate interval is $p \in p \pm u_{\alpha/2}\sqrt{CRB}$ and the interval is a function of the length of the testing sequence. In the next section, the performance of the estimation method, named as error probability method (EPM), is studied through computer simulation. The theoretical results will be given in the mean time using the material provided here.

4.4 Simulation and Analysis of the EPM

The uplink delay estimate using the BER as an indicator is examined through simulation in this section. Computer simulation is used to show the probability distribution of the estimate in terms of the bit error probability. The timing offset vs. bit error probability for a given SNR is compared with the theoretical results from subsection 4.3.5.

Let $N = 1000$ known symbols which forms the probing sequence be transmitted over an AWGN channel. Then the number of errors N_e at the receiver side are counted. The estimated BER is obtained by dividing this number by N, that is $\widehat{p} = N_e/N$ as given by (4.38). Repeating this process M times, each time one $\widehat{p}$ is obtained, the probability distribution of the estimated BER is obtained. The simulation result for $N = 1000$ and $M = 5000$ with SNR $= 4$ dB is plotted in Fig. 4.13. The corresponding average BER for the given SNR is $p = 0.012538$ when timing is correctly aligned. Those ripples for which $k > 20$ errors are the result of a small number of estimates used to obtain the distribution. A theoretical pdf of a binomial random variabledescribed by Eqn. (4.2) with the same parameters is plotted as impulses in Fig. 4.13 as a reference. The simulation result is close to the theoretical in all segments of the curve.

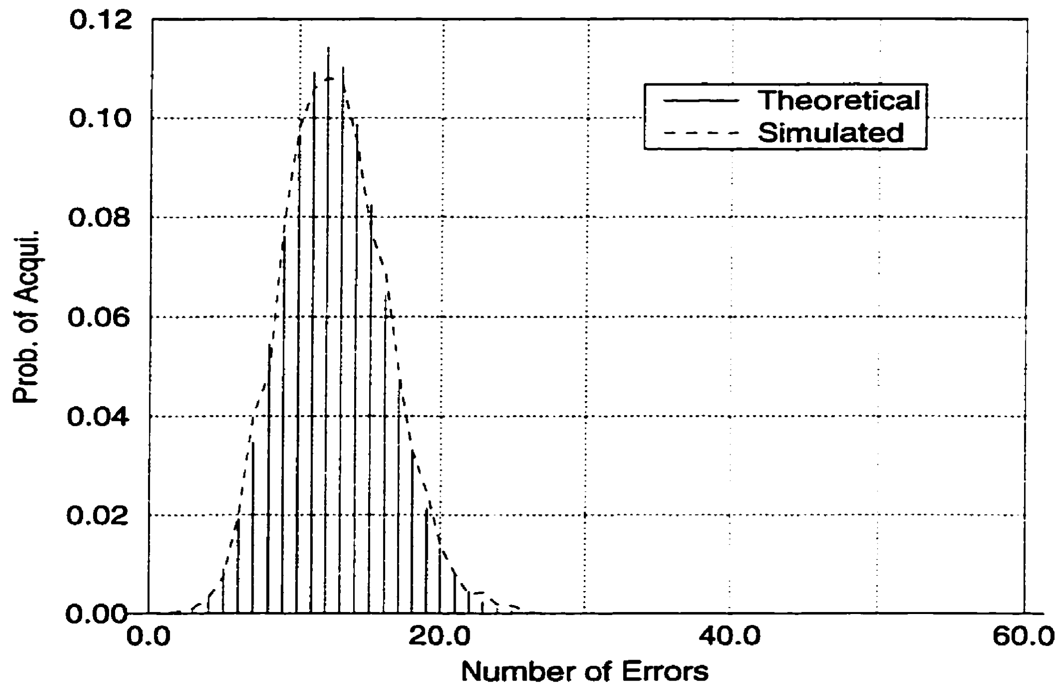

Figure 4.13: Binomial Distribution with $N = 1000$, $p = 0.012538$

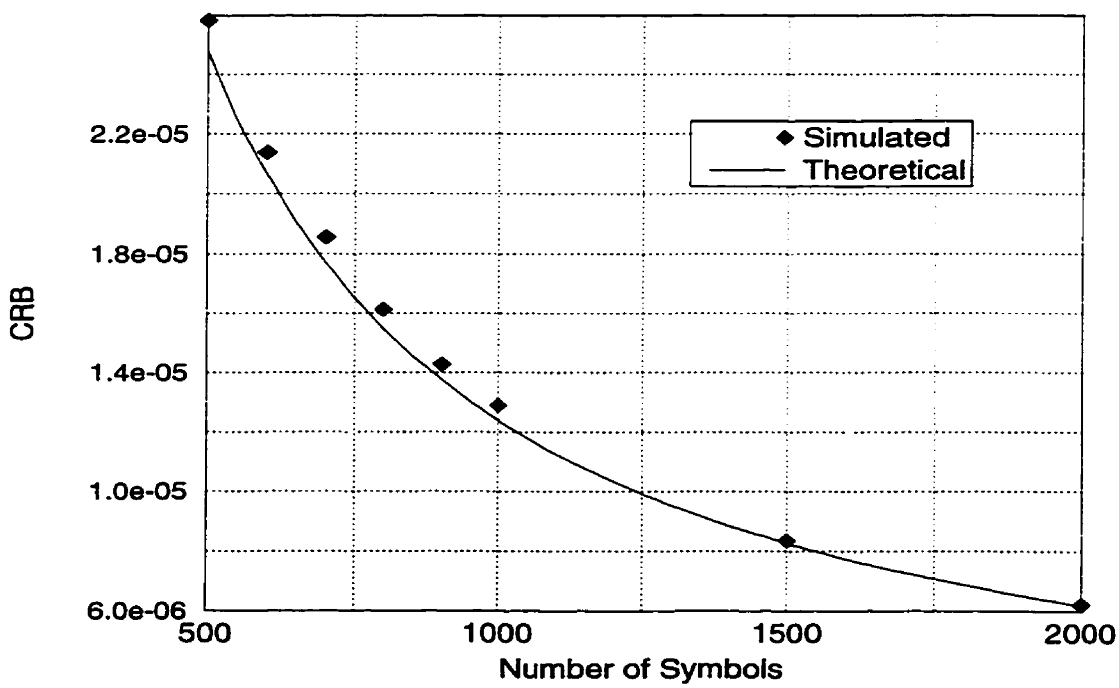

Figure 4.14: Simulation results of CRB ($\lambda = 0$, SNR=4dB)

The variance of this estimate can be computed from the probability distribution obtained from the procedure discussed above by an analytical method using (4.45). This variance is the Cramér–Rao Bound (CRB) on the BER because this estimate is efficient as was shown in section 4.3.3. Some variances computed from simulated $\hat{p}$ for different N are plotted as discrete points in Fig. 4.14. The theoretical CRB is calculated using (4.45) and is plotted as a continuous line in the same figure. The simulation results are in good conformity with the theoretical ones as the difference between theory and simulation is less than 10%. Since the estimated error probability has a confidence probability of 0.95 as stated in section 1.5 the confidence interval for the CRBs in Fig. 4.14 can be determined as follows.

Let $u = \Delta \times p$ be the half of the confidence interval of the error probability estimate, where Δ is defined as the percentage of the mean of the estimate, the upper range for the CRB values in Fig. 4.14 can be obtained from

$$\frac{(\widehat{p}+u)(1-\widehat{p}-u)}{N} = \frac{\widehat{p}(1-\widehat{p})}{N} + \frac{u(1-u)-2\widehat{p}u}{N} \tag{4.61}$$

and

$$\frac{(\widehat{p}-u)(1-\widehat{p}+u)}{N} = \frac{\widehat{p}(1-\widehat{p})}{N} - \frac{u(1+u)+2\widehat{p}u}{N}. \tag{4.62}$$

The second term in (4.61) is the upper value of the simulated CRB and is denoted as

$$I_u = \frac{u(1-u)-2\widehat{p}u}{N}. \tag{4.63}$$

The second term in (4.62) is the lower value of the simulated CRB and is denoted as

$$I_l = \frac{u(1+u)+2\widehat{p}u}{N}. \tag{4.64}$$

The confidence interval for a 95% confidence probability for the simulated CRB then is given as $[I_l, I_u]$. As an example, for $N = 1000$ and SNR=4 dB, the 95% confidence interval given in a form of $[I_R - I_l, I_R + I_u]$ is $[1.12 \times 10^{-5}, 1.34 \times 10^{-5}]$, where $I_R = 1.23 \times 10^{-5}$.

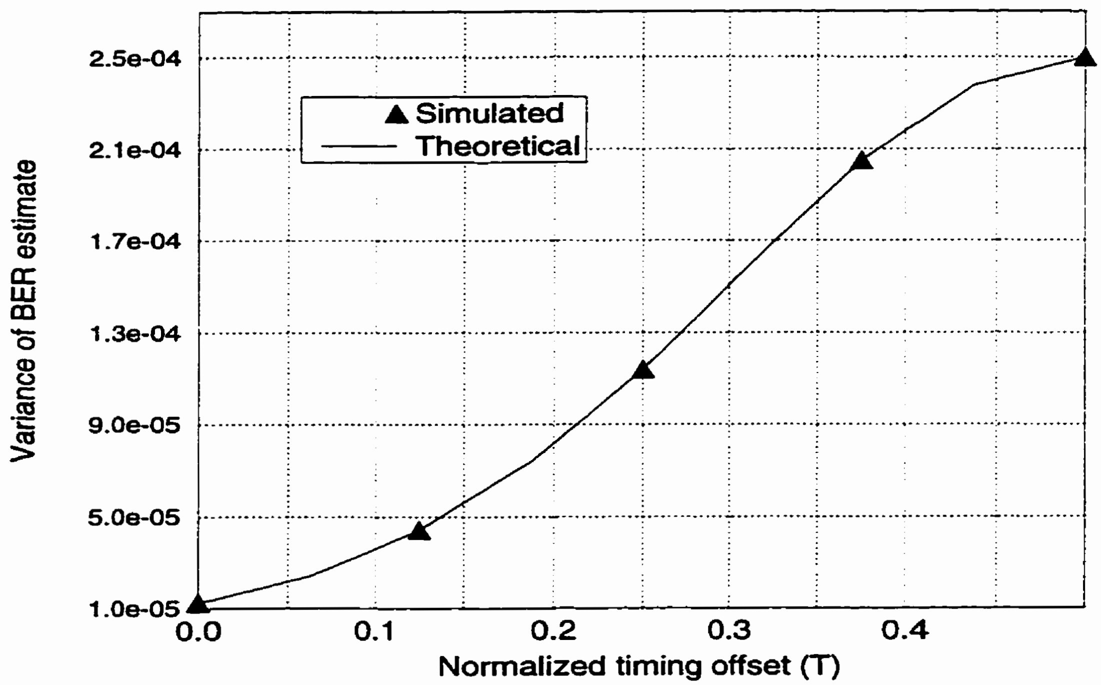

Figure 4.15: Variance as a function of Timing Offset ($N = 1000$)

The variance values could be better if more estimates $\widehat{p}$ were used to calculate $\mathrm{Var}[\widehat{p}]$, but the accuracy in Fig. 4.14 is sufficient for this study.

Since $\widehat{p}$ is a function of the timing offset, which is measured as a percentage of symbol length T, for a fixed length of a probing sequence with given SNR, the CRB changes as $\widehat{p}$ changes. For $0 < p < 0.5$, $p(1-p)$ is monotone increasing and therefore the variance increases as $\widehat{p}$ increases. This phenomenon is shown in Fig. 4.15. In the figure, the variance of estimated BER is computed directly from the simulated pdf of the estimated BER using

$$\mathrm{Var}[\widehat{p}] = \frac{\sum_k (k - \overline{N}_e)^2}{N^2} \qquad k = 0, 1, \cdots N \tag{4.65}$$

where $\overline{N}_e$ is the mean of the number of errors in a probing sequence and k is the possible number of errors in each probe. For each given timing offset, (4.65) is used to get the variance for the offset. The estimate confidence interval can be treated as in (4.61) and (4.62). The estimate sequence length $N = 1000$ is used for this plot. The theoretical CRB in (4.45) as a function of the normalized timing offset λ, which is defined in section 4.3.1, is given in the figure as a reference plot. The plot is obtained through two functions. First,

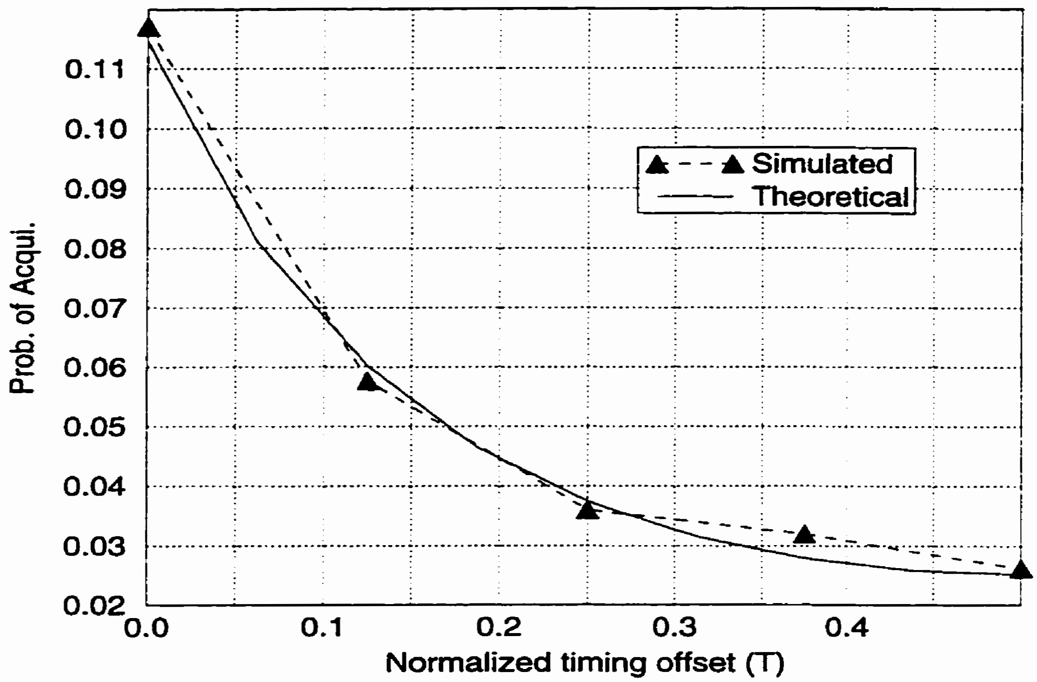

Figure 4.16: Probability of making Correct Estimate (N=1000)

using Eqn. (4.27) to map timing offset to an error probability. Then through use of Eqn. (4.45) to get the plot in Fig. 4.15.

An increase in the CRB means that the estimate has a larger variance. The wider spread of estimates leads to a smaller probability that p is correctly estimated. This decrease in correct estimation means a reduced efficiency of the estimation method. This trend of decreasing probability is plotted in Fig. 4.16. Note that this plot is not a true probability but the peak value of a continuous pdf of a binomial random variable. The small value in probability is because the pdf is widely spread. If all values around the mean are integrated over a fixed interval, the probability is larger but the trend remains the same as shown in Fig. 4.16. The theoretical probability in the plot that corresponds to the mean of a probability distribution governed by the binomial law

$$P(k=Np) = \binom{N}{k} p^k(1-p)^{(N-k)}$$

is also given in the plot. The conditions used for this plot are the same as in Fig. 4.13. The simulated probability follows the trend of the theory. The larger values at some simulation

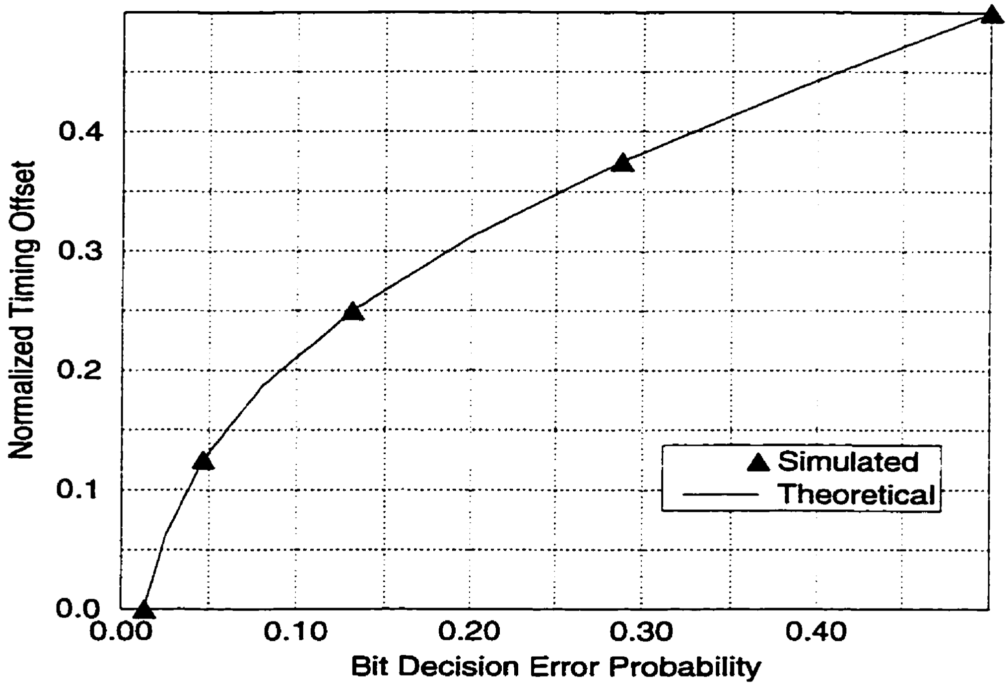

Figure 4.17: Simulated Timing vs. Average Error Probability Curve (SNR = 4 dB)

points in the figure are due to the short probing sequence. Again, the accuracy is sufficient for this study. The timing offset vs. error probability curve is given in Fig. 4.17 for an SNR = 4 dB. Multiple simulations are run with $N = 4000$ in order to get the mean of the timing offset vs. error rate curve. The results match the theoretical ones. This shows that it is possible to establish a relationship between a BER and the timing offset and therefore, the timing error can be estimated from the BER.

Finally, simulation was performed to evaluate the ability of the algorithm to correct a given timing estimate error. This ability is evaluated as a probability of making a correct estimate for a given length of the probing sequence. The probability is obtained by integrating the pdf of the estimated BER ($\hat{p}$) given in (4.56) over a given range around the peak (the mean) of the pdf. The integration range affects the probability value. The range used in this study is the square–root of the CRB of the BER estimate with no timing offset at SNR = 4 dB for a sequence length of $N = 1000$, which gives the equivalent timing offset of about $0.07T$. In equation, the probability is computed as

$$P(\text{acqui}) = \int_{-u_{\alpha/2}}^{u_{\alpha/2}} f(x)\,dx \tag{4.66}$$

where $u_{\frac{\alpha}{2}}$ is the value computed from (4.60) and $f(x)$ is defined by (4.59). The result shows that with 1000 symbols transmitted at $E_b/N_0 = 4$ dB, timing error can be estimated in one step with a probability of 0.5 using the integration range described above for a timing offset of $T/16$. A longer probing sequence improves this probability.

The drawback of this EPM is that a relatively long probing sequence is required, especially for higher operating SNR as will be shown in section 5.1.3, in order to get the estimate of the link error probability. For example, to reach a high probability of 0.95 of correctly estimated BER at SNR $= 4$ dB, for an integration range of $p \pm 0.25p_0$, 4000 symbols are required. The p_0 used here is the error rate of the zero timing offset. p is p_0 when timing offset is zero, otherwise, the p can be computed from (4.27) with a given λ. Also as indicated before, using a 1000 symbol sequence, this method can only yields a correct estimation with probability of 0.5. Since the transform from p to time is non–linear as noticed in (4.55) the estimation efficiency might be reduced as shown in Appendix B. System level simulations which involve both uplink and downlink are not going to be performed using this method.

In the next chapter, a more efficient estimate method based on processing the on–board processor output amplitude, which is named detected signal amplitude method (DSAM), will be introduced. The EPM can be considered as the specific case of the DSAM, where the amplitude is quantized to 0 and 1 by hard decision. The method introduced in the next chapter, on the other hand, can be regarded as making soft decision on the uplink signal amplitude. The system level simulation will be conducted using the DSAM after the performance of the DSAM is studied in the next chapter.

Chapter 5

Delay Estimate (2)

In this chapter, a problem associated with using the EPM is discussed. An alternative estimation method, which is derived from the EPM but with improved performance in terms of estimation time, is introduced. The structure of the estimator, which is based on the principle of the MLE, is given in this chapter. The delay estimation algorithm described is embedded into a complete system simulation model in the next chapter.

5.1 Signal Magnitude as an Error Indicator

5.1.1 From BER to Signal Power

From the user's point of view, the BER is a good indicator of system performance. But as shown in the last chapter, to obtain an acceptable BER requires a long probing sequence. As the SNR increases, this probing sequence becomes longer and longer in order to maintain the accuracy of the BER estimate. This fact follows as the BER decreases with increasing SNR. It becomes impractical to use the BER as the indicator to estimate the delay offset when the BER is small enough for acceptable communications quality. Therefore, though it is possible to estimate the uplink propagation delay from an error probability associated with a BSC channel model using the MLE principle, this is not an efficient approach. The overhead for delay estimation to the system is large if the BER is used for delay estimation error measurement. By examining Equation (4.27), it is found that the BER is related to the timing offset through the power of the sample at the satellite symbol detector. In other words, the detected sample power, or the sample used for detection also provides a measurement of the delay estimation error. Therefore, if the detected signal amplitude is estimated, the timing offset, which can be converted to the propagation delay information, can be calculated from Equation (4.26).

In the following analysis, the satellite deals with the detection of the signal amplitude (voltage) only and the amount of the timing adjustment is computed by the ground terminal. The detected voltage information is transmitted to the ground terminal through the satellite TDM downlink. This information is transmitted in a digitized form and thus the amplitude estimate in the satellite must be quantized before downlink transmission.

To reveal the key characters related to the synchronization problem, Equation (4.26) is rearranged. The signal amplitude is normalized by $A_k T$ and the phase information is removed from the equation on purpose since only the signal amplitude is of interest in the analysis. This normalized signal amplitude is denoted by a in Equation (5.1). This equation does not include any noise signal and is given by

$$a = (1 - 2|\lambda|) \tag{5.1}$$

where λ is the normalized timing offset as defined just after Equation (4.27). Now the timing offset is directly related to the detected signal amplitude. If the signal amplitude can be estimated, the estimated timing offset can be computed. The detected signal amplitude is noise corrupted in a practical system and the voltage must be picked up from a detection sample given in the form

$$x = a + n \tag{5.2}$$

where n is the sample value of the additive noise and x is the sample value of the received signal at the output of the SAW processor. The goal is to find a from x and this goal is achieved by using MLE theory. The MLE of a in (5.2) is used to obtain the delay estimation because the signal amplitude can be treated as an unknown but non–random value. In the next section, the performance of the amplitude estimation technique is analyzed.

5.1.2 Amplitude Estimate

There are two options to obtain the amplitude estimate. One is to transmit each detected signal to the ground terminal directly and the ground terminal processes this information to find the timing offset on the uplink. The other choice is to process a number of detected signal amplitudes on–board the satellite and then send an averaged estimate to the ground terminal. Each method has advantages and disadvantages. These advantages and disadvantages are discussed in the following sections and the one with more advantages is chosen for further study. Since the downlink is a digital channel, the amplitude information (plus the noise on the uplink) must be quantized in order to fit into the TDM downlink channel transmission method. The discussion starts from the method that transmits the detected signal amplitude directly followed by a method which requires more on-board processing but less downlink bandwidth.

5.1.2.1 Quantized Amplitude Estimate

Hereafter this method will be quoted as USQE, which stands for Uplink Signal Quantized and Estimated. This method requires the minimum processing power from the satellite. The signal obtained from the on–board processor is quantized, encoded and transmitted to the ground terminal. The ground terminal looks for uplink timing offset information from the digital information received from the TDM satellite downlink.

The number of bits that are need to be transmitted on the downlink is larger than in the uplink with this method because each detected signal amplitude corresponds to one uplink bit. This amplitude is quantized and encoded by more than one binary digit since, if only one–bit quantization is used, the amplitude information becomes the bit decision, which reduces to the method considered in Chapter 4. It is obvious that the satellite is required to provide high quality signal amplitude information in order for the ground terminal to get an accurate estimate of the timing offset. More precise representation of the detected signal level in a digital form requires more quantization levels, which in turn puts more burden to the satellite downlink. For instance, if N symbols are transmitted from ground terminal to the satellite for the purpose of estimating the uplink propagation delay, these N symbols are detected on–board the satellite and the detected amplitude, instead of being interpreted to 0 and 1, is quantized to discrete levels. These levels are then represented by binary codes. The length of this binary code determines the possible number of quantization levels. If 6 bits are used to encode the signal levels, then a total of $N \times 6$ bits are going to be transmitted in the downlink in order to estimate the uplink delay. Therefore, this method requires more system bandwidth resource on the downlink to obtain the uplink propagation delay estimate. The method considered here also suffers larger distortion in general because it estimates the delay from a quantized version of the detected signal amplitude. The discrete noise signals do not follow the Gaussian distribution exactly. Therefore, the delay estimate from these discrete signals is not an exact maximum likelihood estimate when only simple averaging is used.

In the next subsection, another timing offset estimate method, which is also based on the detected signal amplitude but with a different approach to obtain the amplitude estimate is introduced. The performance of these two approaches is compared after this estimate method is described.

5.1.2.2 Revised Quantized Amplitude Estimate

In the last subsection, the USQE method was introduced. The problem of using too much system capacity with this method was also indicated. If the satellite can process the detected uplink signal amplitude, this problem can be alleviated. Such a method will be called USEQ, which stands for Uplink Signal Estimated and Quantized. Instead of transmitting all the N detected signal amplitudes on the downlink, the satellite first estimates the signal amplitude on–board, then sends an averaged result to the ground terminal. The ground terminal takes the estimated result and compensates for the timing offset by adjusting the uplink timing phase. The USEQ takes only b bits of the satellite downlink bandwidth to transmit the delay information, where b is the code length used to encode the estimates. This means less demand on system capacity because only one result is transmitted for an N bit probing sequence.

The estimation processes of the USQE and the USEQ are listed in Table 5.1. It is clear that the USQE requires less processing on–board. The USEQ method needs more processing power from the satellite but requires no additional hardware for the ground terminals. Since the philosophy here is to let the ground terminals share the system resource as much as possible, the USEQ is preferred to the USQE as the on–board processor is shared by all the terminals. With a less signal processing requirement, the ground terminals become simpler as well.

USQE	USEQ
1. quantization/encode (on–board)	estimate (on–board)
2. decode (ground)	quantize/encode estimate (on–board)
3. estimate from decode (ground)	decode (ground)

Table 5.1: Two approaches to get Delay Estimate from Uplink Signal Amplitudes

In the following discussion, when citing *"the timing is derived from detected signal* *amplitude*", this refers to the use of the USEQ method.

5.1.2.3 Estimation of Amplitude

Since n is a Gaussian random variablewith zero mean and a is a constant as defined in Equation (5.2), x is a Gaussian random variableand a is the mean of x. Therefore, to find a is to estimate the mean of random variable$x$. The random variable x follows the normal distribution

$$f_X(x) = \frac{1}{\sqrt{2\pi}\sigma_x} \exp(-\frac{(x-a)^2}{2\sigma_x^2}) \tag{5.3}$$

where σ_x^2 is the variance of the random variable$x$. The likelihood function is obtained by taking N samples from the sample space, $\mathbf{X}$. Elements in $\mathbf{x} = [x_1, x_2, \cdots, x_N]$ are *iid* and therefore the likelihood function is

$$p_{\mathbf{X}|A}(\mathbf{x}|a) = \prod_{i=1}^{N} \frac{1}{\sqrt{2\pi}\sigma_x} \exp(-\frac{(x_i-a)^2}{2\sigma_x^2}). \tag{5.4}$$

Use of the MLE principle gives the estimated signal amplitude, denoted by $\widehat{a}$, as an average of these samples of the detected signal determined by [41],

$$\widehat{a} = \frac{1}{N}\sum_{i=1}^{N} x_i. \tag{5.5}$$

This estimate itself is a Gaussian random variablebecause it is a linear combination of the Gaussian random variables, x_i. The estimate is unbiased because

$$E[x_i] = a \tag{5.6}$$

which follows from the calculation,

$$\begin{aligned} E[\widehat{a}] &= E[\frac{1}{N}\sum_{i=1}^{N} x_i] \\ &= \frac{1}{N}\sum_{i=1}^{N} E[x_i] \\ &= \frac{Na}{N} = a. \end{aligned} \tag{5.7}$$

It is possible to show that the estimate is efficient [41]. It can be shown that the CRB, which was introduced in subsection 4.2.3, of $\widehat{a}$ is

$$\sigma_{\hat{a}}^2 = E[(\widehat{a} - \overline{\widehat{a}})^2] = \frac{\sigma_x^2}{N}. \tag{5.8}$$

The estimate, $\hat{a}$, can be written as

$$v = a + z = \widehat{a} \tag{5.9}$$

where z represents the random part of the estimate. Therefore, z is a zero mean Gaussian random variablewith variance $\sigma_z^2 = \sigma_x^2/N$. It is considered as a noise signal with less power compared to the noise at the input to the estimator. Such a noise signal is superimposed onto the un–distorted signal with voltage amplitude a as shown in (5.9) and hence the signal to be transmitted to the ground is the sum of the true signal amplitude plus a residual noise from the estimation process. Therefore, this signal processing improves the effective SNR when the signal amplitude estimate is made. The improvement of the effective SNR is a function of the length of the sequence used to obtain the estimate. The noise reduction in terms of signal power is given by Equation (5.8). The amount of SNR improvement is derived as follows. With the SNR defined as

$$\text{SNR} = \frac{A^2}{2\sigma_x^2} = \frac{E_b}{N_0} \tag{5.10}$$

and using Equation (5.8), the effective SNR, denoted by SNRE, is

$$\text{SNRE} = \frac{A^2}{2\sigma_z^2} = \frac{A^2 N}{2\sigma_x^2}. \tag{5.11}$$

When expressed in the form of a decibel, the SNR becomes

$$\text{SNRE(dB)} = \text{SNR(dB)} + 10\log N. \tag{5.12}$$

For $N = 100$, the gain is 20 dB.

Future discussion in this subsection will deal with a Gaussian random variablewith mean a and variance σ_z^2. The pdf of such a random variableis plotted in Fig. 5.1. In the

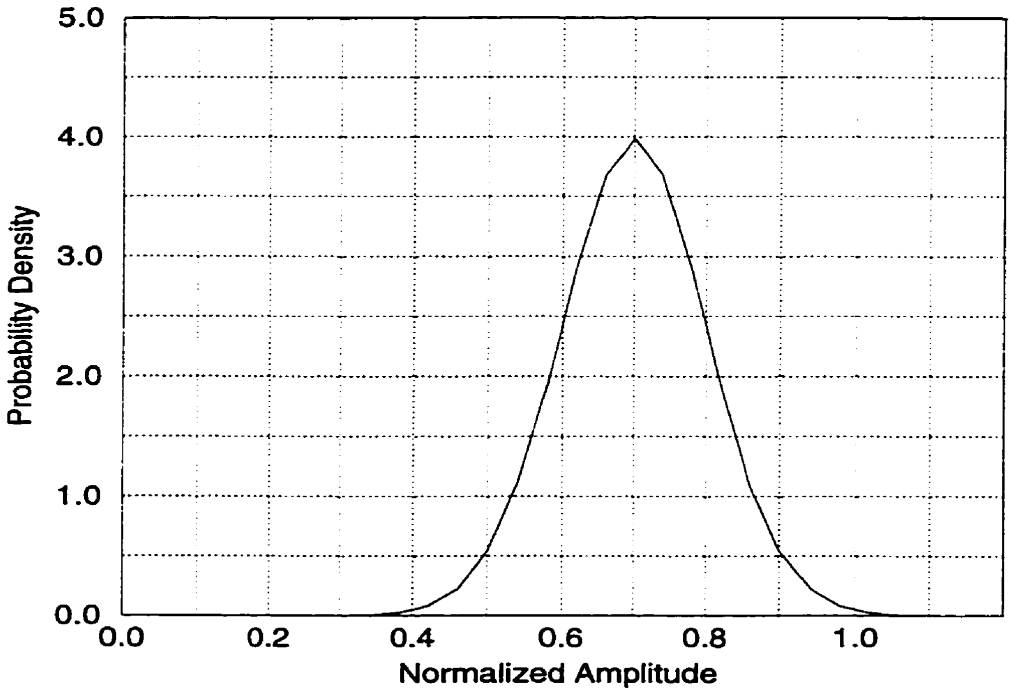

Figure 5.1: Probability Distribution of Estimated Signal Level

figure, the signal level a is assumed between 0 and 1. $\sigma_z = 0.1$ is used for the plot. This corresponds to the case that SNR = 17 dB, where SNR is defined as E_b/N_0 as before in (4.32), if the normalized signal amplitude is set to one. Such an SNR is obtained through the processing of the detected signal using Equation (5.8). The real operating SNR is -3 dB for this example. The amplitude range is deliberately plotted to exceed one in order to show the possible distortion when the normalized signal amplitude is restricted to between 0 to 1. Those signals of larger than 1 and less than 0 are going to be rounded to 1 or 0 respectively depending on the signal amplitudes.

The number of samples needed for a given acquisition probability can be determined because the estimate follows the Gaussian probability distribution. From (5.9), if quantization is not considered, the remaining amplitude error after correction will be a Gaussian random variable z with zero mean and variance σ_z. For a sampling frequency of 8 samples per symbol, the maximum quantization error is $A/16$ where A is the maximum signal amplitude. Synchronization lock is declared when the error is less than the maximum quantization error, $A/16$. Therefore the acquisition probability can be written as

$$P(\text{Acquire}) = P(|z| \leq A/16) \tag{5.13}$$

In other words, the probability of no acquisition is

$$P(\text{No Acqui.}) = P(|z| > A/16) \tag{5.14}$$

Use of the complementary error function defined in [38], the above equation becomes

$$P(\text{No Acqui.}) = 2Q\Big(\frac{A}{16\sigma_z}\Big) \tag{5.15}$$

where $\sigma_z^2 = \sigma_x^2/N$ as defined before. Use of the definition of SNR given in (4.32), equation (5.15) becomes

$$\begin{aligned} P(\text{No Acqui.}) &= 2Q\Big(\sqrt{\frac{A^2}{16^2 \times \sigma_x^2/N}}\Big) \\ &= 2Q\Big(\sqrt{\frac{2 \times N \times \text{SNR}}{16^2}}\Big). \end{aligned} \tag{5.16}$$

If the required probability of acquisition is 0.9999, that is the probability of no–acquisition is 10^{-4}, then

$$\frac{2 \times N \times \text{SNR}}{16^2} = 7.5 \tag{5.17}$$

and with the operating SNR 10 dB

$$N = \frac{7.5 \times 16^2}{10 \times 2} = 96. \tag{5.18}$$

Therefore, if the operating SNR is 10 dB, $N \approx 100$ is needed for the estimator to give a proper amplitude estimation with probability of 0.9999. It is worthwhile to indicate that the estimated parameter is signal amplitudes here, a relatively short estimating sequence is required in order to reach a high acquisition probability. For instance, for the EPM discussed in Chapter 4, where the estimated parameter is the BER, a much longer estimating sequence, $N > 1000$, is required even for a lower acquisition probability of 0.5.

The above discussion assumes the estimate is used to correct the timing error without any distortion. Under such an assumption, a zero mean Gaussian probability distribution with variance σ_z is obtained from the estimate. The estimated signal amplitude is going to be transmitted to the ground terminal through the satellite's downlink digital channel, the signal must be quantized and digitally encoded since digital implementation is considered in this thesis. The number of quantization levels required depends on the requirement of accuracy. An arbitrary signal amplitude a is used to show the peak point of the pdf in Fig. 5.1. The acquisition probability with quantization distortion is studied below.

From (5.9), the amplitude estimate is obtained. The quantized estimate, v_q, has a discrete probability distribution over all possible quantization levels. Assume b bits are used to represent one quantization level when there are $M = 2^b$ signal levels. Let l_k be the k-th quantization level ($k = 1, 2, \cdots, M$). The probability that the signal is quantized to l_k is

$$\begin{aligned} p(l_k) &= P(l_k - q \leq v < l_k + q) \\ &= P(l_{k-1} + q \leq v < l_k + q). \end{aligned} \tag{5.19}$$

In equation (5.19) q is the maximum quantization distortion. Assume the signal to be quantized is between 0 and A ($A = 1$ in Fig. 5.1) where q is defined as

$$q = \frac{A}{2M} \tag{5.20}$$

and M is as defined as before. The q quantization levels fall on the following values

$$l_k = (2k-1) \times q \qquad k = 1, 2, \cdots, M. \tag{5.21}$$

Now let $l_k = a_q$ be the nearest quantization level to a, the mean of the estimate in (5.9), and $Q_u(\cdot)$ be a quantization function as

$$Q_u(\widehat{a}) = a_q \qquad a_q - q \leq \widehat{a} < a_q + q \tag{5.22}$$

where q is the maximum quantization error. Then the probability of acquisition becomes

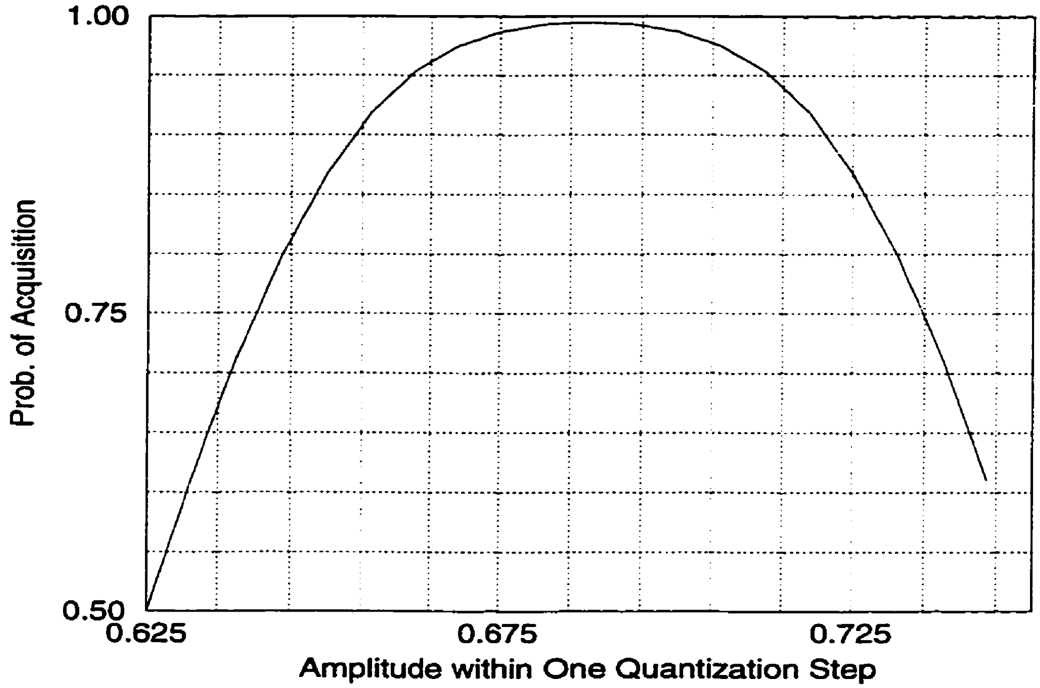

Figure 5.2: Probability of Acquisition with Different Signal Amplitude

$$P(\text{Acquire}) = P(Q_u(\hat{a}) = a_q) = \int_{a_q-q}^{a_q+q} f(x)dx \qquad (5.23)$$

where $f(x)$ follows Gaussian distribution with mean a and variance σ_z^2. If $a = a_q$, (5.23) is equivalent to (5.13). Generally speaking $a \neq a_q$ and then the probability of no acquisition is given by

$$P(\text{No Acqui}) = Q(\frac{|a - a_q - q|}{\sigma_z}) + Q(\frac{|a - a_q + q|}{\sigma_z}) \qquad (5.24)$$

if the only distortion is due to quantization. Therefore, the probability of acquisition is smaller than the result from (5.13). For the worst case, the timing offset is right at the center of two quantization levels. Then the probability of acquiring the correct timing is, under the best circumstances, 0.5. The acquisition probability versus true signal amplitude is given in Fig. 5.2. The estimation length is 100, number of samples per symbol is 8, and the operating SNR is 10 dB in this plot.

When the timing offset is very large ($\tau = T/2$) or very small ($\tau = 0$), quantization of the estimated signal amplitude results in overload distortion due to confined usable signal range. With $\tau = T/2$, using (5.5), one get an estimate $\widehat{a}$ with a zero mean Gaussian distribution. This signal will be quantized to the lowest level l_0 with probability

$$P(Q_u(\widehat{a}) = l_0) = \int_{-\infty}^{l_0+q} f(x)dx. \tag{5.25}$$

This probability is larger than

$$P(Q_u(\widehat{a}) = l_0) = \int_{l_0-q}^{l_0+q} f(x)dx. \tag{5.26}$$

The effect of overload distortion is further illustrated later with figures.

Now the discussion is moved to the initiative of this study, the timing offset estimate. Because each quantization level corresponds to a timing offset from the signal amplitude vs. timing offset relationship given in Equation (5.1) for a given SNR_0 (or A) with a properly selected probing sequence, the probability for each quantization level is also the probability that the estimated timing offset is T_k. From above discussion, it is clear that if the distortion from quantization and overload is not considered, the probability of acquiring timing is independent of the amount of timing offset. When quantization and overload are included, the probability of acquiring timing becomes dependent of the amount of timing offset. Then (5.24) and (5.25) are more suitable representation of the true situation. Therefore the study will be concentrated on the discrete probability distribution $p(l_k)$ which serves following two purposes:

1. To find the average time delay estimate, which is defined as the mean of all the possible estimates,

$$\overline{T}_e = \sum_k T_e(k)p(l_k). \tag{5.27}$$

2. To provide the probability of a specific signal being quantized to the correct level. That is, the signal $v = a + z$ is quantized to the level corresponding to a.

SNR (dB)	Sequence Length	Max. Ampl.	Real Ampl.
5	100	1.	0.7

Table 5.2: Parameters used in Fig. 5.3

In the rest of this subsection, the effect of quantization and overload due to the signal exceeding the quantization range is studied in detail by using a 4–bit/16–level quantization system to process the estimated signal amplitude. The typical pdf of a quantized signal amplitude is plotted in Fig. 5.3. The original continuous probability distribution was given in Fig. 5.1. The peak probability in the figure is 0.518. The parameters used in this plot are given in Table 5.2. The sequence length is the number of symbols used to perform the estimation. The real amplitude in the table is less than the maximum due to the timing offset and the additive noise.

Pdfs with the same timing offset but different SNRs are plotted in Fig. 5.4 for various noise levels (SNRs). The pdf becomes more condensed to its mean as the SNR increases. The trend shows the improvement of the estimation process because the chance of making a correct estimate increases as the SNR increases. At lower SNR, the uncertainty of the estimate is large because of the wider distribution of the possible estimates.

Different signal amplitudes within one quantization step are the result of different timing offsets and lead to slightly different shapes for the pdfs. In Fig. 5.5, when $a = l_i$ ($a = 0.71875$ in the figure falls right on one of the quantization levels), there is no quantization distortion for this level and the pdf is symmetrical about a. Usually, $a \neq l_k \quad (k = 1, 2, \cdots, M)$ and the discrete pdf is skewed. The peak of the pdf is close to the true value which is going to be estimated. When $a = l_i + q$, it is quantized to level l_i and l_{i+1} with equal probability. Therefore, the resulting pdf is symmetrical relative to $l_i + q$ as shown in Fig. 5.6.

It is also observed that at the end points, the probability distribution is highly skewed

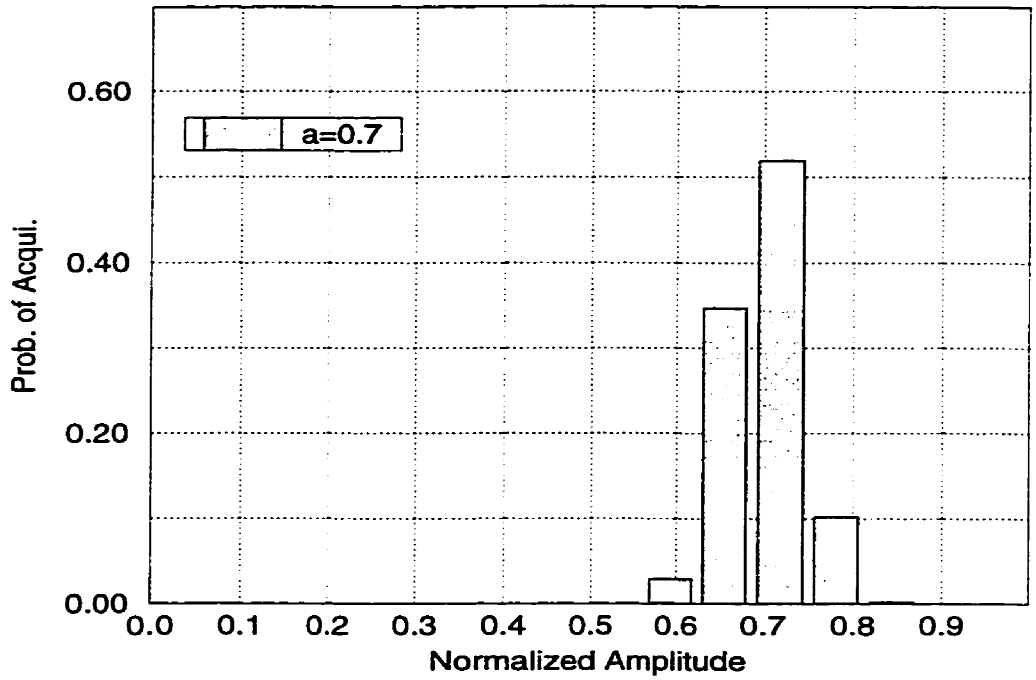

Figure 5.3: PDF of a Quantized Signal

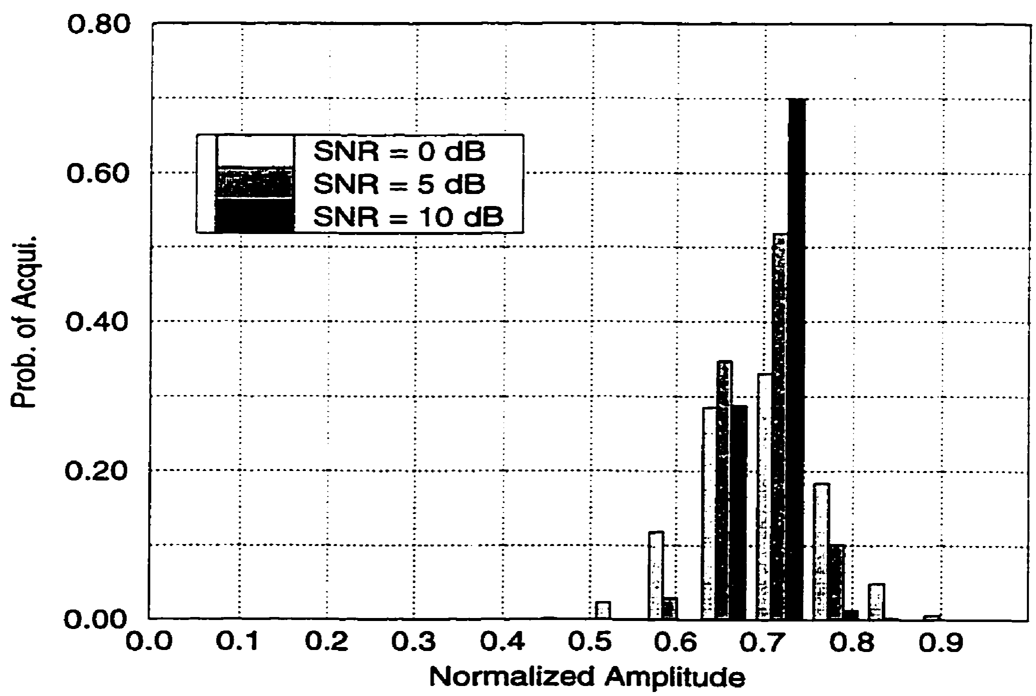

Figure 5.4: PDF of Quantized Signals for Various Noise Levels

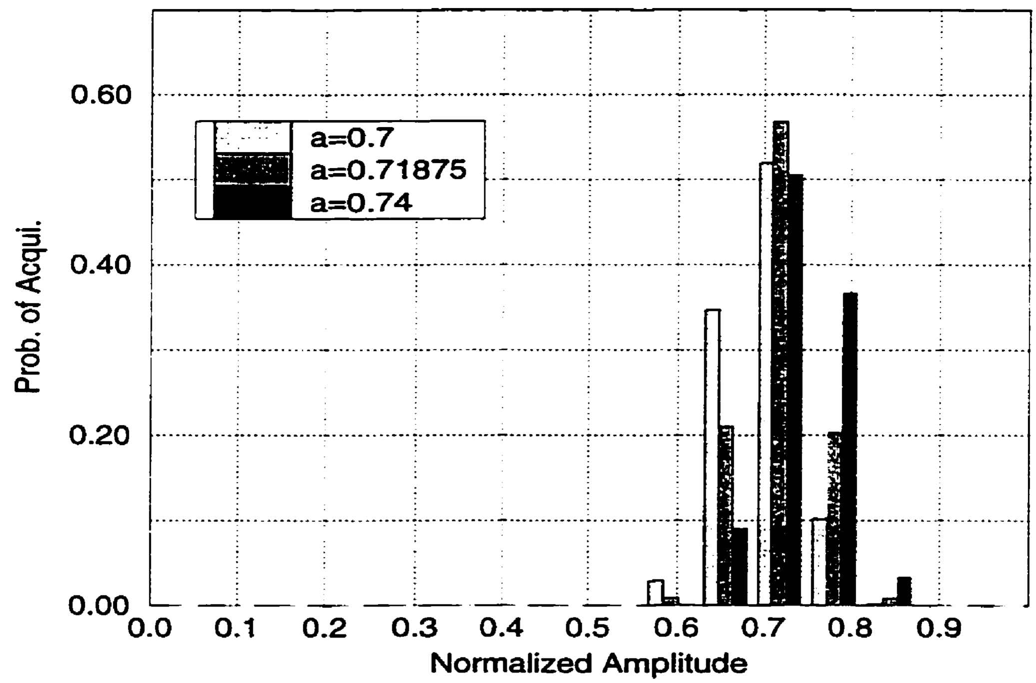

Figure 5.5: PDF of Various a within one Quantization Step

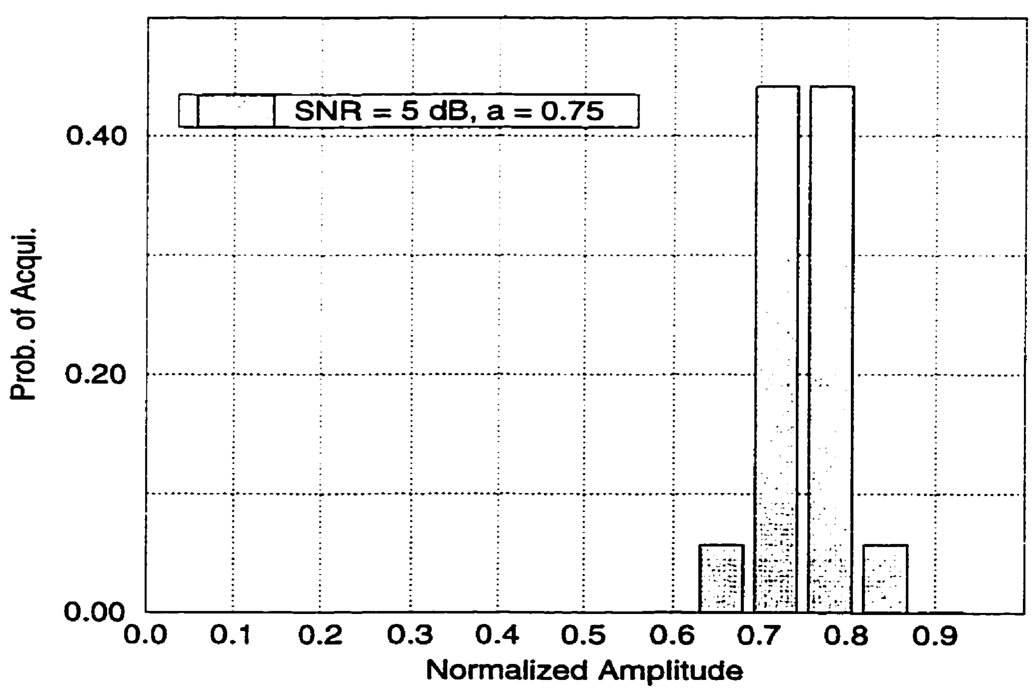

Figure 5.6: PDF of Quantized Signal when $a = l_i + q$

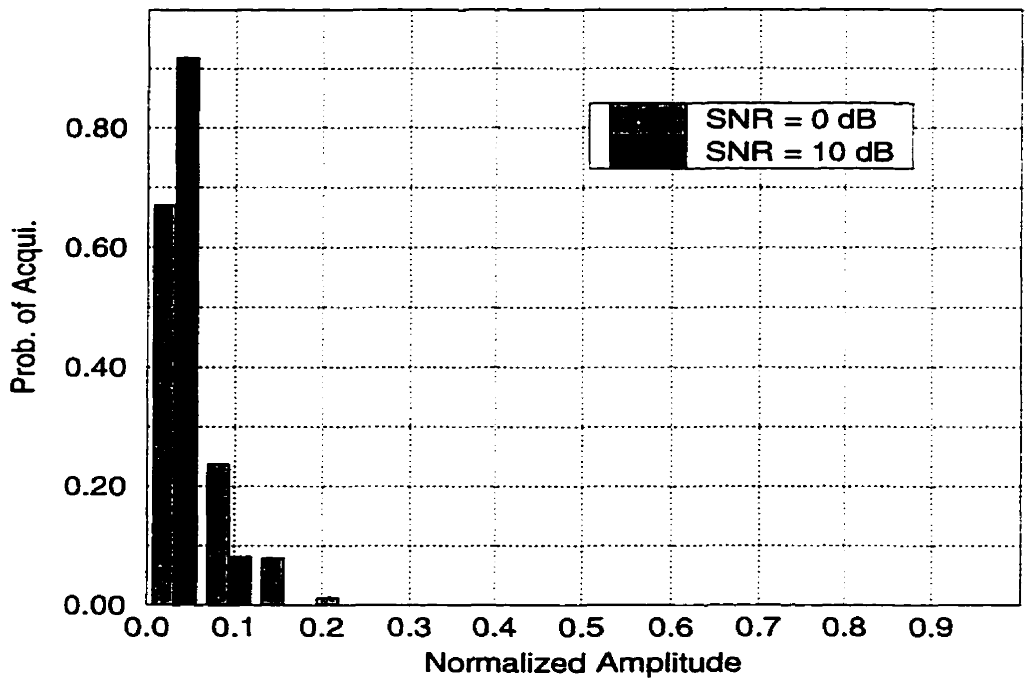

Figure 5.7: PDF when a is at the lowest Quantization Level

because of the overload distortion in the quantization process. The overload distortion increases the probability of the signal being quantized to the correct level since the overloaded signals are quantized to the first available quantization level, which, in this case, happens to be the desired one. The situation for a close to zero is plotted in Fig. 5.7. In this figure, the signal level equals the lowest quantization level but the plot is not symmetrical as in the previous discussion. Furthermore, the end point gives an increased probability of the correct estimation. This is shown in Fig. 5.8. In this figure, $a = 0.01$, which is lower than the smallest quantization level. This overload effect diminishes as a moves to the center, *i.e.* $a \approx A/2$, or when the SNR is large. In the later case, the overload distortion is small because the estimate has a smaller variance.

The number of quantization levels also has an effect on the estimation process. This is examined next. When the number of quantization levels increases, the probability for one specific level usually decreases as compared to a case which has less quantization levels. A larger number of levels provides a better time resolution. Therefore, a trade–off must be made between the consistency (higher probability) and the accuracy (finer resolution).

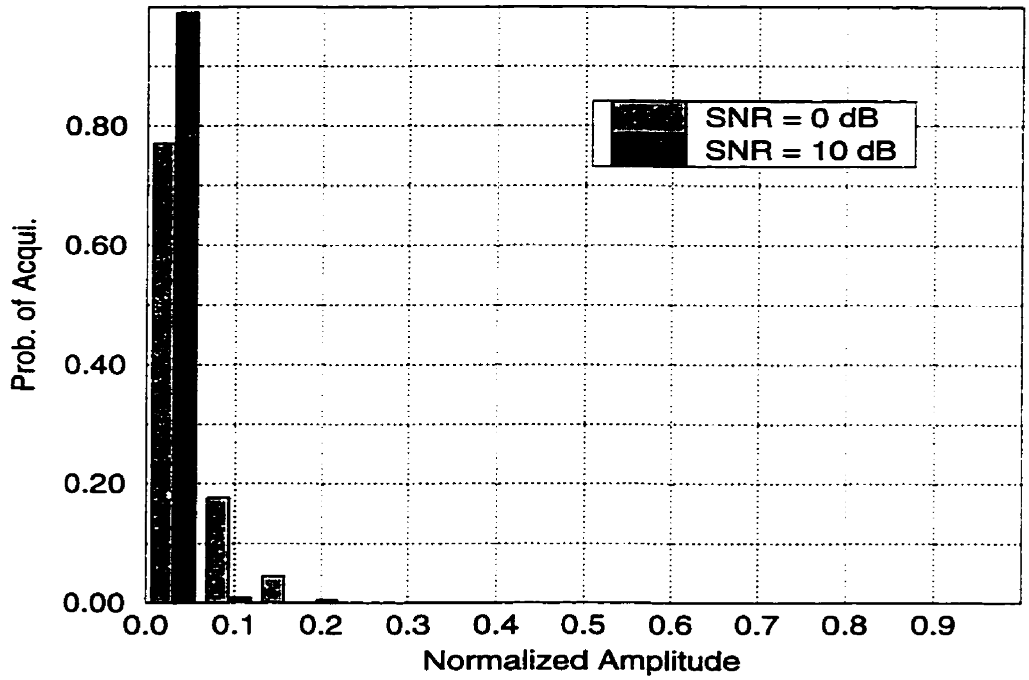

Figure 5.8: PDF when a is less than the lowest Quantization Level

The pdf for 64–level quantization is given in Fig. 5.9. In the figure, two different SNRs (10 dB and 0 dB) are used. Again, an improved estimate is noticed as the result of higher SNR. The pdf of the 64–level quantizer is compared with the 16–level one in Fig. 5.10 for SNR = 0 dB. A more gradual change is obvious for 64–level quantization. It is also true that the probability that the estimate falls into the closest quantization is smaller for 64–level quantization as indicated previously.

As noted in the beginning of this subsection, an estimate made from a longer sequence increases the effective SNR. This conclusion holds for the quantized case as shown in Fig. 5.11 where different lengths of the estimate sequence are used.

5.1.2.4 Performance of Timing Estimate

The statistical performance of the method of amplitude estimation is studied in this subsection. First, the mean of the time delay estimate is evaluated. Let T_e be the timing offset that corresponds to a and $T_e(k)$ the timing offset derived from level l_k in the quantization process, as defined in equation (5.21). The residual timing offset after a correction based

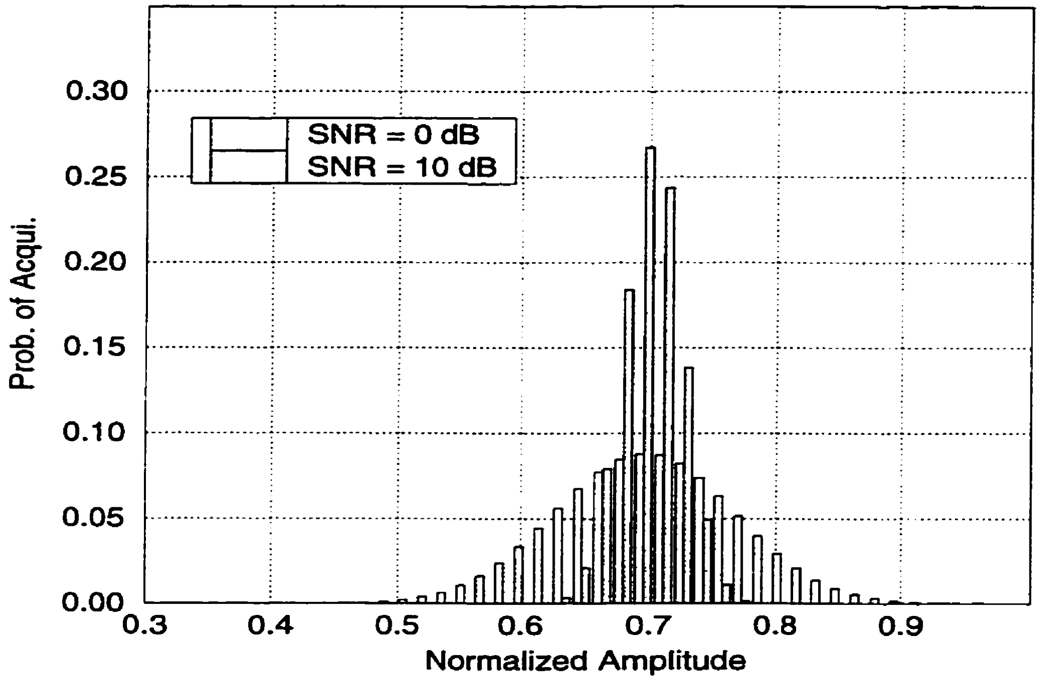

Figure 5.9: PDF of 64–level Quantization

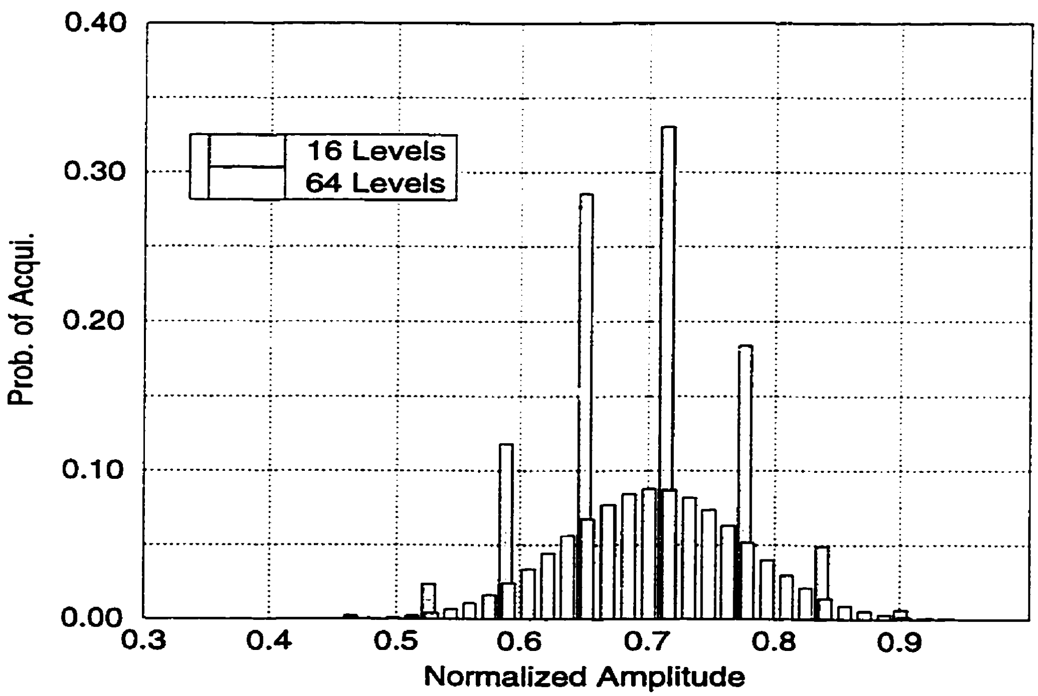

Figure 5.10: Comparison of 64–level and 16–level Quantization

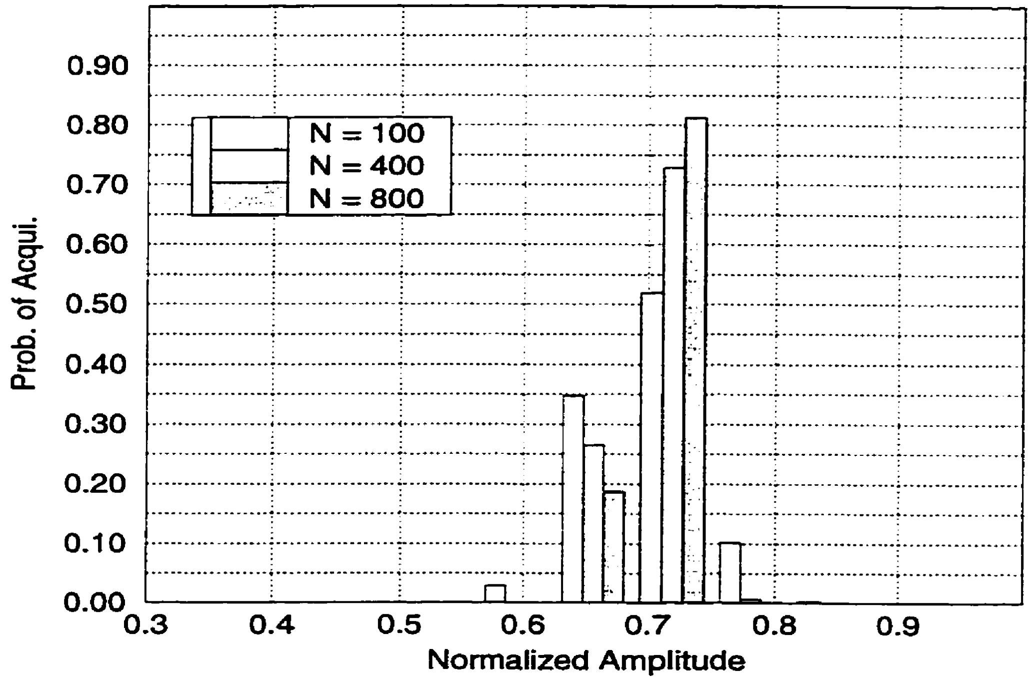

Figure 5.11: Longer sequence improves Estimation

on $T_e(k)$ is defined as

$$T_r(k) = T_e - T_e(k). \tag{5.28}$$

If $T_e(k) = T_e$, the estimate matches the true value and the residual is zero. Since $T_e(k)$ is a random variable with the same pdf of l_k, the average residual timing offset is obtained from averaging the residual offset by its pdf using (5.27) to give

$$\overline{T}_r = \sum_k T_r(k)p(l_k) = T_e - \sum_k T_e(k)p(l_k) = T_e - \overline{T}_e. \tag{5.29}$$

The second term at the right hand side of the equation is the averaged estimate of the timing offset. When $a = l_i$, the signal amplitude is one of the quantization levels, $T_e(k)|_{k=i} = T_e$, the pdf of $T_e(k)$ is symmetrical to l_i. Therefore

$$p(l_{i+j}) = p(l_{i-j}) \qquad i+j \leq M \quad \text{and} \quad i > j \tag{5.30}$$

and

$$\overline{T}_e = \sum_k T_e(k)p(l_k) = T_e \tag{5.31}$$

which gives

$$\overline{T}_r = \sum_k T_r(k)p(l_k) = 0. \tag{5.32}$$

If $a \neq l_i$

$$\sum_k T_e(k)p(l_k) \neq T_e \tag{5.33}$$

because the pdf is non–symmetrical relative to T_e. Therefore

$$\overline{T}_r \neq 0. \tag{5.34}$$

This conclusion is further justified as follows. When there is no noise, the signal will be quantized to one specific level with probability 1. If the signal level does not match a specific quantization level exactly, there is a very small residual error. The amplitude of this error depends on the true signal level but will not be larger than q, the maximum quantization distortion. Since the noise is zero mean, if the quantization causes an error, one can expect the mean timing estimate error is zero. Otherwise, the residual error has a non zero mean. When $T_r \neq 0$, the estimate is biased. Because the amount of the bias is within the maximum quantization distortion, the estimate is considered as unbiased in the following discussion. The two sets of numerical results given in Table 5.3 and Table 5.4 are used to justify the above conclusion. Table 5.3 shows the case of $\overline{T}_e \neq T_e$. For lower SNR, since the environmental noise is more dominant than the quantization noise, the mean timing error is close to its true value. On the other hand, as SNR increases, the quantization distortion becomes dominant and the estimate has a clear bias. In the calculation, $n = 4$ bits is used to represent 16 quantization levels and the signal amplitude A is normalized to 1. The detected signal amplitude a is set to 0.7 and 0.71875 to represent $a \neq l_i$ and $a = l_i$ (at the quantization level) cases, respectively. In these two tables, column 2 is the normalized average estimate of the timing offset and column 3 is the probabilities of the signal being quantized to level $T_i = 0.1406$, which is the closest quantization level to the true signal amplitude. The amount of the timing offset is given in the respective captions.

In Table 5.3, $\overline{T}_e \neq T_e$ for SNR $\neq 0$ dB. As indicated before, when noise is not included, the signal is quantized to a specific level with probability one. The estimates in this table are biased. The amount of bias depends on the true value of the signal amplitude and the maximum is q for the amplitude estimate, where q is one half of the quantization level. In Table 5.4, the averaged estimate is always the true value because this true timing offset is one of the quantization levels. From these tables, it is found that the estimate method is consistent when SNR ≥ 10 dB.

SNR	$\overline{T}_e/T$	Prob($T_i = 0.1406$)
0	0.15	0.33
5	0.14997	0.52
10	0.1492	0.7
15	0.1456	0.84
∞	0.1406	1

Table 5.3: Average Timing Offset Estimate for $T_e = 0.15T$

Next, the probability of the signal being quantized to the level, to which a noiseless signal would be quantized, is studied. Assume $v = (a + z_n)$ is quantized to level l_i with probability $p(l_i)$. The probability is the sum of a continuous pdf for all the signals within the interval $[l_i - q, l_i + q]$. Such a probability can be obtained from the pdf for this sum. The amplitude interval is used to determine the interval of the timing offset estimate with

SNR	$\overline{T}_e/T$	Prob($T_i = 0.1406$)
0	0.1406	0.34
10	0.1406	0.84
∞	0.1406	1

Table 5.4: Average Timing Offset Estimate for $T_e = 0.1406T$

the help of Equation (5.1). The corresponding time interval is $[t_{lo}, t_{up}]$. The upper and the lower points t_{up} and t_{lo} are given by

$$\begin{aligned} t_{up} &= \frac{(1-\frac{l_i-q}{A})T}{2} \\ t_{lo} &= \frac{(1-\frac{l_i+q}{A})T}{2}. \end{aligned} \tag{5.35}$$

For different levels of noise, the probability $p(l_i)$ is different, but the interval is fixed as shown in Fig. 5.4. It is worthwhile to note that for the different signal amplitudes, a, the level it is quantized to is different. In the next section, the performance of this estimation method is compared with the estimation method using BER as an offset indicator (EPM) described in section 4.3 and 4.4 for a given a and fixed noise signal power.

5.1.3 Comparison with Error Probability Method

Two delay estimation methods: using BER as the error measurement, named EPM in Chapter 4, and using the detected signal amplitude as the error measurement, named DSAM, which was discussed in the previous sections of this chapter, are compared herein for estimation accuracy and the average residual error. The operating SNR and probing sequence length are specified in the discussion.

With the operating SNR, the probing sequence length and a detected signal amplitude at the output of the processor prescribed, the probability that the signal amplitude is estimated correctly can be computed using the DSAM. The estimation accuracy is defined in terms of the probability of making a correct estimate for the range of signals being considered to obtain such a probability. With this probability determined, the EPM needs further calculation to obtain the range of the bit error probability estimates from where the specific probability is achieved.

The procedures noted above are illustrated in this section. Numerical results will be given. The pdf calculated in the last section provides the probability that an estimate falls in a range of $[l_i - q, l_i + q]$ for a given signal amplitude a, operating SNR, and the number of quantization levels. The signal amplitude and timing offset are related by

$$t = \frac{(1-a)T}{2}. \tag{5.36}$$

Equation (5.36) is the inverse function of Equation (5.1), in which $\lambda = t/T$. Therefore, once the signal amplitude is estimated, giving $\hat{a}$, the timing offset estimate can be readily computed from (5.36). The DSAM gives the probability of the signal levels falling within one specific quantization range. Therefore, the estimate of the timing falls in a range governed by (5.35). As an example, assume the timing offset $T_e = 0.15T$. Then $\lambda = T_e/T = 0.15$ and from (5.1) the detected signal amplitude is $a = 0.7A$. Such an a is quantized to $l_i = 0.71875$ using a 4–bit/16–level quantizer which is needed for downlink digital transmission, which in turn gives a timing offset estimate of 0.140625 if the decision is correct. The true value is 0.15. The associated maximum quantization distortion determines the range of the estimate using (5.35). This range is [0.125, 0.15625].

Now, consider bit error probability method presented in Chapter 4. The bit error probability is also estimated using MLE and the variance of this estimate has a lower bound CRB $= \sigma^2_{\hat{p}}$. The timing interval using the EPM is calculated using the procedure given below.

1. Form a Gaussian random variable$p_n = (\widehat{p} - p)/\sigma_{\hat{p}}$. Where $\widehat{p}$ is the estimate of p, the bit error probability. $\sigma^2_{\hat{p}} = p(1-p)/N =$ CRB. The probability distribution of $\widehat{p}$ is approximately Gaussian when the number used for the estimation is larger than 50 [77]. The random variablep_n has zero mean and variance of 1.

2. For a given bit error probability, the integration interval $[-u_{\alpha/2}, u_{\alpha/2}]$ is obtained by solving the equation

$$p(l_i) = P(|p_n| < u_{\alpha/2}) = \int_{-u_{\alpha/2}}^{u_{\alpha/2}} \frac{1}{\sqrt{2\pi}} \exp(-\frac{x^2}{2})\, dx \tag{5.37}$$

3. $\widehat{p}$ is in a range of $\widehat{p} = p \pm u_{\frac{\alpha}{2}}\sigma_{\widehat{p}}$. Two conditions $p + u_{\frac{\alpha}{2}}\sigma_{\widehat{p}} \leq 0.5$ and $p \geq u_{\frac{\alpha}{2}}\sigma_{\widehat{p}}$ must be met since $0 \leq p \leq 0.5$. Those probabilities that do not meet the two conditions are discarded from the discussion.

4. Step 3 gives the upper and the lower limits of the error probability. The signal levels (the effective SNR) can be found from these error probabilities using

$$\begin{aligned} a_{low} &= Q^{-1}(\widehat{p} + \sigma_{\widehat{p}} u_{\frac{\alpha}{2}})\sigma_x \\ a_{high} &= Q^{-1}(\widehat{p} - \sigma_{\widehat{p}} u_{\frac{\alpha}{2}})\sigma_x \end{aligned} \tag{5.38}$$

   where σ_x^2 is defined as the variance (power) of the noise signal.

5. From the signal levels, the timing offset can be calculated as before using (5.35).

Numerical results for both methods are given in Table 5.5. The ultimate goal of showing these tables is to determine which method is a more suitable one for the delay estimate for the on–board processing satellite system. Table 5.5 (b) is solely used for the EPM. Two probabilities, $P(l_i) = 0.33$ for SNR $= 0$ dB and $P(l_i) = 0.7$ for SNR $= 10$ dB from the DSAM are used with Eqn. (5.37) to compute the $\widehat{p}$ in Table 5.5 (b). The values in the tables are obtained as follows. The SNR is the designed signal–to–noise ratio. a is the measured signal amplitude while assuming signal amplitude is normalized to $A = 1$ when timing is correct. p is the bit error probability corresponding to the signal amplitude a in an AWGN environment, where the noise level is determined by the SNR. The estimation is obtained from a 100-symbol probing sequence. The number of quantization levels are sixteen. The error probability p and the $\sqrt{\text{CRB}}$ are not used by the DSAM in Table 5.5 (a) but are used by the EPM in Table 5.5 (b). The $\widehat{p}$ range is determined using Equation (5.37). The range of the signal amplitude a is then obtained using the equations in (5.38). The criterion of picking up probabilities stated above (Item 3 of timing interval computation procedure on Page 102) is used to discard unsuitable results. These discarded results are listed as *not applicable (N/A)* in the table.

SNR	a	p	$\sqrt{\text{CRB}}$	t (DSAM)
0	0.7	0.161	3.68×10^{-2}	$0.125 - 0.15625$
10	0.7	1.03×10^{-3}	3.21×10^{-3}	$0.125 - 0.15625$

(a)

SNR	$\hat{p}$ (range)	a (range)	t (EPM)
0	$9.5 \times 10^{-3} - 0.313$	$0.6573 - 0.7452$	$0.1274 - 0.1713$
10	not applicable	N/A	N/A

(b)

Table 5.5: Numerical Results for EPM and DSAM

For SNR $= 0$ dB, the estimated timing offset is not as good as using the DSAM with such a short estimating sequence. For SNR $= 10$ dB, the EPM can not be used for a short sequence of 100 symbols but DSAM is useful at this SNR with an even better estimate variance.

Additional tables for the different SNRs are provided in Table 5.6 and Table 5.7 for further comparison of the two methods. The bit error probabilities after the timing is re-aligned according to the correct delay estimate are given under entry p. The two methods are compared for a given SNR with a fixed number of symbols used for the estimation. The averaged bit error probability column $\overline{p}$ is designed to show the average performance difference between the two methods. This average $\overline{p}$ is defined as

$$\overline{p} = \sum_i p_i p(i). \tag{5.39}$$

In (5.39), p_i is the bit error probability when the timing is corrected using the estimate on state i. $p(i)$ is the probability that estimate falls on the state i. This is $p(l_i)$ for the DSAM. For the EPM, the binomial distribution is used. Note here, if p is the designed error probability, the timing offset is assumed zero for those estimate that is less than p using the EPM. It is clear that DSAM has a better average bit error probability performance. The

Method	|max error|(T)	N	p	prob	$\overline{p}$
EPM	0.0213	100	0.07931	0.33	0.1247
DSAM	0.015625	100	0.08261	0.33	0.0921

Table 5.6: Comparison of EPM and DSAM (SNR = 0 dB)

prob entry corresponds to $p(l_i)$, where l_i is the correctly quantized signal level.

Method	|max error|(T)	N	p	prob	$\overline{p}$
EPM	Not Applicable	100	N/A	0.7	N/A
DSAM	0.015625	100	8.25e-6	0.7	1.004e-5

Table 5.7: Comparison of EPM and DSAM (SNR = 10 dB)

Since the bit error probability method has a much fine time resolution with a relatively small probability on each step, to compare the best correction, the EPM is better than DSAM. The DSAM is better than the EPM in the sense of the averaged bit error probability using a short sequence. There is another limitation of EPM. When the observed $\widehat{p}$ is less than the designed best p, one can not tell if the timing offset exists. In such a case, one must assume that the timing is correct and take the current delay estimate. This may lead to a large bit error probability on the next transmission.

The average bit error probability vs. length of probing sequence is given in Fig. 5.12 for the DSAM. As expected, an increased number of symbols in the probing sequence leads to a better bit error performance. In the plot, a time offset of $0.15T$ and $0.140625T$ (a special case) is used for the illustration. The second value corresponds to an amplitude quantization level $l_i = 0.78175$. From the plot, the average bit error probability tends to flatten when the number of probing symbols increases. When the offset is $0.15T$, which represents a normal situation (*i.e,* the signal level is not exactly at one quantization level), the curve (dashed line) tends to flatten sooner than the special case given in the plot (offset=$0.140625T$).

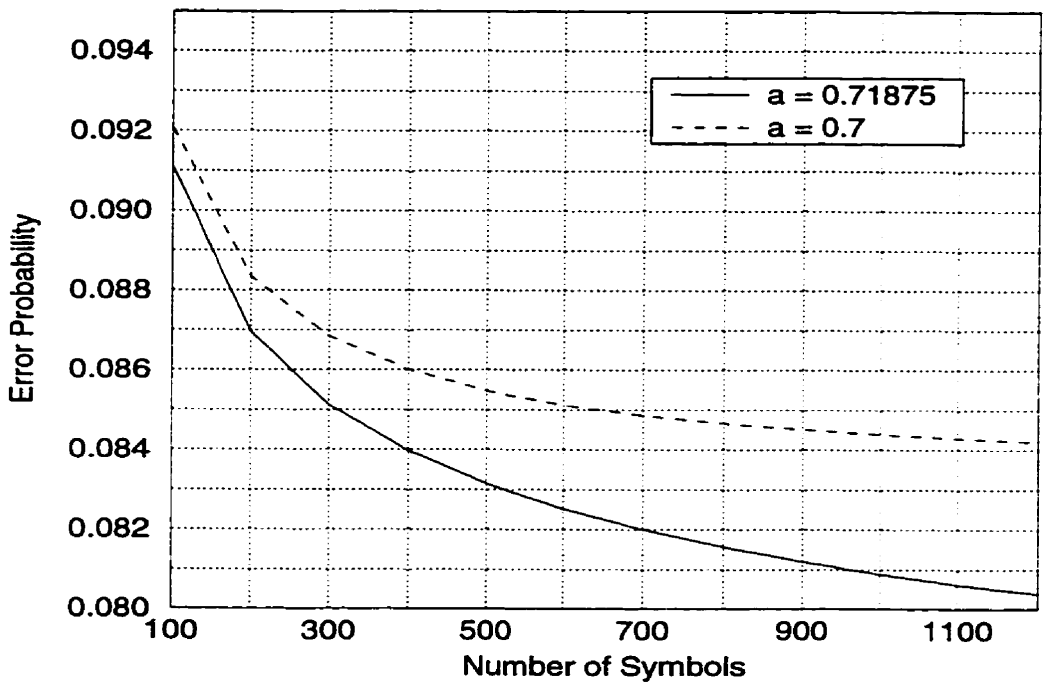

Figure 5.12: Bit error probability vs. Number of symbols (SNR = 0 dB)

Therefore, for the special case, more improvement can be expected.

The BER improvement is plotted in Fig. 5.13. In the figure, a fixed time offset of $0.15T$ is used for the outer curve. The SNR penalty is the result of the incorrect time delay estimate. By correcting this timing offset, a BER curve very close to perfect detection is obtained. An SNR penalty of less than 0.5 dB is observed for the averaged BER in the 10^{-3} region. In this figure, perfect carrier recovery is assumed and the only factor that causes the BER degradation is the timing error.

It is concluded here that for a short probing sequence, the EPM has a large variance. This large variance implies that each estimate is taken from a wide range of values and therefore, the resulting delay estimate is not consistent. On the other hand, though the DSAM has a residual estimate bias, it is consistent and the bias is very small. As long as the residual error is small (*i.e.* maximum quantization distortion q is small), the overall performance will be better than the EPM.

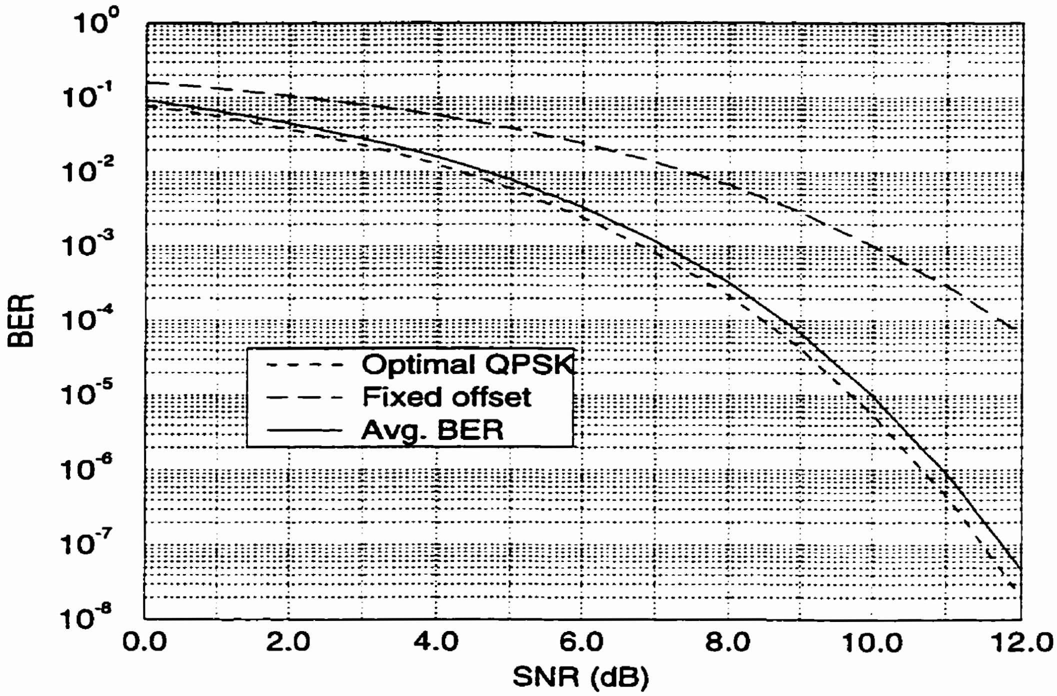

Figure 5.13: BER vs. SNR

5.2 Carrier Synchronization

5.2.1 Carrier Synchronization Consideration

Since the symbol timing must be recovered before the signal phase is recovered, it is desired to remove the phase term while preserving the magnitude information, As such, non–coherent propagation delay estimation will be considered. The magnitude of the uplink signal contains the timing offset information. A simple square–then–summation of the QPSK in–phase (I) and quadrature (Q) components removes the phase information. Let x and y represent the output of the I and the Q channels and the magnitude represented by r is given as

$$r = \sqrt{x^2 + y^2}. \tag{5.40}$$

This magnitude has a Rician pdf when both the I and the Q channels are corrupted by the additive Gaussian noise. If the noise power on each channel is σ^2 and the signal amplitude is a, then the Rician random variablehas a and σ as parameters and can be written as

$$p_R(r) = \frac{r}{\sigma^2}\exp\left(-\frac{r^2+a^2}{2\sigma^2}\right)I_0\left(\frac{ra}{\sigma^2}\right) \qquad 0 < r < \infty \tag{5.41}$$

If the estimate is made from only the magnitude in (5.40), the Rician distribution instead of the normal distribution treated earlier must be considered. The MLE discussed in section 5.1.2 can not be applied to the pdf in (5.41).

5.2.2 Modified Estimation Procedure

From (4.26), the output has two orthogonal components. When noise is considered, the output is

$$r = a\cos(\phi_k + \alpha_{k,m}) + ja\sin(\phi_k + \alpha_{k,m}) + n_c + jn_s. \tag{5.42}$$

ϕ_k and $\alpha_{k,m}$ are constant for the discussion. The real and imaginary parts are Gaussian random variables because n_c and n_s are Gaussian. Therefore, MLE can be applied to these two parts separately. Let $\widehat{x}$ and $\widehat{y}$ represent the two ML estimates from the two channels where x_i and y_i are samples from the two orthogonal channels such that

$$x_i = a\cos(\phi_k + \alpha_{k,m}) + n_c \tag{5.43}$$

$$y_i = a\sin(\phi_k + \alpha_{k,m}) + n_s \tag{5.44}$$

and $r = x_i + jy_i$. Then the estimates are given as

$$\widehat{x} = \frac{1}{n}\sum_i x_i \tag{5.45}$$

$$\widehat{y} = \frac{1}{n}\sum_i y_i \tag{5.46}$$

and the means of the estimates are

$$E[\hat{x}] = a\cos(\phi_k + \alpha_{k,m}) \tag{5.47}$$

$$E[\hat{y}] = a\sin(\phi_k + \alpha_{k,m}). \tag{5.48}$$

Also, the variances are

$$\mathrm{Var}[\hat{x}] = \frac{\sigma^2}{n} \tag{5.49}$$

$$\mathrm{Var}[\hat{y}] = \frac{\sigma^2}{n} \tag{5.50}$$

where n samples are used to obtain the estimates. The estimates $\hat{x}$ and $\hat{y}$ are unbiased and efficient as stated in (5.7). The magnitude of this complex estimate $(\hat{x} + j\hat{y})$ is

$$\hat{r} = \sqrt{\hat{x}^2 + \hat{y}^2}. \tag{5.51}$$

When $\hat{x}$ and $\hat{y}$ are close to their means, the estimated MCD output magnitude is close to its true value. The unknown phase information is removed completely when $\hat{x}$ and $\hat{y}$ reach their respective means.

Since $\hat{x}$ and $\hat{y}$ are Gaussian random variablescharacterized by their means and variances, the random variable$\hat{r} = \sqrt{\hat{x}^2 + \hat{y}^2}$ still obeys the Rician distribution.

It is known that when $a \gg \sigma$ in (5.41), the Rician pdf can be approximated by the Gaussian distribution [57]. This conclusion is clearly shown in Fig. 5.14 and Fig. 5.15. In Fig. 5.14, the dashed line shows a Rician pdf and the solid line a Gaussian pdf. The difference between the two curves, though not very large, is easily noticeable. In Fig. 5.15, since the random variable values concentrate around a, those two distributions are virtually identical.

The approximate pdf is obtained as follows. From (4.8), using the expansion of 0th order Bessel function $I_0(z)$ for $z \gg 1$ [77]

$$I_0(z) = \frac{e^z}{\sqrt{2\pi z}}(1 + \frac{1}{8z} + \frac{9}{128z^3} + \cdots +) \approx \frac{e^z}{\sqrt{2\pi z}} \tag{5.52}$$

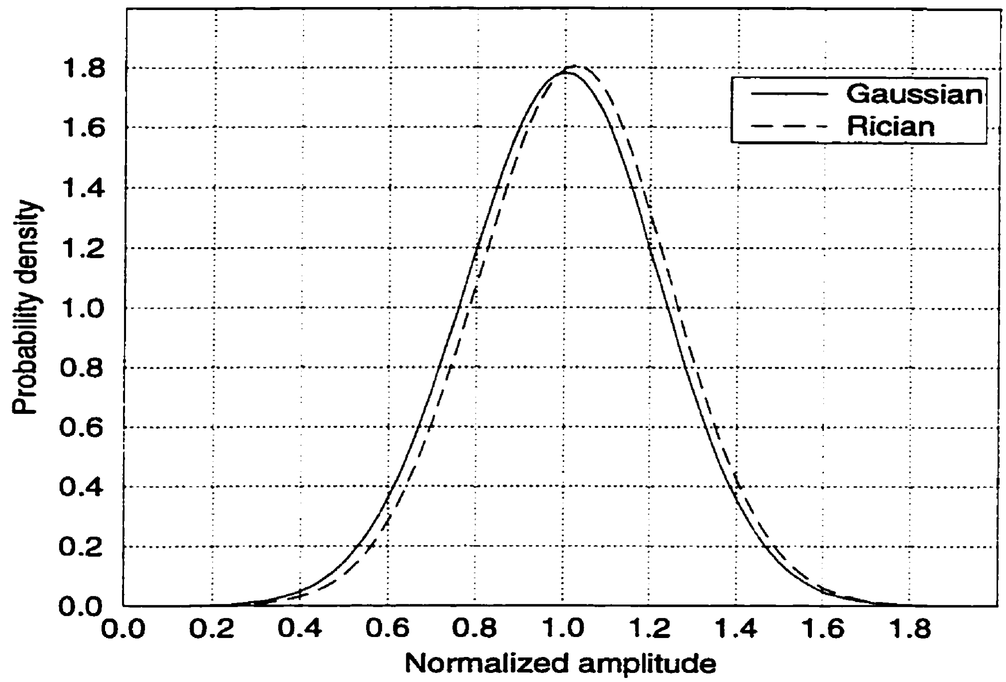

Figure 5.14: Rician and Gaussian Distribution

substitute ra/σ^2 for z in (5.52) and expand (4.8), then the probability distribution becomes

$$p_R(r) = \frac{r}{\sigma^2}\exp(-\frac{r^2+a^2}{2\sigma^2})\frac{e^{ra/\sigma^2}}{\sqrt{2\pi ra/\sigma^2}} \qquad 0 < r < \infty. \tag{5.53}$$

the two exponential terms can be merged to one, then by rearranging the variables in the above equation an approximate pdf is obtained in (5.54)

$$p_R(r) = \frac{1}{\sqrt{2\pi}\sigma}\exp(-\frac{(r-a)^2}{2\sigma^2})\sqrt{\frac{r}{a}} \tag{5.54}$$

The approximate is correct because after estimation, $a \gg \sigma$ and σ is small. For any $r \neq a$ the exponential term goes to zero quickly and for those $r \approx a$, $\sqrt{r/a} \approx 1$. Therefore $p_R(r)$ is approximately Gaussian.

5.2.3 Resulting Estimates

The fact that the Rician pdfs can be approximated by Gaussian pdfs when a is much larger than σ makes it possible to use conclusions obtained in section 5.1 where the possibility of obtaining estimates for the Gaussian random variablesare discussed. In this section it is

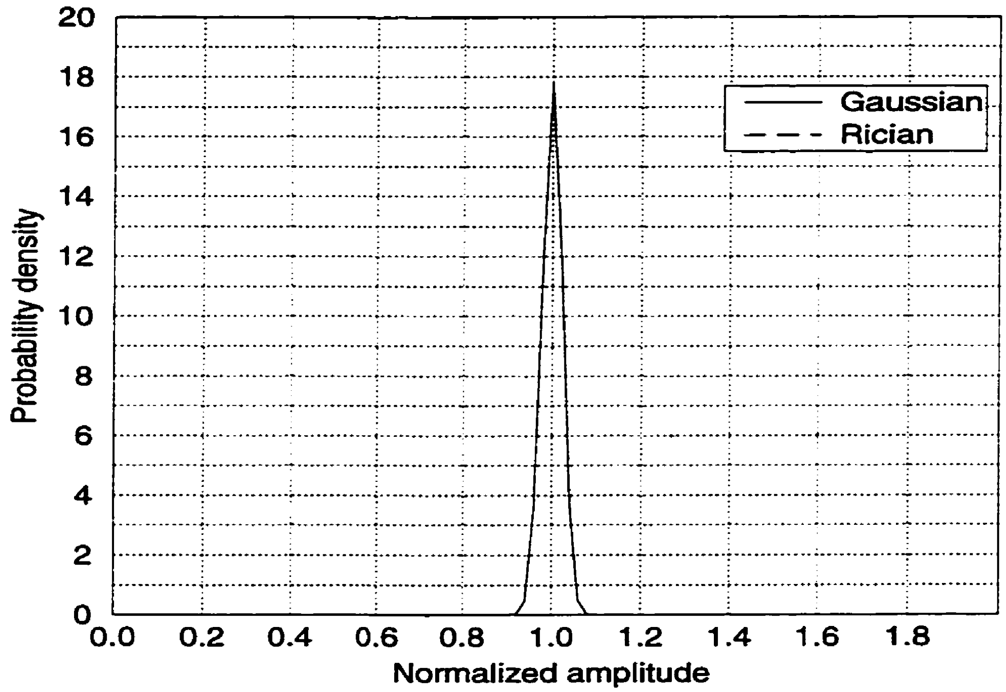

Figure 5.15: Rician and Gaussian Distribution for $a \gg \sigma$

shown that these results are applicable to the estimates formed from the I and Q channel estimates.

As mentioned in subsection 5.1.2, the variances of the estimates are N times smaller than that of the variances before averaging. Since the means of the estimates are the same as the original random variables, the new random variablederived from I and Q channel estimates through $r = \sqrt{x^2 + y^2}$ can be approximated by a Gaussian pdf for a sufficiently large N.

By applying different a/σ to both Rician and Gaussian pdfs and checking the plots visually, it is found that when $a/\sigma > 10$, both pdfs become identical. Fig. 5.15 shows this point clearly (where $a = 10\sigma$).

This criterion can be extended to the range $a/\sigma > 1.3$ when quantization is used after the estimation process (this is the case in the implementation studied in Chapter 6). All the previous conclusions hold. Namely, the estimates can be obtained with 100 probing symbols, the estimates has a mean linearly related with the timing error for non-windowed inputs and there is a lower bound for the variances of the estimates. This conclusion is demonstrated through computer simulations in Chapter 6. Here the probabilities of making the estimation are compared with the previous Gaussian amplitude case. The probability of making an estimate within one quantization step is

$$P = \int_{l_i - q}^{l_i + q} p_R(r)dr \tag{5.55}$$

where l_i is the ith quantization level and the step size is $2q$. For $a = 0$, which corresponds to a timing offset of one half of the symbol length, $p_R(r)$ is the Rayleigh pdf. For $a \neq 0$, $p_R(r)$ is the Rician pdf.

When the Rayleigh pdf is considered, (5.55) becomes

$$P = \int_0^{2q} \frac{r}{\sigma^2} \exp(-\frac{r^2}{2\sigma^2})dr = 1 - \exp(-\frac{2q^2}{\sigma^2}). \tag{5.56}$$

It is worthwhile to indicate that σ^2 would be replaced by σ^2/N if the discussion is on the estimate made from N samples. When 16 quantization levels are used, the step size is $2q = 1/16$. Here q is normalized with respect to the symbol length T. The estimate is made from a 100 symbol probing sequence. For $E_b/N_0 = 10$ dB, the probability is 0.98. That is in one hundred transmissions, ninety eight of them is expected to fall in the region of zero to $2q$. This result is very close to the one given in Fig. 5.8 where the same SNR and estimate sequence length are used. For $a \neq 0$ and assuming σ is small, then the Gaussian approximation can be used to obtain the acquisition probability, which is

$$P = \int_{l_i - q}^{l_i + q} \frac{1}{\sqrt{2\pi}\sigma} \exp(-\frac{(r-a)^2}{2\sigma^2})dr \tag{5.57}$$

where the subscript i depends on the signal value of a. This probability can be easily computed using numerical integration if a and σ are available. Equation (5.57) can be written as

$$P = p(l_i) = Q(\frac{l_i - q - a}{\sigma}) - Q(\frac{l_i + q - a}{\sigma}). \tag{5.58}$$

For example, if use $E_b/N_0 = 10$ dB, with $a = 0.7A$ and a 4–bit quantizer used, $q = 0.03125$ and the normalized quantization level corresponds to the a is $l_i = 0.71875$. From Eqn.

(5.58), the probability is approximately 0.7, which matches the probability for SNR = 10 dB given in Fig. 5.4.

5.3 Selected Estimate Method

From above discussions, it is concluded that the preferred estimation method is given in section 5.2.2; that is, detection amplitude estimation with non–coherent combining and quantization for downlink TDM transmission. The system simulation in the next chapter will be based on this estimation algorithm plus all the supporting functions necessary in a practical communication system.

The delay estimate through BER monitoring had been simulated in Chapter 4. This method provides an alternative to the amplitude estimate method. The BER method is useful if the probing signal power is restricted to a very low level or when SNR is much lower than the normal operation value.

In the next chapter, a complete satellite system, with the delay estimation algorithm discussed above embedded in it, is simulated. The results are compared with those from this chapter.

Chapter 6

Simulation

In this chapter, the simulation of a two–way link between a terminal and a processing satellite communication system is presented. The simulated system is an FDMA/TDM system with possible addition of TDMA to the uplink. The delay estimation algorithm described in section 5.2.2 on page 108 of Chapter 5 is evaluated in the simulation. The implementation of each part of the system is explained and a complete system simulation is then performed. Interactions between the satellite and a ground terminal are considered, and whenever possible, simulation results are compared with their theoretical counterparts from Chapter 5. However, in this chapter the performance of the uplink propagation delay estimation algorithm is evaluated in a closed–loop system involving a ground–bound terminal and a processing satellite.

6.1 System Configuration

A block diagram for a computer simulation model which is developed in this chapter is shown in Fig. 6.1. Instead of going directly into the description of individual subsystems in Fig. 6.1, it is better to start with an overall system description.

Any communication system consists of a transmitter and a receiver. The former con-

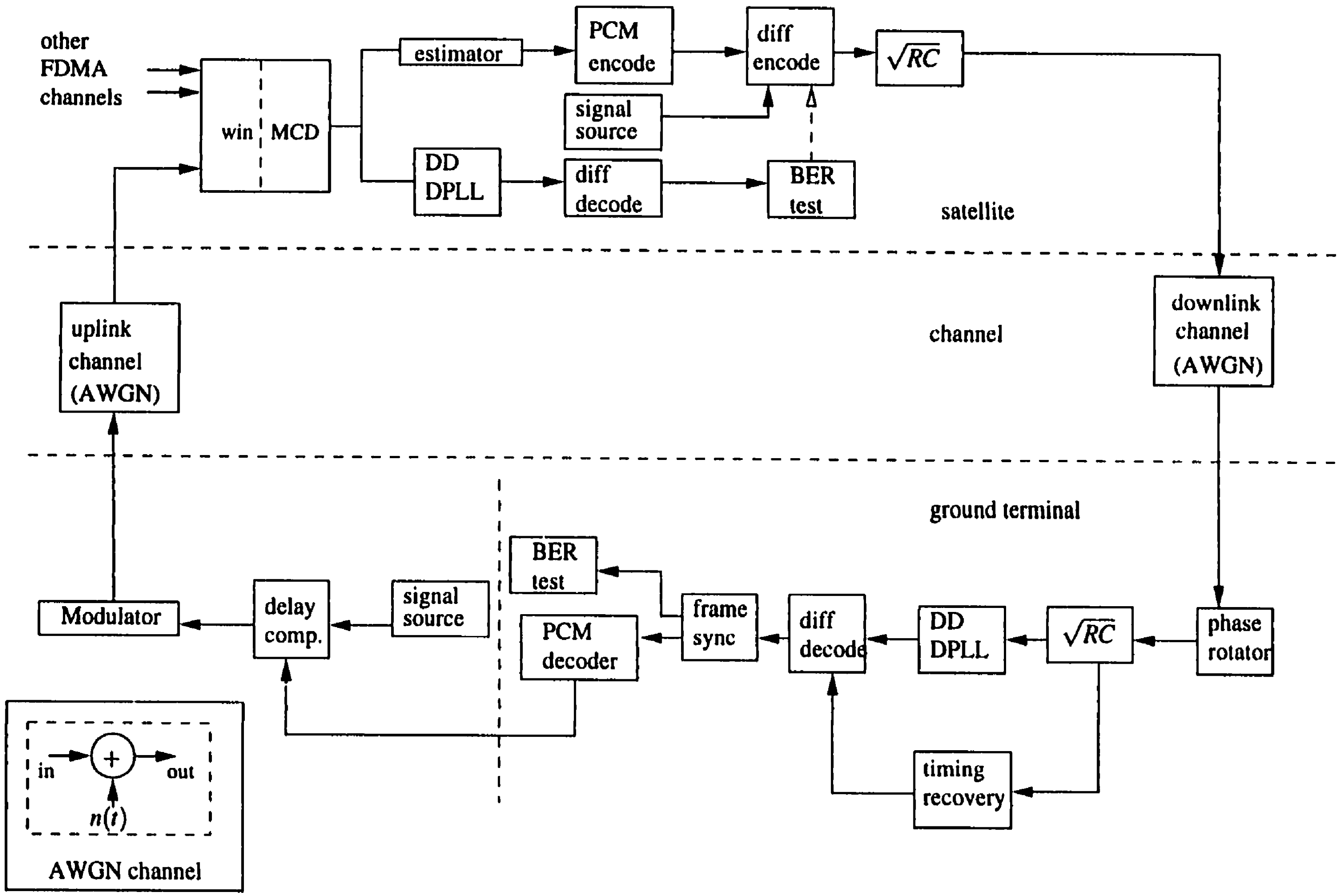

Figure 6.1: The Complete Simulation Model

tains a signal source, a modulator and associated control functions while the latter contains a demodulator, a signal sink and necessary controlling functions. The simulation model presented here is designed to simulate the process of an user accessing the system resources in order to communicate with other users in the system. The model includes three basic parts, the processing satellite, a ground terminal, and downlink and uplink channels. The satellite transmitter and the ground terminal receiver form the satellite downlink while the ground terminal transmitter and the satellite receiver form the satellite uplink. On–board amplitude estimation is modelled in the system simulation and the propagation delay estimation algorithm presented in section 5.3 of the last chapter is embedded in this system. A detailed initialization procedure which allows an user to access the system will be given in section 6.4.1.1.

Some of the subsystems, such as the maximum length pseudo random sequence generator used as signal source [22], the timing recovery function [29], the decision–directed discrete PLL (DD–DPLL) [37], and the raised–cosine (RC) pulse shaping filter [72] in Fig. 6.1 are well known from the literature. For consistency, however, all the functions shown in Fig. 6.1 are briefly described below. The description is grouped into the ground terminals, the satellite payload, and the common functions. Here a common function means that those functions appear in both the ground terminal side and the satellite side. The block diagram for the system to be studied is given in Fig. 6.1.

1. The ground terminals:

    - Delay compensation (delay comp. in Fig. 6.1): this function compensates the uplink propagation delay by adjusting the uplink clock phase. It is controlled by the information obtained from the delay estimation subsystem.
    - Modulator: this modulation function converts the bit stream of the signal source to a complex lowpass equivalent modulated signal. Pulse shaping is performed

Frame Header (15–bit)	Information block (24 uplink channels in sequence)

Figure 6.2: Illustration of Frame Header in a TDM Frame

here if such a function is required. QPSK modulation with differential encoding is used in the simulation.

- D/A: this function decodes the delay information estimated on–board the satellite and converts the digits to analog values and the information is sent to the delay compensation block. When in communications mode, the differentially decoded signals are sent to BER tests instead of the D/A block.
- Frame sync: this function detects frame header in the downlink bit stream. A 15–bit frame header is used in the simulation. Each downlink TDM frame contains a header and an information block as shown in Fig. 6.2.
- Timing recovery: this function recovers the timing boundary of each symbol from the incoming downlink signal. The timing error detection algorithm is taken from [29].
- Phase rotator: this function simulates the errors made in the down conversion of the carrier frequency of the downlink signal. Phases of the incoming signal and the local oscillator are generally not coherent and therefore, the output of the phase rotator contains both modulation and an unknown phase offset.

2. The satellite payload:

    - MCD (multicarrier demodulator): this is implemented using the characteristics of SAW devices. The chirp Fourier transform derived in [34] is simulated using the MCM configuration shown in Fig. 3.3. The windowing function, denoted by “win” in the figure, is required to reduce the sidelobe amplitude of each FDMA channel mapped to a time sequence [35].

- Estimator: this function estimates the uplink signal amplitude. The transmitter timing recovery depends on the information from this estimator.
- A/D: this function encodes the estimated signal amplitudes to a digital form. When on–board estimation is used, the estimated signal amplitude is quantized using linear quantization for TDM downlink transmission.

3. The common functions:

   - Signal source: this function produces a pseudo random or alternating zero and one sequence. In case of a random sequence, the signal is obtained from a linear shift register with feedback. A pseudo random sequence of length is $2^{11} - 1$ is used to perform the BER test. The source on the satellite side is also used to provide a specific frame synchronization header. The frame synchronization is necessary to delimit the information boundary of satellite downlink data stream. More on frame synchronization is discussed later in subsection 6.3.6.
   - Noise generator: this function generates random Gaussian noise. The noise signal is added to the output of modulator to simulate the AWGN channel. The side–bar in Fig. 6.1 shows how the AWGN channel is modelled.
   - DD–DPLL: decision directed digital phase locked loop. This subsystem tracks the unknown carrier phase/frequency offset. Bit decisions are made in the PD after symbol timing is recovered and the bit stream is then differentially decoded. The uplink BER test is made after differential decoding. The output can be remodulated and transmitted on the downlink but this downlink may not necessarily be connected to the transmitting ground terminal. This DPLL consists of three functions, which are not shown separately in Fig. 6.1.
     - phase detector(PD): this function detects the phase error. The function used

in the simulation is adopted from [37] with modification. The information symbol decision is made here.

- loop filter (LF): this is a first order IIR filter described by Gardner in his book "Phaselock Techniques" [83]. By adding a pole using this filter to the loop, a second order PLL is obtained. It produces frequency–offset compensation in the carrier recovery process.
- VCO: this is modelled as an ideal integrator. It outputs a complex phase correction signal with constant magnitude.

- differential encoder/decoder: the signal is differentially encoded on the transmitter side to combat the carrier phase ambiguity introduced by the PLL on the receiver side. The differential decoder is required in order to recover the original information on the receiver side.
- The $\sqrt{RC}$: this symbol means that the filter $\sqrt{RC}$ has the square–root raised cosine finite impulse response [72]. Raised cosine pulse–shaping is used in the downlink. The pulse shaping filter uses the square root of this raised cosine function and a filter matched to the transmitter pulse shape is used in the ground terminal receiver, which is thus also a $\sqrt{RC}$ filter.

All above functions are integrated together to form a closed–loop satellite communication system with an uplink and a downlink. All functions are driven by a common clock – the master clock on–board the satellite.

In the next two sections, the performance of each function is examined. In section 6.2, the delay estimate algorithm described in the section 5.2.2 of Chapter 5, namely the detected signal amplitude method (DSAM), is simulated in a stand–alone program. The statistical performance of this algorithm is obtained in section 6.2. In section 6.3, all related functions necessary for the system simulation are separately implemented and tested. These two sections show the construction of the simulation system.

6.2 Simulation of the Delay Estimation Algorithm

The delay estimate function which is an implementation of the algorithm described in section 5.2.2 is evaluated by the characteristics of the estimation of the timing strobes or clock phases. Attempts are made to determine the probing signal length from the probability distributions and the mean square error of the estimates.

To make the further discussion easier to follow, the estimation method is briefly stated here again. Estimation is performed on in–phase and quadrature channels separately and these estimates are then squared and added to remove the unknown phase offset which presents in the frequency down converted uplink signals. The combined signal is quantized in order to be transmitted on the satellite TDM downlink channel. The performance of this method as a subsystem was considered in section 5.2.3. Here its performance is examined in a full system simulation.

The pdfs of the quantized signal amplitude are discrete and for different amount of time offset, the pdfs of the magnitude estimates are different. The shape of pdfs are also affected by the number of symbols used to get estimates. Since sixteen samples are taken in one symbol period, nine steps are used in the simulation to represent a timing offset range of $[0, T/2]$ because the algorithm will recognize only the amount of timing offset not the polarity. The probing signal is chosen to generate a linear offset vs. amplitude output. Such a signal is obtained by changing the modulating signal phase by π radius every T sec.

First, the normal situation when the timing offset is around the center of 0 and $T/2$ is examined. In this and the subsequent simulations, if not otherwise specified, the operating SNR, which determines the variance of the received signal, is 10 dB. The mean of the received random variables depend on the amount of the timing offset. The theoretical pdfs in those plots are obtained from Rician distribution given in (4.8) using the same SNR and mean parameters. Fig. 6.3 and Fig. 6.4 show the pdf results with different length of probing sequence. Instead of using 16 levels for half symbol length in Chapter 5, here nine levels

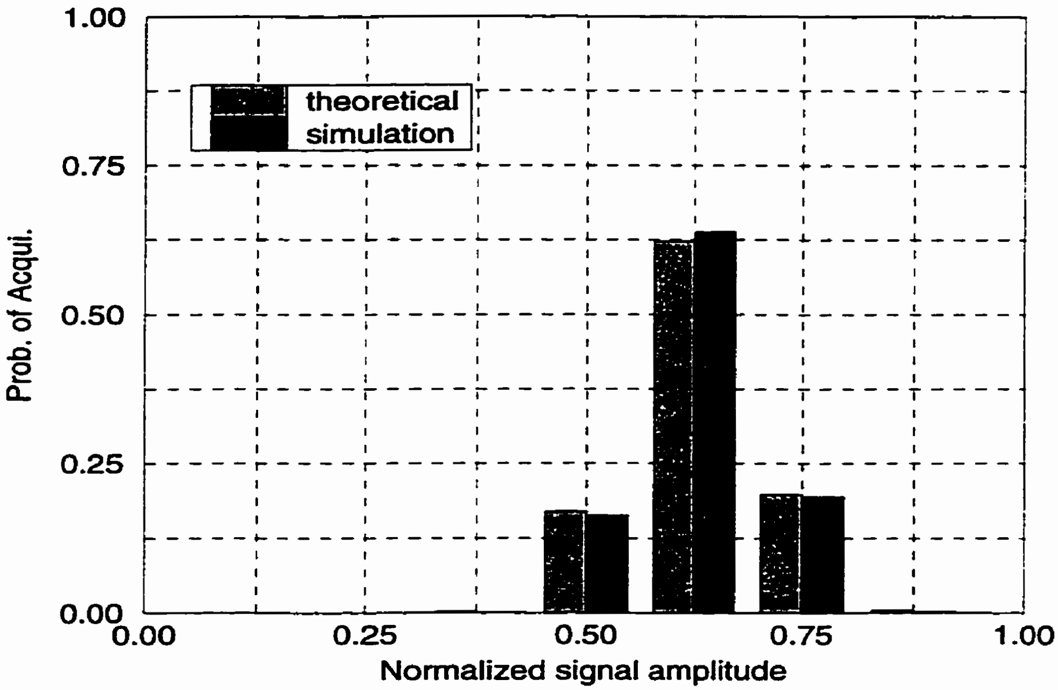

Figure 6.3: Typical Discrete pdf of Estimates from Short Sequence (offset = $3T/16$, average over 10 symbols)

are used for $[0, T/2]$. The time offset used in the simulation is $3T/16$. Though 9 signal levels are plotted in Fig. 6.3, almost all estimated signal amplitudes fall on 0.5, 0.625 and 0.75. The values here are the normalized quantization levels. A very small probability can be observed on 0.375 and 0.875 and zero probabilities are obtained for other signal levels in Fig. 6.3. From this plot, even with only 10 symbols, the procedure yields an acceptable estimate of the signal amplitude. With 100 symbols, the correct estimate of timing has a probability larger than 0.99. In either case, the largest probability is associated with the true signal magnitude, which is normalized to 0.625.

If the timing offset is small, the detected signal amplitude will be high since the arguments, when normalized, are limited to between 0 and 1 and thus the discrete probabilities have a larger portion concentrated on the higher amplitude side. Therefore, the probabilities of making a correct estimate are larger for both short and long sequences. This point is shown in Fig. 6.5 and Fig. 6.6 with the timing offsets of zero.

Now consider another extreme case. This is when timing offset is about one–half a

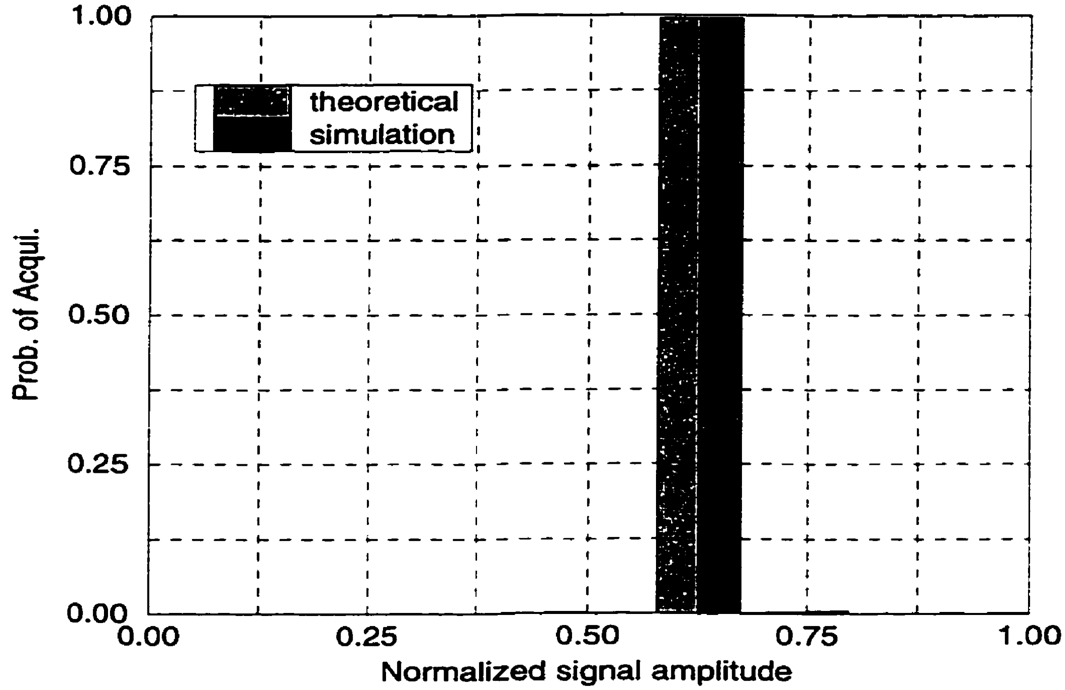

Figure 6.4: Typical Discrete pdf of Estimates from Long Sequence (offset = $3T/16$, average over 100 symbols)

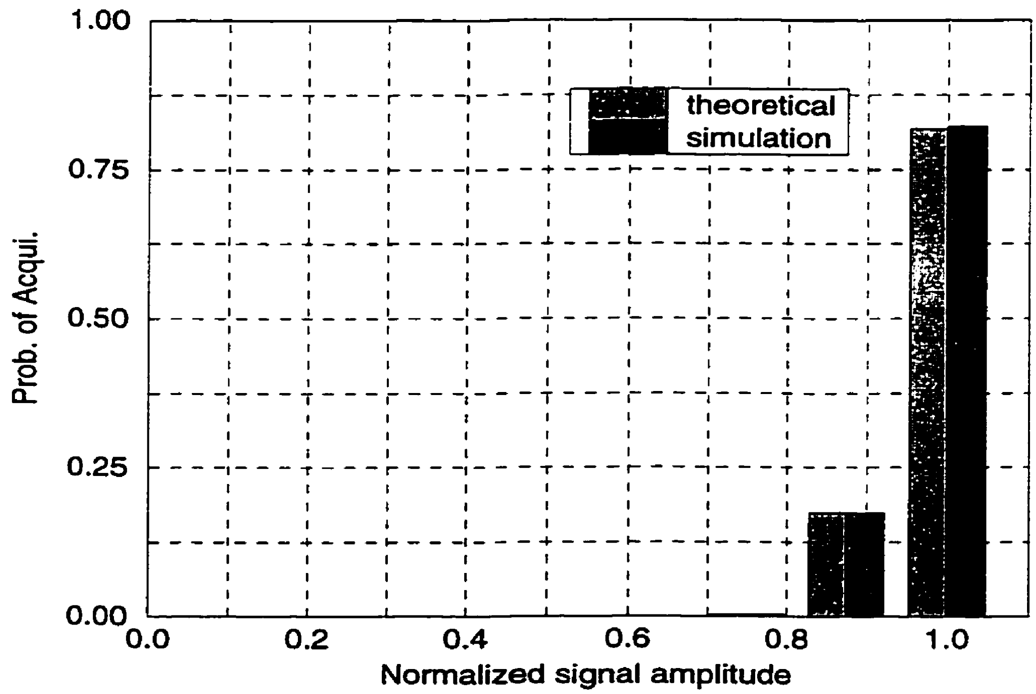

Figure 6.5: Discrete pdf of Estimates for Small Offset from a Short Sequence (offset = 0, average over 10 symbols)

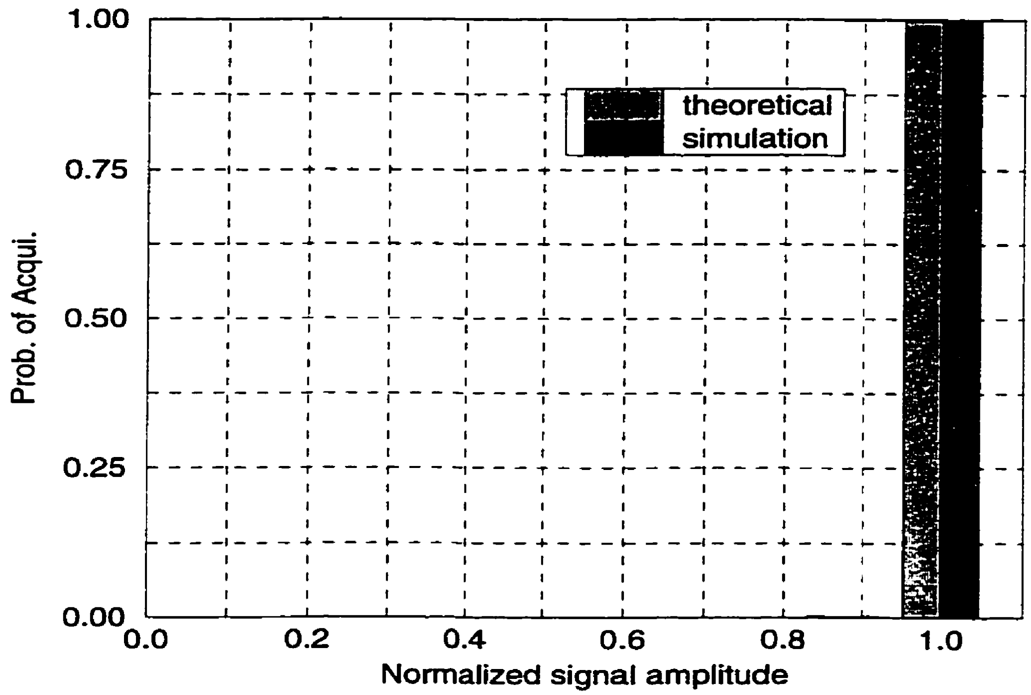

Figure 6.6: Discrete pdf of Estimates for Small Offset from a Long Sequence (offset = 0, average over 100 symbols)

symbol length. Under such a circumstance, the detected signal magnitude is very low and consequently the effective SNR is small because the noise component remains the same regardless of how the timing offset changes. Therefore, estimates from both channels have larger variances and smaller means. As illustrated in section 5.2.2, the Rician pdf differs in shape from the Gaussian pdf in such an environment. As expected, the estimate process yields an incorrect signal amplitude estimate if a short probing signal is used due to the effect of the non–negative Rician pdf as shown in Fig. 6.7, where a zero amplitude was expected. The magnitude is estimated correctly if a longer sequence is used as shown Fig. 6.8, where 100 symbols are used to make one estimate.

The above discussion was focused on the estimated signal magnitude. To obtain the propagation delay information, this magnitude information needs to be mapped to the amount of timing offset. The linear relationship given in (5.1), where A was 1, is given here as (6.1)

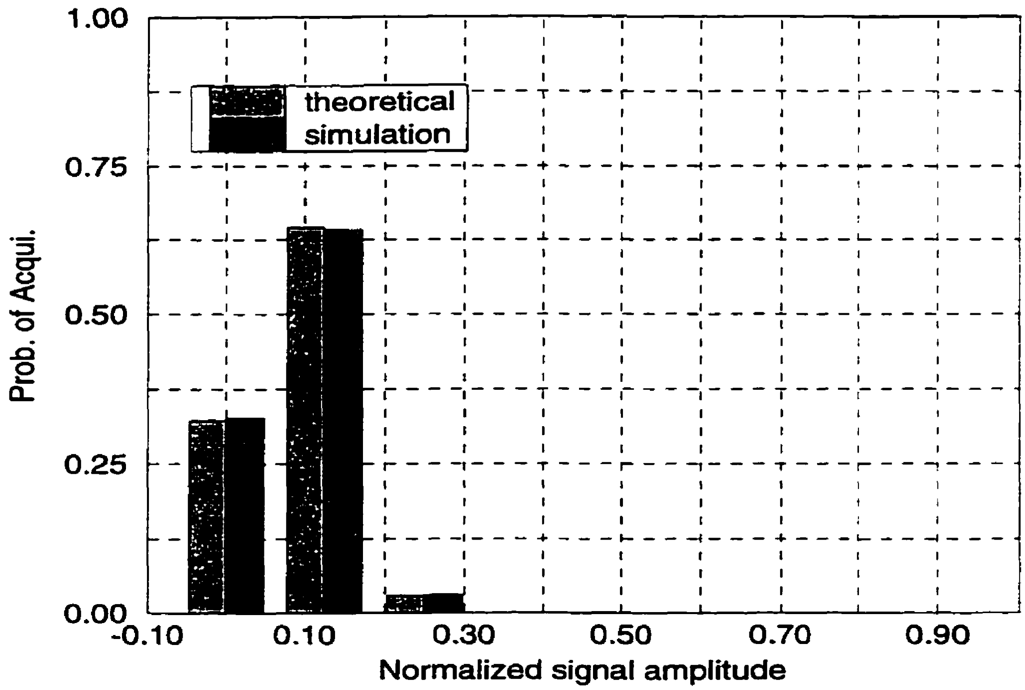

Figure 6.7: Discrete pdf of Amplitude Estimates for Large Offset from a Short Sequence (offset = $T/2$, average over 10 symbols)

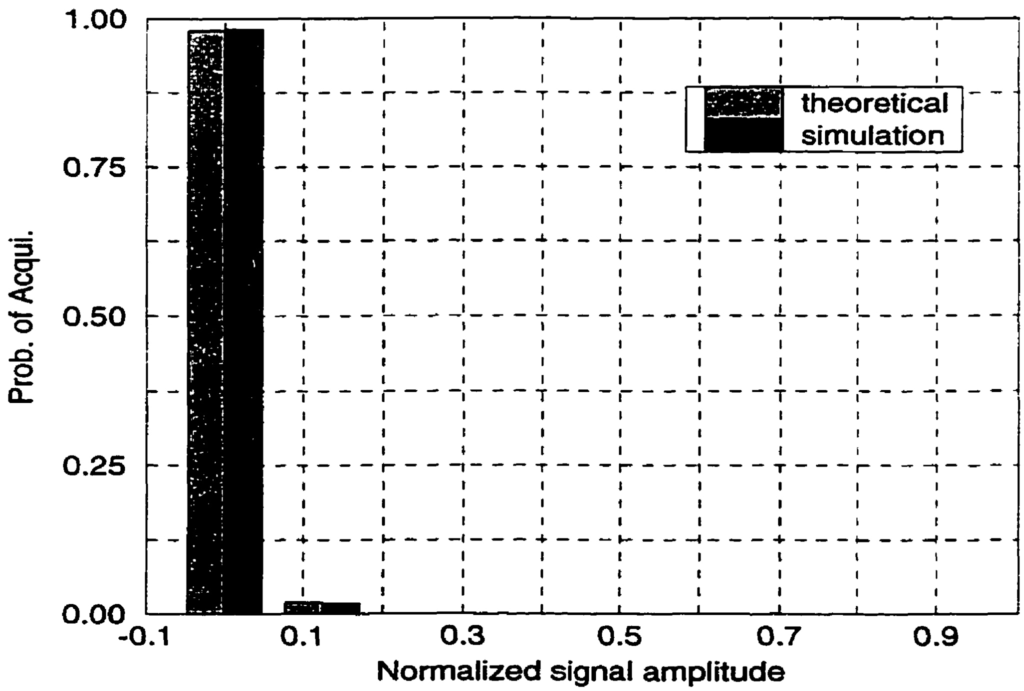

Figure 6.8: Discrete pdf of Amplitude Estimates for Large Offset from a Long Sequence (offset = $T/2$, average over 100 symbols)

$$a = (1 - 2\frac{T_e}{T})A \tag{6.1}$$

and it is used to obtain the timing offset. This relationship is obtained from the MCD output with probing signal format described on page 120. Here T_e is the estimated timing offset in the delay estimation, T is the uplink symbol period and the T_e/T is the normalized timing offset. The correct estimate leads to zero residual timing error. The residual timing error, denoted by T_r, is defined as

$$T_r = |T_e - T_{off}|. \tag{6.2}$$

where T_{off} is the true timing offset and T_e is the estimated timing offset as defined above. All residual timing errors are assumed positive. Therefore, over corrections and under corrections are combined together if they lead to the same T_r. Different amounts of offset produce different pdfs of residual timing error since the discrete pdfs of magnitude estimates are different in terms of correctly estimated magnitudes. This is true especially for short probing sequences as can be seen from Fig. 6.9. In the figure, the residual timing offset is obtained from (6.2). T_{off} is used as the parameters given in the figure and T_e is computed from (6.1) once a/A is estimated. For both situations, the use of a shorter sequence and a longer sequence to probe the timing offset are examined. In Fig. 6.9, as the amount of timing offset increases, the probability of making incorrect estimate increases. To observe this performance compare the resulting pdf with those in Fig. 6.3 and Fig. 6.7, where the probabilities are given as functions of estimated signal magnitudes. It is clear that the probability of estimates with error on both sides of the correct estimate are combined in the residual timing error pdf. The Rician pdf is the result of the low signal magnitudes from large timing offset and causes a high probability of incorrect estimate and consequently a high residual timing offset. The situation improves in Fig. 6.10, where 100 symbols are used to obtain the timing estimate. Other parameters used for this figure are the same as in Fig. 6.9. In this figure, regardless the amount of offset, the delay estimate algorithm will

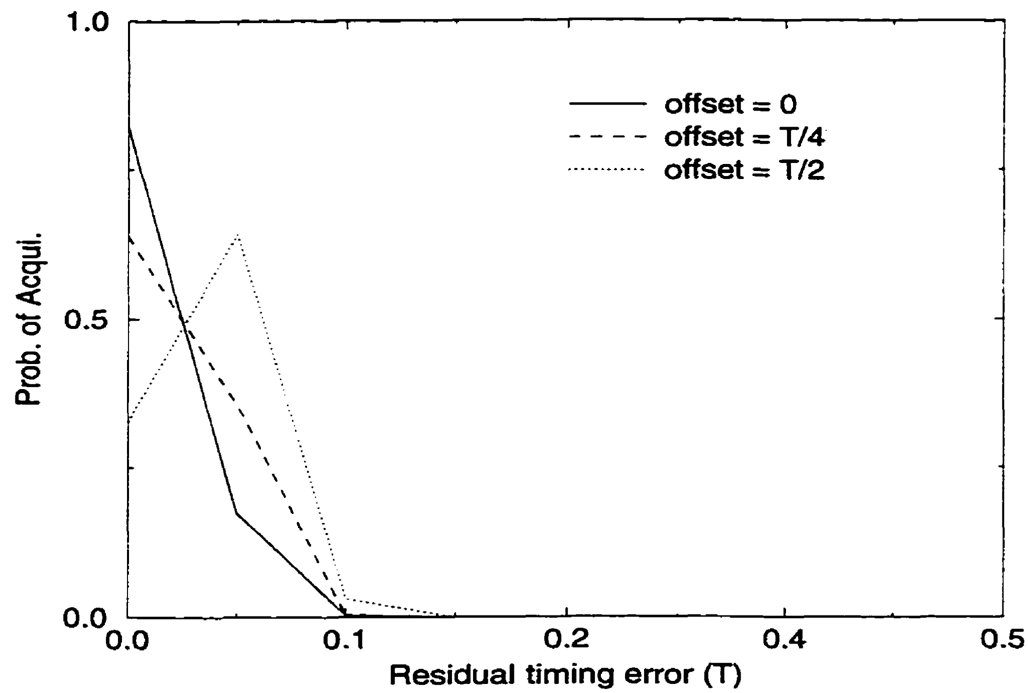

Figure 6.9: PDF of Residual Timing Errors for Estimates from a Short Sequence ($N = 10$)

produce a correct estimate with a very high probability. The difference in terms of timing estimate performance among the three timing offsets considered here is negligible.

To get a sense of how the timing estimate improves, the probability of making a correct magnitude estimate against the number of symbols used to form the estimate is plotted in Fig. 6.11. In this plot, the estimate is performed from all input symbols and updated as new symbol arrives at the satellite detector. This figure shows that if the probing signal length is longer than 100 symbols, the estimate becomes accurate and stable regardless of the size of the timing offset. Therefore, 100–symbol is suggested as the probing sequence length and is used in the system simulation given later in this chapter.

The suggested probing signal length of 100 symbols can also be justified from the mean square error (MSE) plot given in Fig. 6.12. The MSE in the plot is calculated using

$$\text{MSE} = \sum_{i=0}^{L}(T_r(i))^2 p(i) \tag{6.3}$$

where $T_r(i)$ is the residual timing offset and $p(i)$ is the probability corresponding to the timing offset in pdf of the residual timing error. T_r is obtained from (6.2). The $p(i)$ is

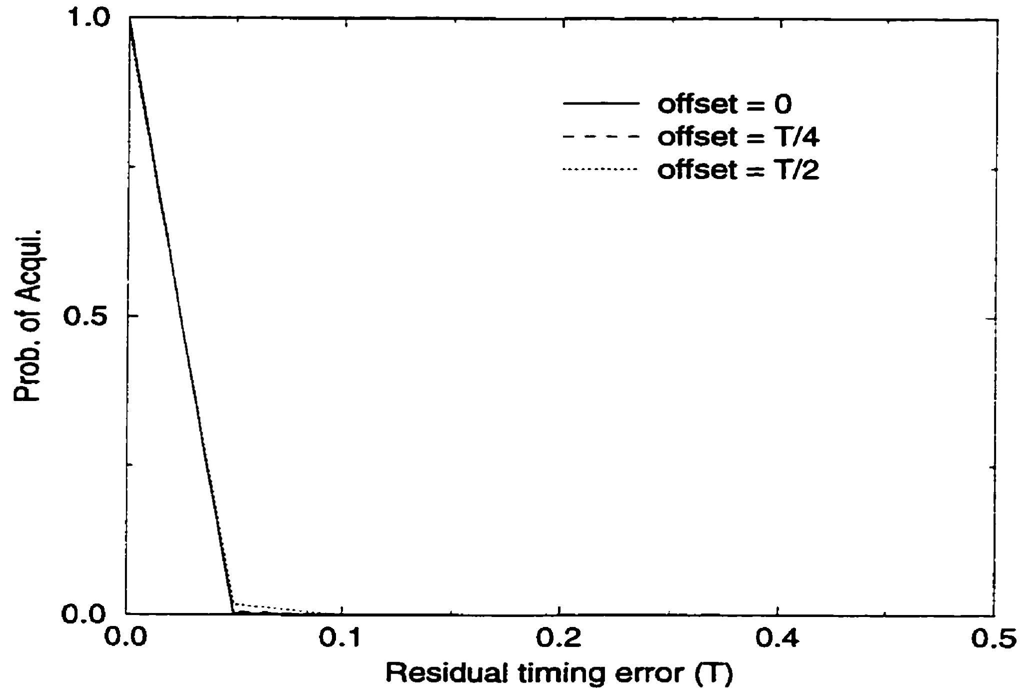

Figure 6.10: PDF of Residual Timing Errors for Estimates from a Long Sequence (N = 100)

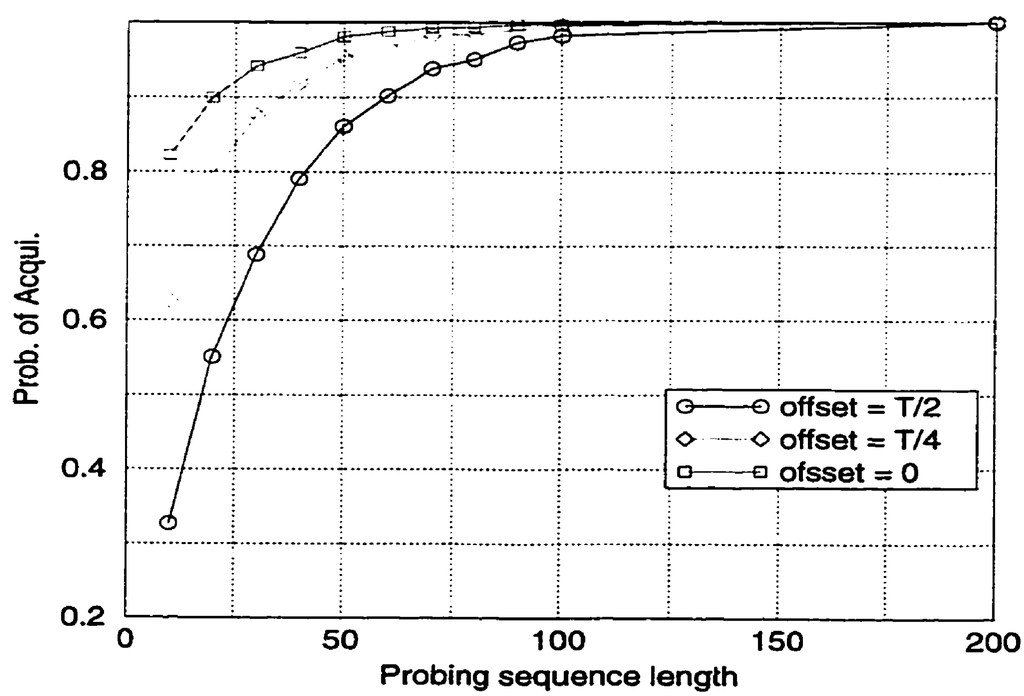

Figure 6.11: Effect of the Amount of Timing Offset on the Estimate

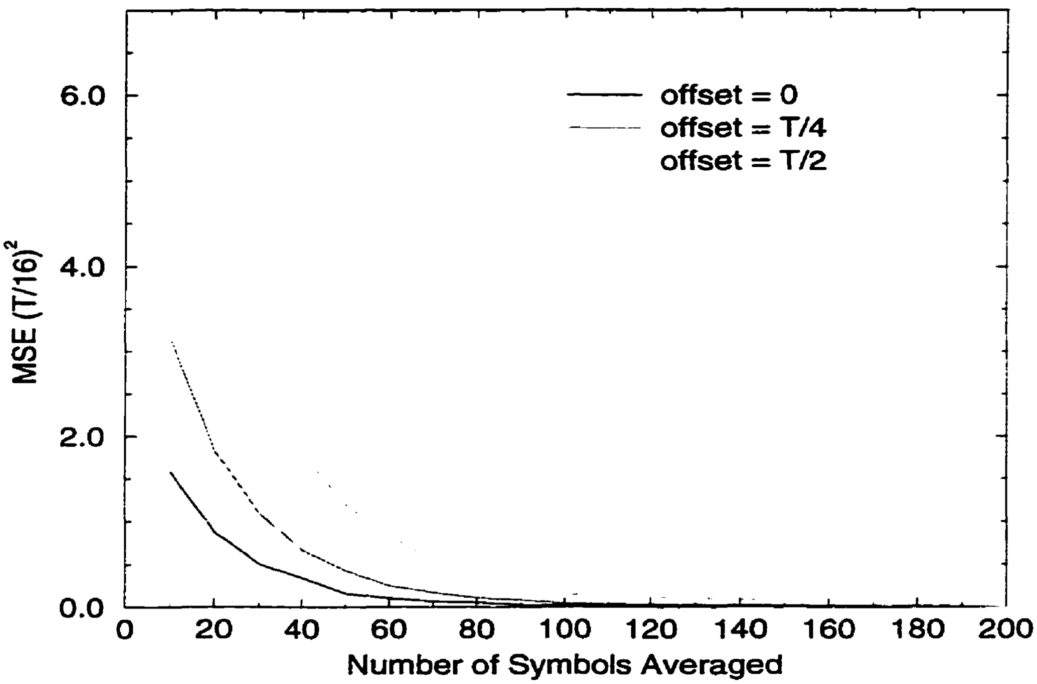

Figure 6.12: Mean Square Error of Residual Timing Errors

determined by running the timing estimate simulation program over $N = 3000$ symbols with a fixed amount of timing offset and examining the frequency that the estimates fall on level i. Then divide this frequency by N to determine $p(i)$. Note that $L = 8$, is one half of the total samples per symbol. Because T_r is the error in timing offset estimation, Eqn. (6.3) gives the MSE.

The reliability of the estimation algorithm is examined by simulation where a probability of 0.90 is set as the threshold of successful estimation. If the probability of the correct estimate is less than the threshold, it is said that the procedure fails to produce the desired estimate. The failure point is studied as a function of operating SNR and the result is plotted in Fig. 6.13 with the length of probing sequence as a parameter. This plot shows the case that the timing offset is $3T/16$ where the pdf of the estimated signal magnitude approximately follows a Gaussian distribution. Again longer probing sequences produce more reliable timing estimates. From this figure, it is clear that if a 200–symbol sequence is used, the correct estimate can be obtained easily even with a low SNR of 3 dB. On the other hand, a higher SNR is required for a proper estimate of timing offset if a shorter sequence

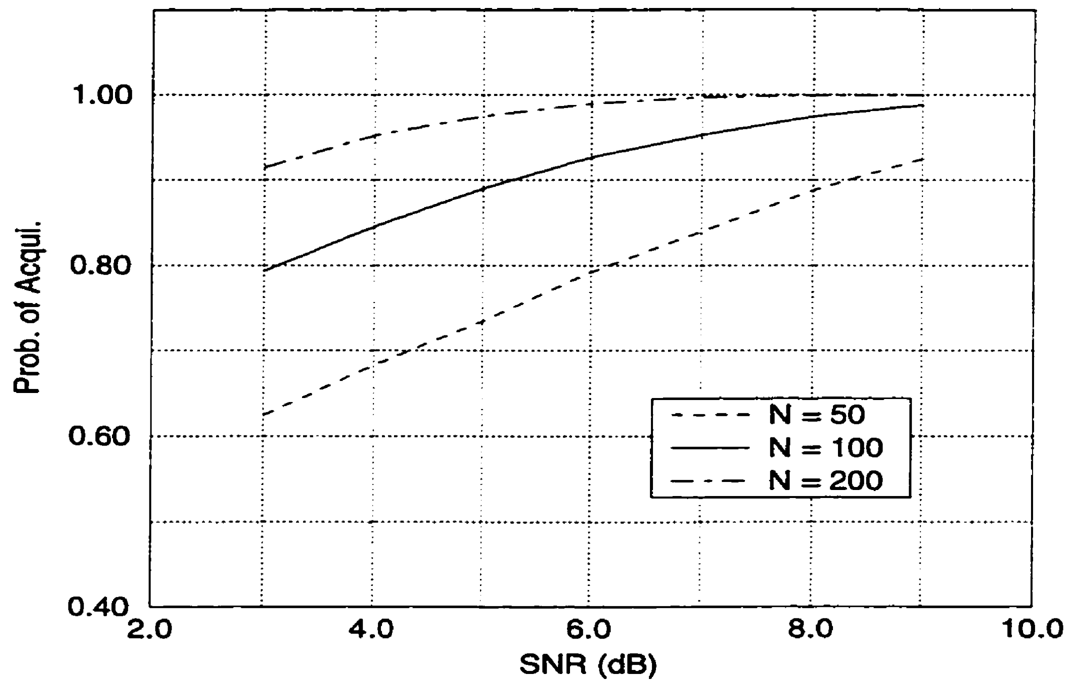

Figure 6.13: Probability of successful estimates (offset = $3T/16$)

is going to be used. To compromise between estimation speed and SNR requirement, a 100–symbol sequence is used in later simulation results. Such a sequence can successfully produce the desired estimate for an SNR as low as 5 dB which is a lower limit for most satellite communication applications.

The situation of large timing offset is slightly different from the moderate timing offset case. Under the large offset condition, the detected signal amplitude is very low, therefore, a longer sequence might be required to combat the low effective SNR. In fact, a low power signal may be mandatory required for the probing signal in order to reduce the interference to other in–service channels but this restriction is not considered here. And again, for SNR $\geq$ 8 dB, a 100–symbol probing sequence provides a satisfactory estimation probability of larger than 0.9 as shown in Fig. 6.14.

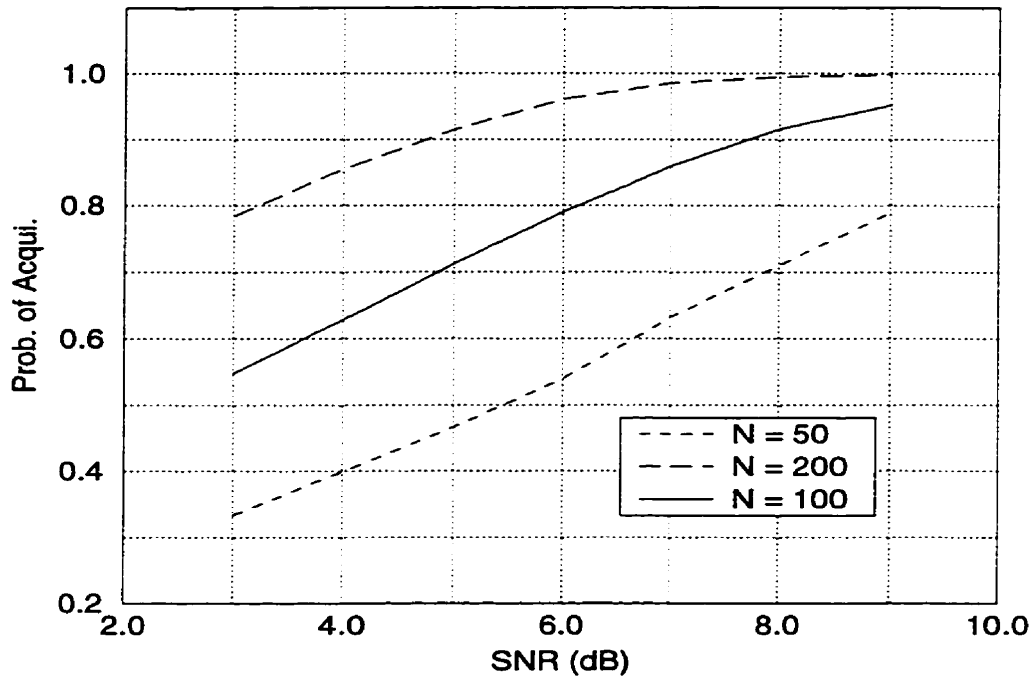

Figure 6.14: Probability of successful Estimates (offset = $T/2$)

6.3 Implementation of the Related Functions

In this section, the implementation of the functional blocks in Fig. 6.1 is explained. Since the downlink and the uplink use different access formats, the satellite downlink and uplink may have different components in their respective transmitters and receivers due to the different requirements from the different pulse shapes used for the transmitted symbols and timing recovery mechanisms used on different links.

6.3.1 Signal Source

The signal source is designed to provide an alternating zero and one sequence or a pseudo random binary sequence with different sequence lengths. The alternative sequence is used in the satellite downlink timing recovery. A short pseudo random sequence is used as a frame synchronization header. Use of frame header is illustrated in Fig. 6.2. The longer random sequence is used to perform the BER test during the system simulation.

The pseudo random sequence is obtained from a linear shift register with feedback.

Both short and long sequence generators are shown in Fig. 6.15 (a) and Fig. 6.15 (b) respectively. The short sequence used for frame synchronization has a sequence period of 15. The long sequence has a period $2^{11} - 1$.

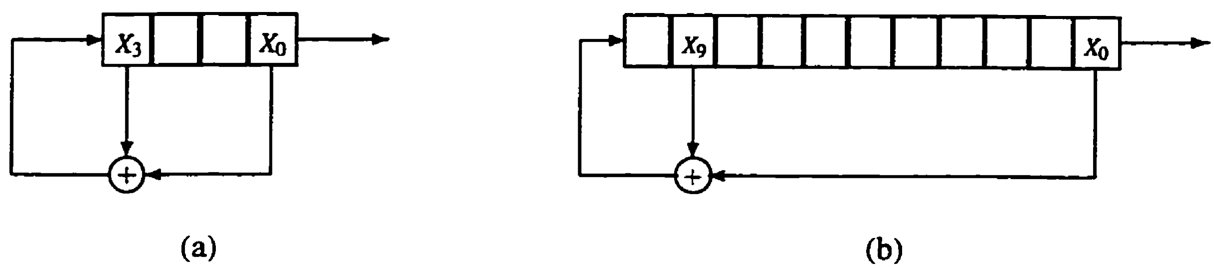

Figure 6.15: Sequence Generators

The update rule for the short sequence is

$$X_3 = X_3 \oplus X_0. \tag{6.4}$$

And the long sequence is updated by

$$X_{10} = X_9 \oplus X_0. \tag{6.5}$$

In both equations above, $\oplus$ is the *exclusive OR* operation. The output is taken from X_0 as shown in Fig. 6.15.

6.3.2 DD–DPLL

The complete PLL model used for computer simulation is given in Fig. 6.16. In this model, the phase detector (PD) is decision–directed, therefore the signal decision is available from the PD. The decision is used to remove the modulating information through feedback. Multiplexers can not perform phase subtraction directly. The phase subtraction is implemented using complex signals through phase rotations which is implemented using

$$\exp(j\phi_d) = \exp(j\phi_1) \times \exp(-j\phi_2) = \exp[j(\phi_1 - \phi_2)]. \tag{6.6}$$

The phase rotation is used to remove the unknown phase offset in the input signal using the local estimate. When the estimate is correct, the bit decision is improved by the coherent

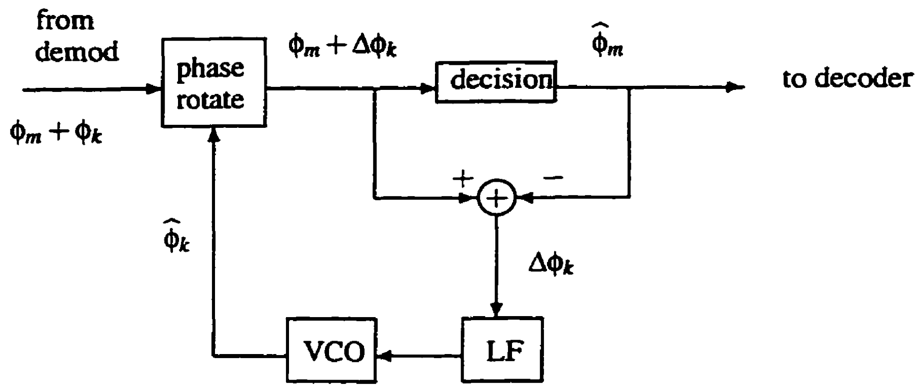

Figure 6.16: Block Diagram of DPLL

detection. The PLL is a second order loop. The loop damping factor is set at 0.707. The natural frequency is set at about $0.01/T$, where T is the symbol duration. This PLL is implemented in a discrete form as had been done in [30].

The loop filter (LF) is a first order IIR filter with transfer function

$$H(s) = \frac{\tau_2}{\tau_1} + \frac{1}{s\tau_1} \tag{6.7}$$

as suggested by Gardner in [83]. It is converted to the discrete form using

$$s = \frac{T}{1 - z^{-1}} \tag{6.8}$$

where T is the sampling period. In the simulation it is the symbol period because the bit decision is made every symbol period. Taking the inverse z–transform, the time domain filter function is obtained as

$$y(n) = \frac{(\tau_2 + T)}{\tau_1} x(n) - \frac{\tau_2}{\tau_1} x(n-1) + y(n-1) \tag{6.9}$$

where τ_1 and τ_2 are the time constants. The loop natural frequency is determined by τ_1. Damping factor is a function of both τ_1 and τ_2 as given in [30]. The loop gain is set to a proper constant. The time domain loop filter structure is shown in Fig. 6.17.

The VCO updates its output phase using the information from the LF. The signal from demultiplexer is phase corrected by the estimated phase, $\widehat{\phi}_k$, before a decision is made.

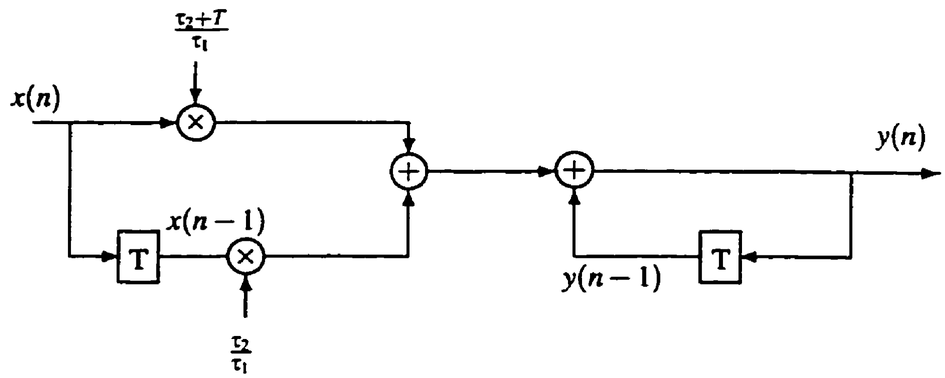

Figure 6.17: Structure of the Digital Loop Filter

Two phases, from before the symbol decision and after the symbol decision, are subtracted to removed the modulation and when this decision is correct, the modulation is removed completely. The resulting error signal is then passed to LF. A new estimate of the unknown phase offset in the incoming signal is then obtained at the output of VCO which follows the phase change in incoming signal. The transient responses to a step phase change and linear phase change will be studied. The steady state performance is characterized by pdf of the output phase of the VCO.

The responses to a step phase change in the input signal is plotted in Fig. 6.18. The input phase is also shown in the figure. In the figure, (a) is the phase plot of the input signal, (b) is the output phase of the VCO, (c) is the output of the phase detector, and (d) is the output of the loop filter. Input signal with phases $\pm\pi/4$ and $\pm 3\pi/4$ are considered having the zero phase offset because these phases represent modulation phases. In Fig. 6.18 (a), the signal phase jump is 0.05 rad and in (b), the VCO output eventually moves to its steady state of 0.05 rad. Outputs from the PD and the LF eventually go to zero. The output jumps of the PD and the LF are responses to the phase jump in the input signal.

The PLL phase synchronization process can be further depicted in a phase plot given in Fig. 6.19 where the phase of input signal changes linearly ($\Delta f T = 0.005$) and the dashed curve represents the output of the VCO. The changing input phase due to a frequency offset

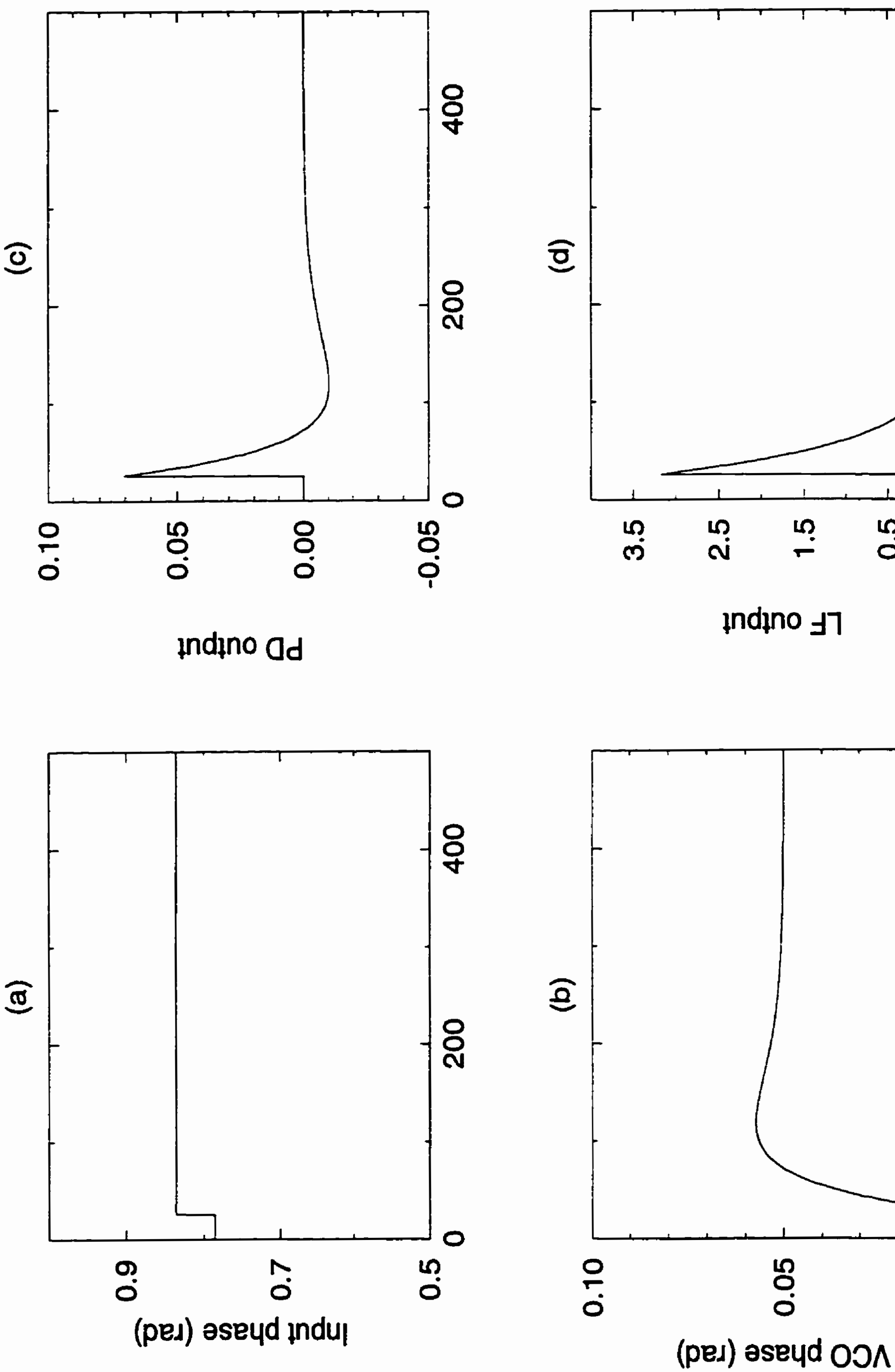

Figure 6.18: PLL Responses to a Step Input Phase Change

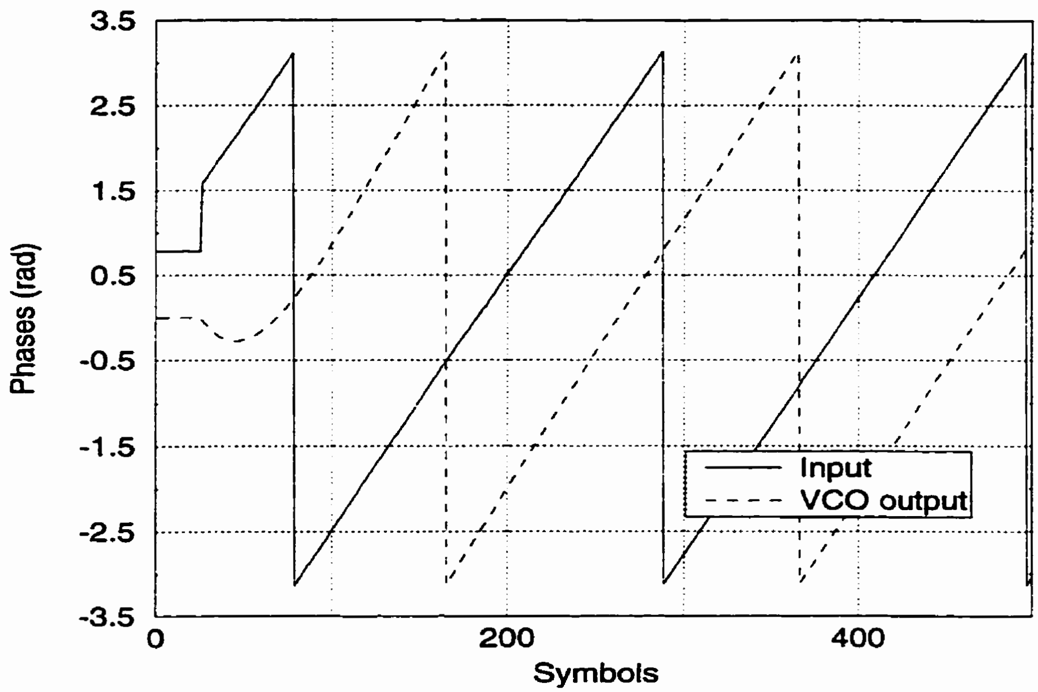

Figure 6.19: Phases of Input Linear Phase Signal and VCO Output

between the input signal and the local oscillator is nicely tracked by this PLL. The transient process takes about 150 symbols. As mentioned before, the recovered local carrier phase may have a fixed offset from the true input signal phase as a result of PLL phase tracking. In this figure, a phase offset of $3\pi/4$ is observed. This phase ambiguity can be removed by using differential encoding in the transmitter.

From these plots, it is clear that the local signal will be locked–in with the input signal after about 150 symbols. In the simulation, 200 symbols are used to allow a complete carrier phase lock–in.

The PLL lock–in process for 2000 symbols is illustrated in Fig. 6.20. In this figure the sine function of the VCO output phase is plotted. Fig. 6.20 (a) is the input sine wave. The input signal represents a constant frequency offset between the carrier of the incoming signal and the local oscillator. This offset is set larger than the case in the simulation in order to show the lock–in process clearly. Fig. 6.20 (b) is the case when noise is not applied while (c) shows the prolonged lock-in time because the effect of noise. This plot is obtained by running the PLL simulation program for $\Delta fT = 0.06$ and SNR $= 10$ dB while

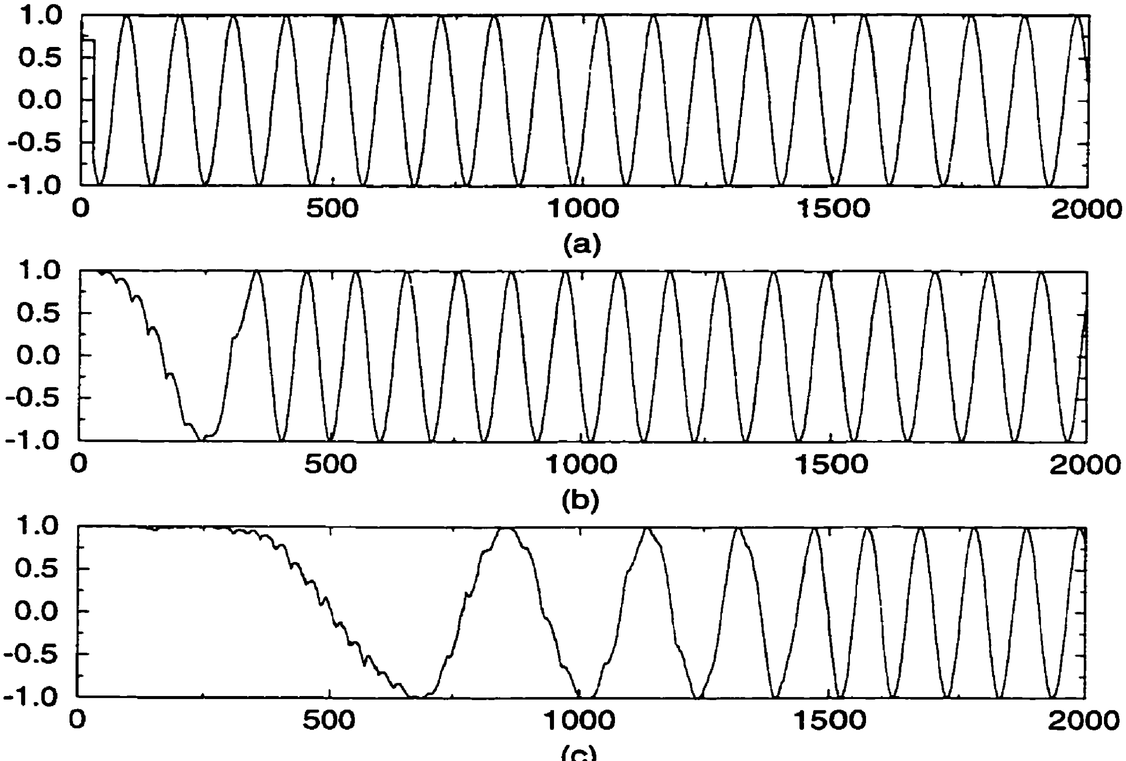

Figure 6.20: PLL Lock–in process

in the system simulation $\Delta fT = 0.01$ is used. In the latter case, the lock–in process takes much less time.

The phase stability is evaluated by its probability distribution. 30000 samples have been taken from the VCO output. The pdf is calculated over $-\pi$, π range for different operating SNRs. The signal mean is computed from this pdf. The variance of the VCO phase is obtained as well. Fig. 6.21 shows the calculation. In this figure two pdfs for SNR = 10 dB and SNR = 5 dB are given. For SNR = 10 dB, the phase variance is 0.00134 rad^2, which corresponds to a standard deviation of 2.1°. This result is comparable to those given in [37]. The pdf is nearly symmetrical and therefore the mean of the phase jitter caused by noise at the loop input is close to zero. Since for $\phi_k > 0.5$ rad the probability is approximately zero, only $\widehat{\phi}_k \leq 0.5$ rad is plotted in Fig. 6.21.

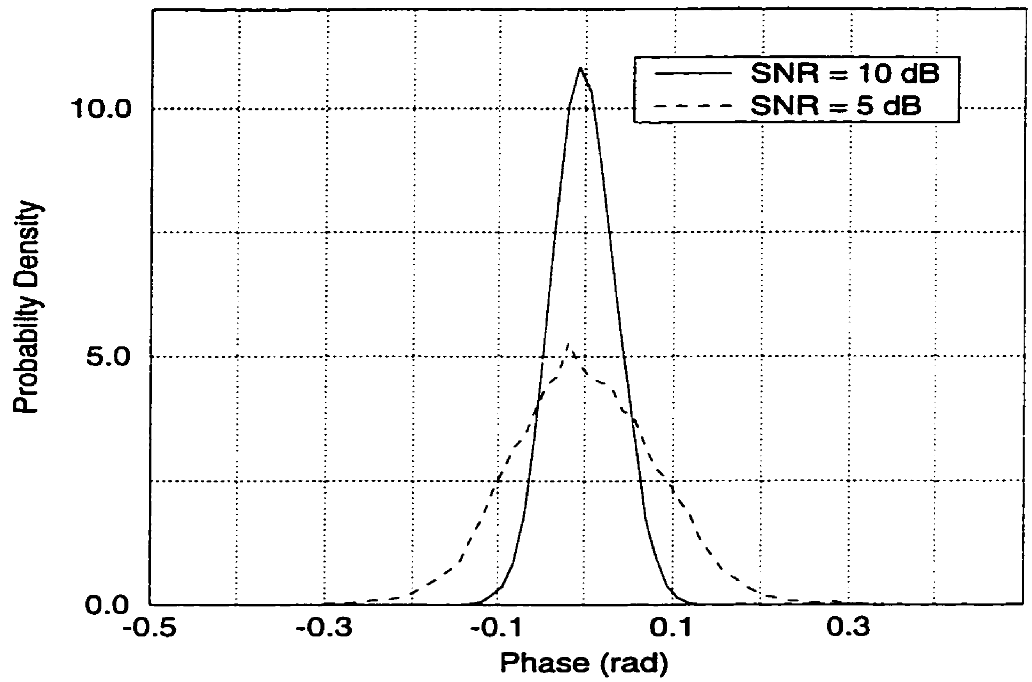

Figure 6.21: Probability Distribution of VCO Output Phase $\widehat{\phi}_k$

6.3.3 Pulse–shaping

The raised–cosine (RC) function with a roll–off factor of 100% is used as the system downlink pulse–shaping transfer function. The magnitude of this transfer function is given as

$$|H(f)| = \begin{cases} 1 & 0 \leq |f| \leq \dfrac{1-\alpha}{2T} \\ \dfrac{1}{2}(1 - \sin\dfrac{\pi T}{\alpha}(|f| - \dfrac{1}{2T})) & \dfrac{1-\alpha}{2T} < |f| \leq \dfrac{1+\alpha}{2T} \\ 0. & \end{cases} \tag{6.10}$$

where α is the roll–off factor, $0 \leq \alpha \leq 1$. The impulse response is split into transmitter and receiver filters. To make the receiver filter matches the pulse shape of incoming signal, square root of the RC pulse shape is used in both the transmitter pulse–shaping filter and the receiver matched filter. The overall raised–cosine shape is used because Gardner's timing recovery algorithm [29] works best when baseband signal at the receiver detector is in the raised–cosine shape. The Gardner's timing recovery algorithm will be used later for downlink timing recovery. The uplink pulse shape is rectangular because windowing is used generally in the on–board processor.

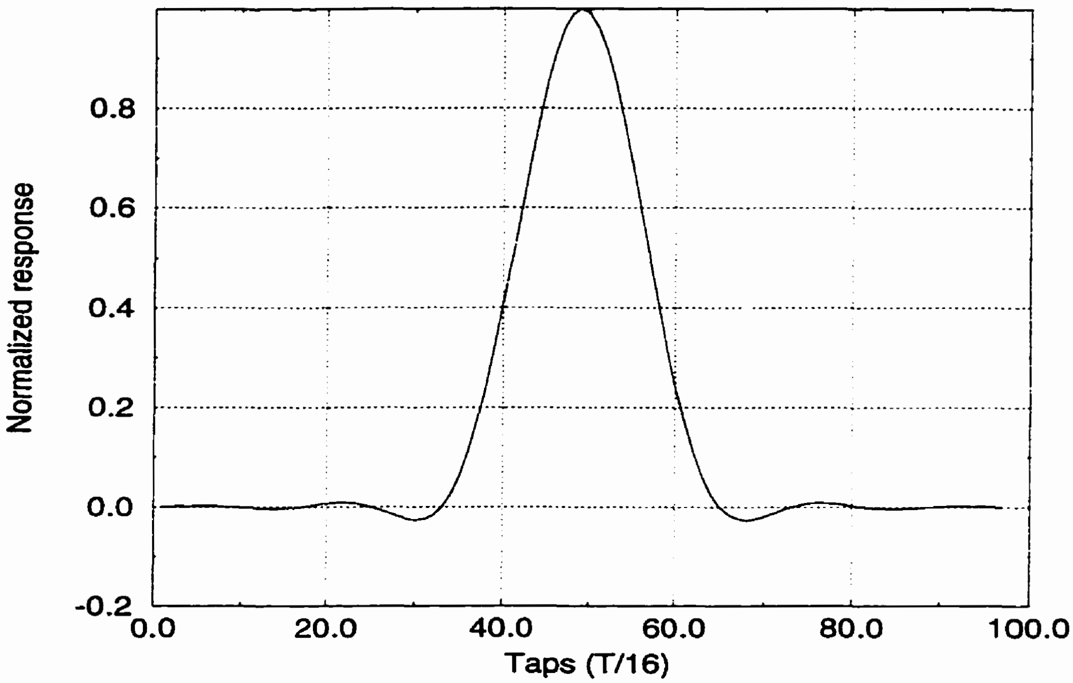

Figure 6.22: Impulse Response of 97-tap $\sqrt{RC}$ Filter

The FIR filter is realized using 97 tap coefficients. The signal is sampled at 16 samples per T and therefore, the filter finite impulse response lasts for 6 symbols. The impulse response of this square–root RC filter is plotted in Fig. 6.22. Less taps would be used in an real application.

A random baseband signal obtained from the output of the pulse–shaping filter is given in Fig. 6.23. The dashed line shows the input signal and a 48 taps (3T) delay due to pulse shaping can be observed. The received signal passed to the receiver matched filter is delayed by another 48 taps and a total of 6–symbol delay is shown clearly in the plot. This time relationship must be taken into account when simulation programs are written.

6.3.4 Downlink Timing Recovery

The downlink clock frequency is recovered as the master clock. The algorithm used to recover this master clock is immune from the phase offset in the carrier recovery process [29] and thus, the timing can be recovered before the carrier phase is recovered perfectly.

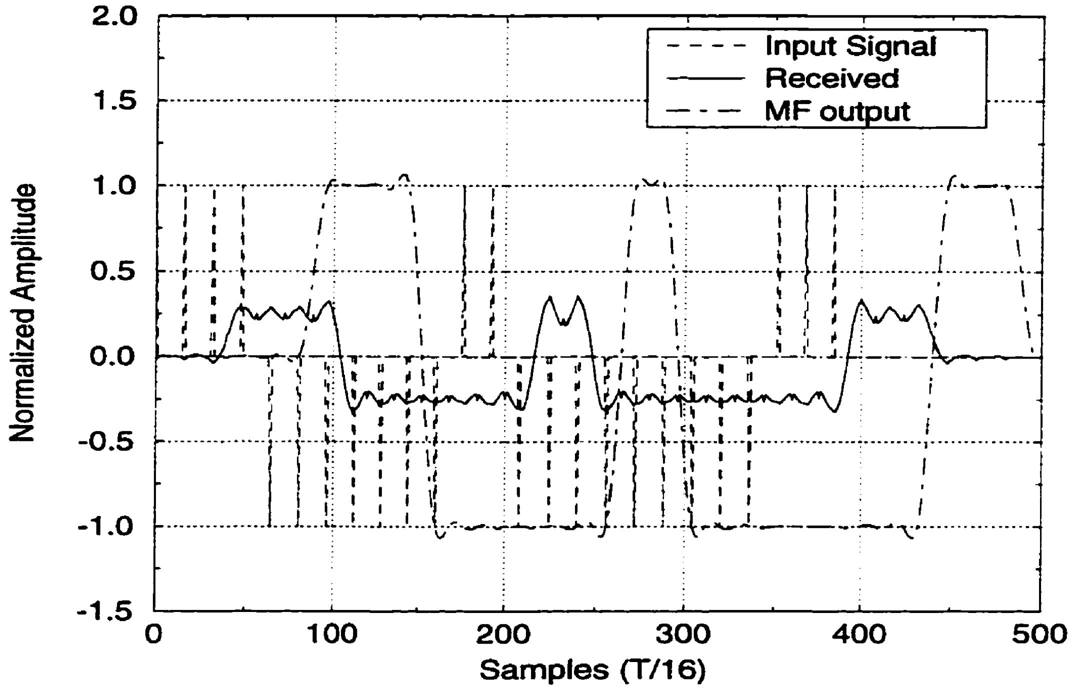

Figure 6.23: Baseband Signals with Square–root RC Pulse Shaping

This feature allows the use of discrete PLL for the carrier recovery.

The timing error is detected using [29]

$$e(n) = \Re[r(n-\frac{1}{2})]\Re[r(n)-r(n-1)] + \Im[r(n-\frac{1}{2})]\Im[r(n)-r(n-1)]. \qquad (6.11)$$

In Eqn. (6.11), $r(n)$ is a complex signal from the matched filter. $n-\frac{1}{2}$ represents the mid–pulse sampling time and n and $n-1$ represent two consecutive symbol detection sampling instants. $\Re[\cdot]$ and $\Im[\cdot]$ take the real and imaginary part of the signal $r(n)$ respectively. $e(n)$ is the error signal from this timing detector. The characteristic of this timing error detector is obtained by feeding data with fixed offset to the detector. The output of the detector is shown in Fig. 6.24. The positive offset in the plot means the local timing is leading the correct sampling time, therefore, a negative voltage is generated to move the local clock phase backward. And vice versa, negative offset leads to a positive error signal. The stable operation region, from the plot, is between $[-T/4, T/4]$ as illustrated in [29]. The operation gives a real number. This timing error signal is filtered by an IIR filter described by

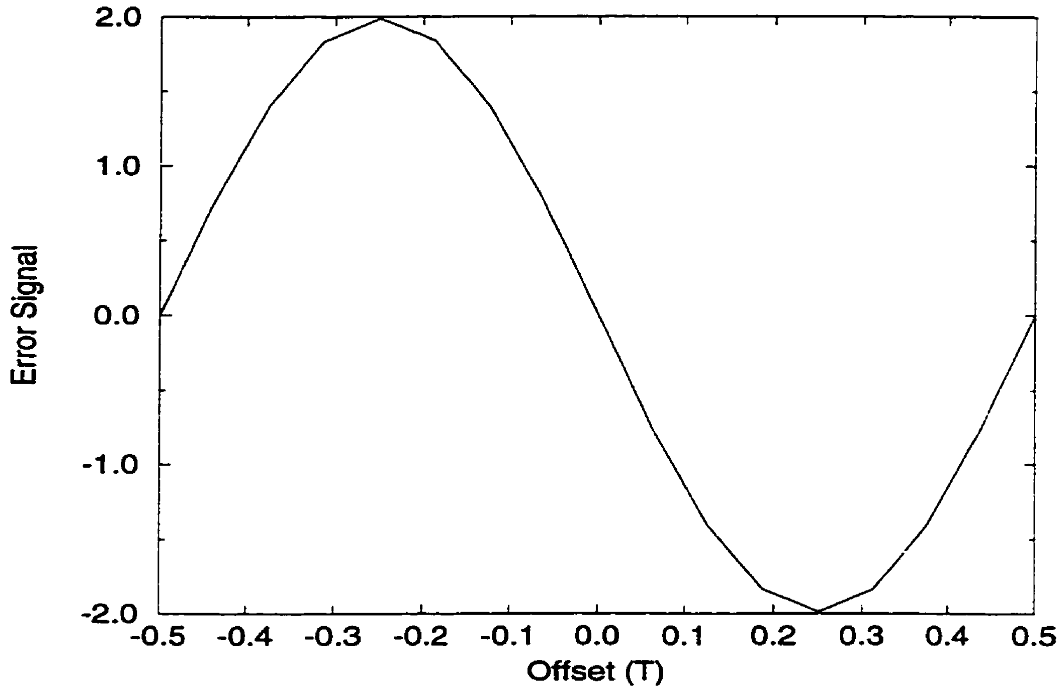

Figure 6.24: Characteristic of Timing Error Detector (S–curve)

$$y(n) = ax(n) + by(n-1) \tag{6.12}$$

where $x(n)$ is the input to the filter and $y(n)$ is the output of the filter. Parameters a and b characterize the IIR loop filter. Unity gain can be obtained by setting $a+b=1$. Increasing a increases the filter BW. Wider bandwidth provides quicker response to the error present in the timing but it also makes the detector more susceptible to the noise in the signal. In the simulation, $a = 0.05$ is used. The filter state is reset after each correction. This is necessary since after each correction, the timing status is changed and the old status kept in the filter does not represent the current timing information. A threshold is used to compare with the accumulated error signals from the timing error detector given in [29]. The threshold helps reducing unnecessary correction of the timing of symbol samples [74]. The threshold used in the simulation is 30 percent of the peak signal amplitude as suggested in [74]. The error signal is plotted in Fig. 6.25 with the noise generator being turned off for better illustration. It is easily seen that the error signal builds up to the threshold in the plot, then the timing is corrected and the filter status is cleared, which produces a drop in the error

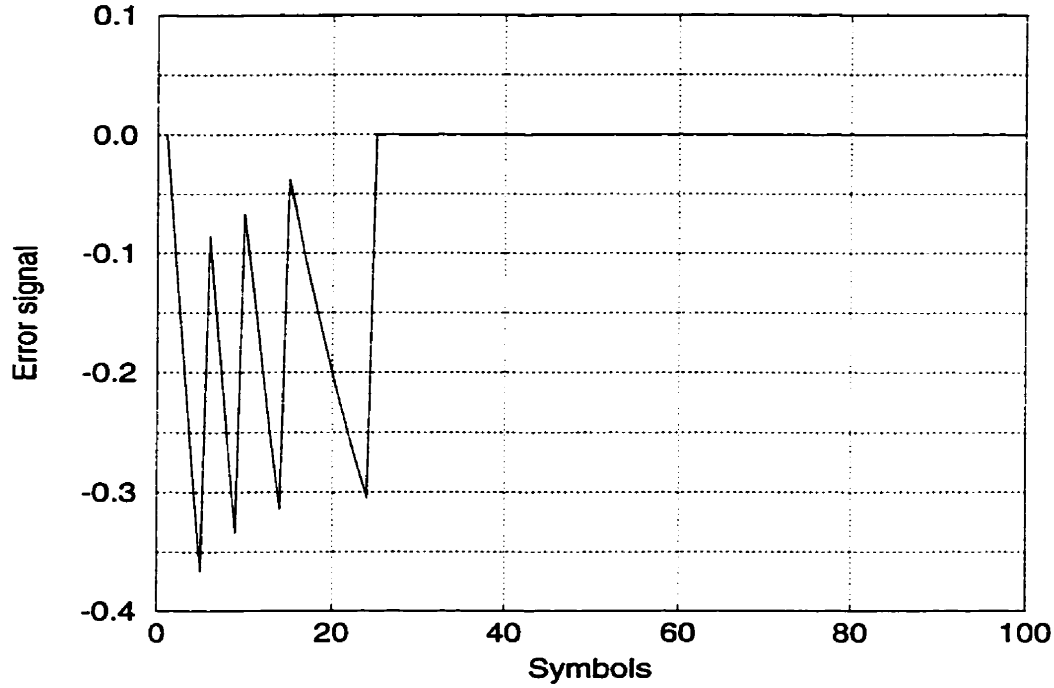

Figure 6.25: Error Signal from Timing Loop Filter

signal amplitude. The peaks of the error signal corresponds to a one–step correction when $|e(n)|$ is greater than the threshold. Otherwise, no correction is made.

In the simulation, the initial sampling position (timing phase) is arbitrarily set to an offset of $T/4$ (a 4–sample advance from the correct timing phase). In Fig. 6.26, four correcting pulses appear with negative signs where each of the pulses imply that the timing point should be retarded by one–sample time. The fourth correcting signal is not generated as quickly as the previous three occur as smaller timing offsets will be corrected slower than the larger timing offset. The error signal amplitude is smaller when timing is closer to the correct one and therefore a longer integration time is required to make error signal larger than the threshold.

6.3.5 Differential Encoder/Decoder

The differential encoder and decoder are used to combat the phase ambiguity of the recovered carrier phase reference. The source information is encoded before being fed into the

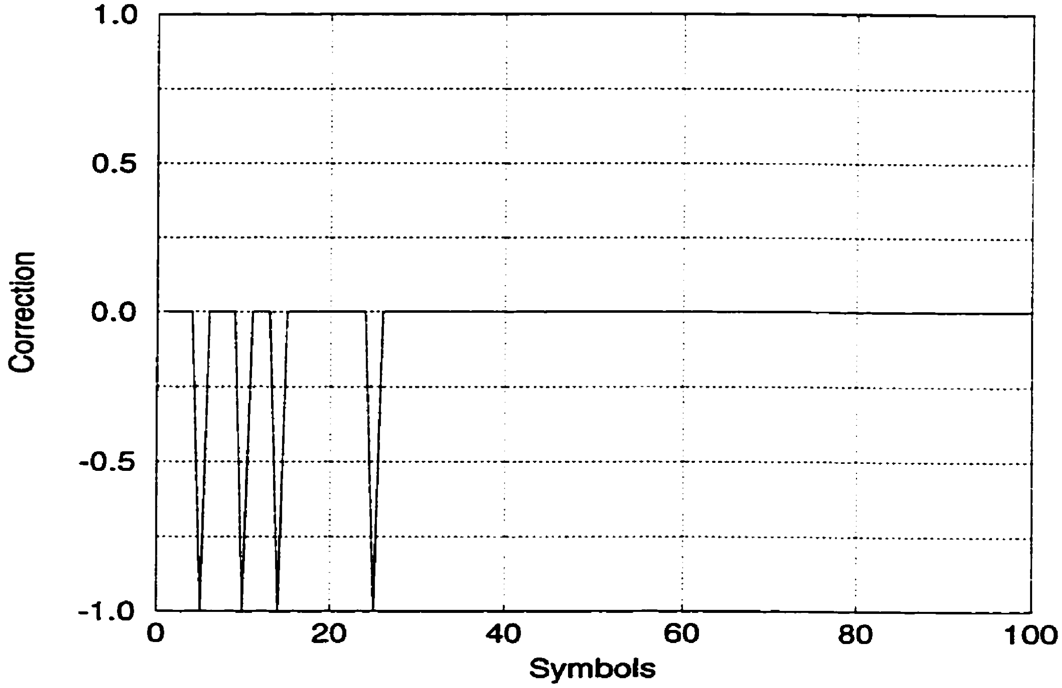

Figure 6.26: Correction Signal

modulator using

$$\phi_{m+1} = (\phi_m + \phi_{in}) \bmod 2\pi. \tag{6.13}$$

Here ϕ_{in} is the phase of source signal and ϕ_m is the mth modulation signal phase. Since the source signal phase is represented by $\pm\pi/4$ and $\pm 3\pi/4$, a phase shift of $-\pi/4$ is used to rotate it to the $(0, \pm\pi/2, \pi)$ constellation for proper encoding. The output of this encoder uses the $(\pm\pi/4, \pm 3\pi/4)$ constellation by rotating the encoded phase by $\pi/4$.

The differential decoder inverts the encoding process. The source information is recovered using

$$\widehat{\phi_{in}} = (\phi_{m+1} - \phi_m) \bmod 2\pi. \tag{6.14}$$

6.3.6 Frame Synchronization

The frame header is generated by a pseudo random sequence generator with a sequence length of 15 bits. The length of the frame header guarantees a non–correlation with other possible sequences at high probability of $1-(0.5)^{15}$ when assuming an *iid* signal source packaged in the meesage body of Fig. 6.2. This header is inserted to the start of each downlink frame as shown in Fig. 6.2. The timing error information is transmitted in the downlink frame. To extract this information, the ground terminal tries to determine the location of a frame header using the correlation process explained below. Once this header is located, the terminal can extract the uplink timing error information from a pre-determined block in the frame.

A local copy of the header sequence is correlated with the detected bit stream using

$$X_{corr}(\tau) = \sum_{i=0}^{14} l(i)\, r(i-\tau) \tag{6.15}$$

where $l(i)$ is the local sequence, $r(i)$ is the received bit stream and $X_{corr}(\tau)$ is the cross–correlation between the two signals. If a high correlation is achieved, then *frame–sync* is declared. In the simulation, a threshold is set to tolerate possible erroneous bit decisions. For a 15–bit sequence, when all bits are recovered correctly, the correlation output is 15. The threshold is set at 11, which means that two error bits are allowed before the frame header is missed in the detection process. This value corresponds to an average bit error rate of 0.133. Such a high bit error rate represents a low SNR of -2 dB. The normal operating SNR in this simulation is in the range of 5 dB to 10 dB.

6.3.7 MCD and Magnitude Estimator

Now the MCD is included into the uplink delay estimation algorithm presented in section 5.3. The multicarrier demodulator is implemented using

$$F(t) = \int_0^T f(\tau) \exp(-j\mu t\tau)\, d\tau \tag{6.16}$$

which produce the desired CFT at time t. Here $f(\tau)$ is the input FDMA signal from a ground terminal. Integral $F(t)$ is a complex signal.

The estimator takes the real and the imaginary parts of $F(t)$ in (6.16) respectively and uses the on–board master clock as a timing signal. The uplink delay estimation algorithm was introduced in section 5.2.2 and was simulated in section 6.2. In the simulation, it starts working after the downlink clock and carrier phase are recovered.

The whole algorithm is briefly reviewed here. The uplink transmission is controlled by the recovered clock and the estimated uplink signal amplitude information is transmitted to the ground terminals via the satellite downlink. The uplink timing error is calculated in the ground terminal. N samples are taken from MCD and the averages of the real part and the imaginary part are obtained separately. This process produces the maximum likelihood estimations of the in–phase and the quadrature components. Two MLEs, independent of each other, are combined using

$$r = \sqrt{x^2 + y^2}$$

as was given in (5.40) to remove the phase information. The magnitude estimate that uses this method is plotted in Fig. 6.27 as a function of the sample size. In the same plot, the signal amplitude estimated directly using the magnitude of MCD output is given as a dotted line. A bias is observed from the plot for this direct estimation of the uplink signal power. Any unknown bias in the estimate will degrade the estimation accuracy. The bias is minimized by taking the in–phase and quadrature ML estimate and then combine them to get the amplitude estimate. A quantized version of estimation from the I and the Q channels is also shown in Fig. 6.27. As concluded before in section 6.2, a 100–symbol preamble is enough to produce a stable timing estimate. In this simulation SNR $=$ 10 dB was used.

The probability distribution of the estimate displayed in Fig. 6.28 is obtained using the simulation program involving 30000 symbols. The timing offset in running the simulation is set at $0.375T$ and, also, SNR $=$ 10 dB. The true signal amplitude without the effect of noise should be $0.25A$, where A is the designed signal amplitude. The results shown in Fig. 6.28 is easily recognized as the Rician pdf. The theoretical pdf given in the plot uses

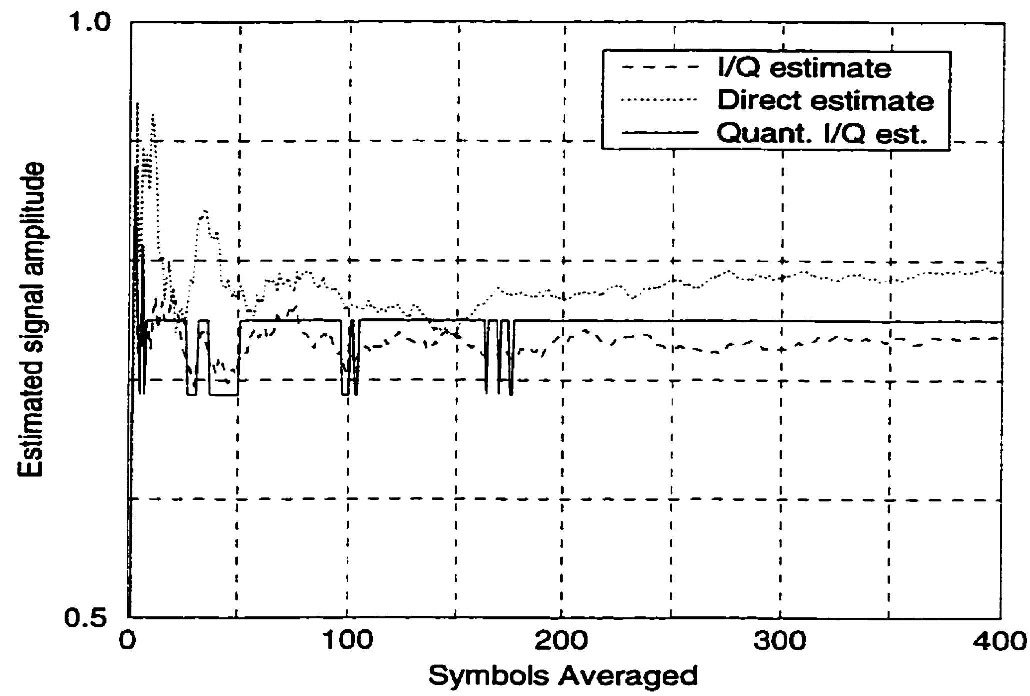

Figure 6.27: Estimated Magnitude as a Function of Sampling Size

(5.41) with mean $0.25A$ and σ be the function of SNR. It is in good conformity with the simulation. The separate I and Q channel estimation must be used to avoid the problem of biased estimation which is clearly shown by the dotted line in Fig. 6.27.

In the next section, all related functional blocks are put together in order to examine the dynamic performance of the delay estimation algorithm.

6.4 System Simulation

The system initialization procedure is introduced in this section. The interference to other in–operation users due to incorrect delay estimation error is examined. A complete system simulation with downlink and uplink driven by a common clock follows the separate simulations of uplink and downlink. The system performance will be evaluated in terms of the BER. The effect of downlink operating SNR, which affects the stability of recovered downlink clock, on the uplink delay estimate is also tested. The result will be given as a probability of correct estimate of the uplink timing offset as a function of uplink SNR with

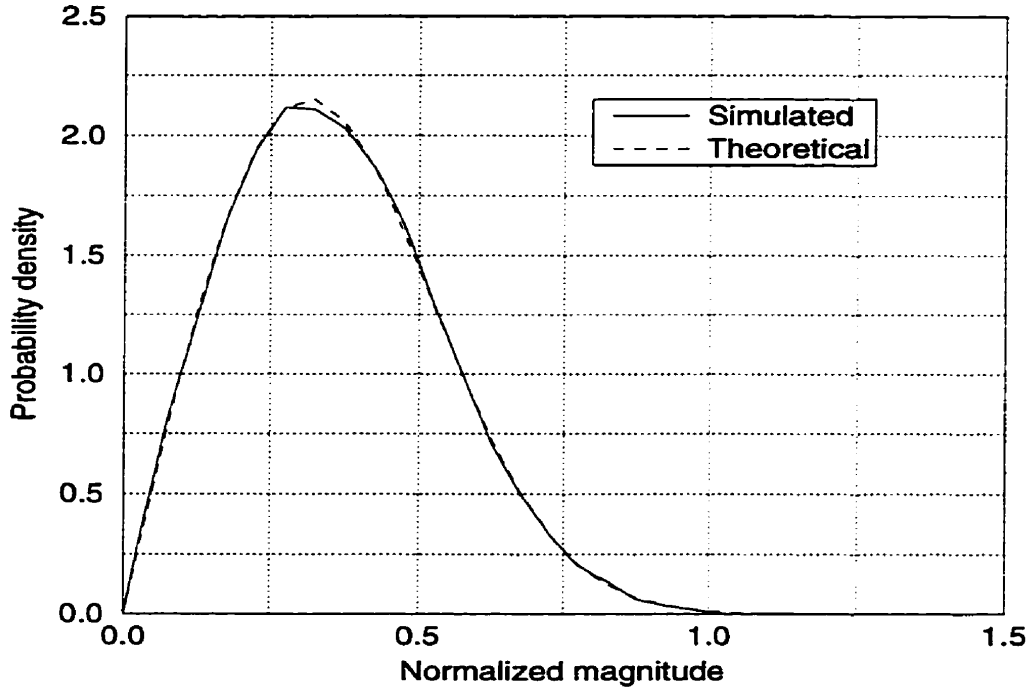

Figure 6.28: PDF of Magnitude at sampling Time

downlink SNR as parameter.

6.4.1 System Initialization

6.4.1.1 Initialization Procedure

The system initialization procedure is shown in Fig. 6.29. Only the clock signal flows are shown in this flow chart. The on–board frame–forming process of the downlink is not shown explicitly. Iterative acquisition using a shorter sequence is not considered as a valid approach here since the time savings from a shorter sequence can not compensate for the large propagation delay between the satellite and the ground terminal since multiple probes are required if a shorter probe sequence is used.

Referring to Fig. 6.29, the flow chart for the uplink time delay estimation algorithm is described. The process starts from recovering the satellite clock and carrier of the downlink. During this phase, no specific signal is required since the downlink stream is driven by the master clock on–board the satellite. The ground terminal first detects power from

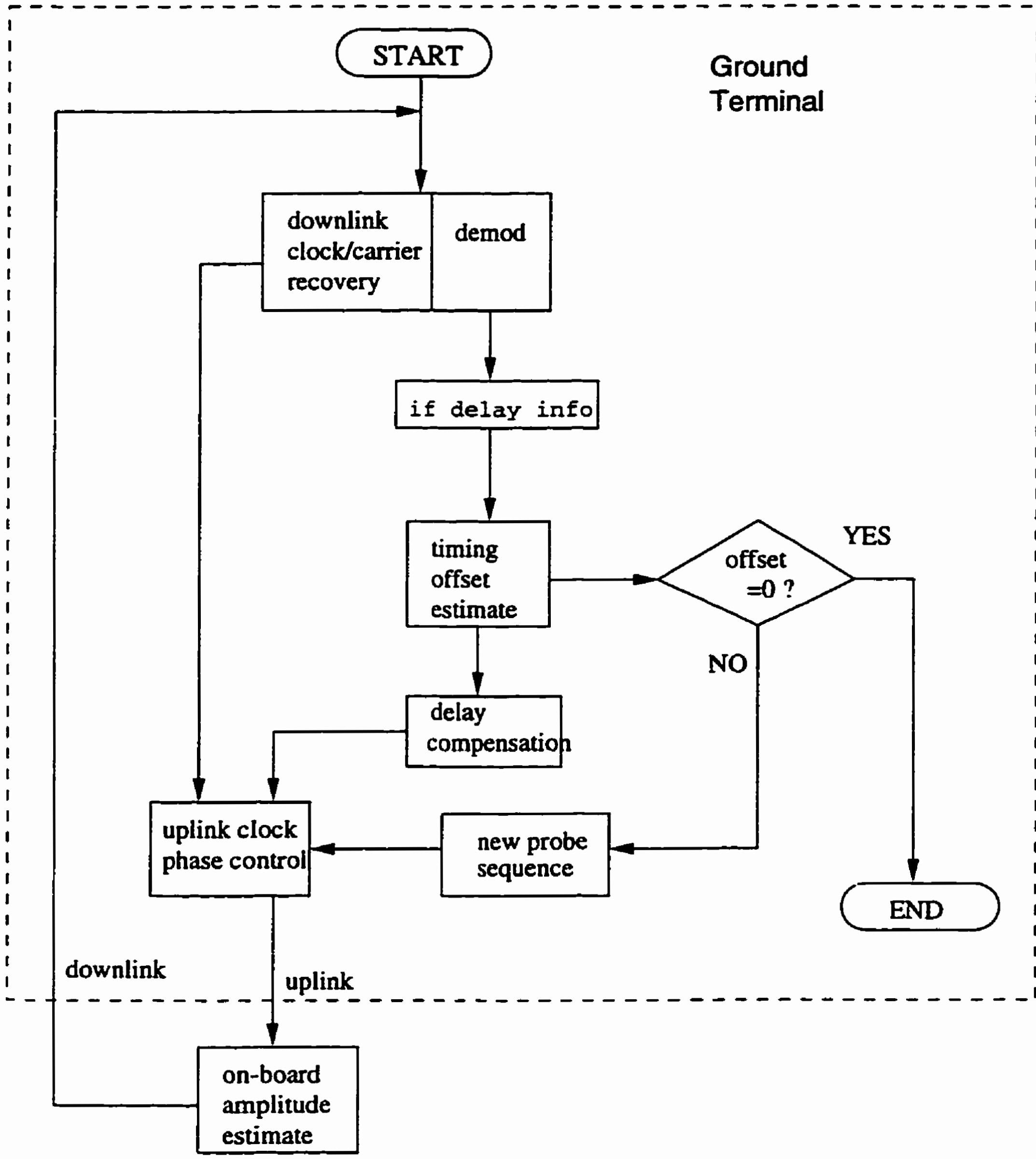

Figure 6.29: Initialization Flow Chart

the downlink for possible initialization. After acquiring the downlink clock, the ground terminal sends a probe sequence which is clocked by recovered downlink clock and the clock phase is compensated according to an estimated uplink propagation delay. The process is marked by `timing offset estimate` and `delay compensation` in Fig. 6.29. The `timing offset estimate` part converts the estimated magnitude information to the timing offset estimate using a table lookup. If a zero offset is found, then the initialization process is terminated. Otherwise, a new probe sequence is transmitted based on the new estimated delay and the uplink timing offset is estimated again. The received signal amplitude for the uplink probing sequence is estimated on–board the satellite. The estimated amplitude is transmitted to the ground terminal in quantized form. The `delay compensation` stores the compensating information for the delay estimate.

This kind of system initialization process can be described by a *geometric random variable* X. This is a *first time of success* problem. Such a trial has two outcomes, *success* and *failure*. Let the probability of success in a trial be p, then the process has a *success* outcome in the n–th trial is given by

$$P(X=n) = (1-p)^{n-1}\,p \qquad n \geq 1 \tag{6.17}$$

where p is the probability of getting a success in one trial and n the number of trials performed. The expected value of the random variable$X$ is

$$E[X] = \frac{1}{p}. \tag{6.18}$$

This expected value is the average number of trials to get the first success. From Fig. 6.10, the probability of *success in one trial* is larger than $p = 0.98$ for a 100–symbol probing sequence with a 10 dB operating SNR. Therefore, almost all estimates are correctly obtained with one estimate. From (6.17), the probability of success in more than one would be 0.02. In the simulation, it is rare to find an incorrect estimate of the uplink signal magnitude when the SNR is a constant. Theoretically, since the success of the estimate is confirmed through one more round of the estimation process, there exists the probability of missing the correct estimate, but this probability is $p \times (1-p)$. With $p = 0.98$, one gets the probability of the incorrect confirmation to be 0.0196. Therefore, the risk of missing a correct estimate is very low. The risk increases when the SNR becomes lower.

The complete initialization procedure is listed as follow:

1. Receive the downlink signal and recover the master clock. The uplink timing offset is determined by the ground terminal.

2. Transmit the uplink probe signal controlled by the recovered master clock.

3. Process the uplink signal on–board to obtain the magnitude estimate.

4. Transmit the quantized estimated uplink magnitude information in the proper downlink channel.

5. The ground terminal determines the amount of the uplink delay and compensates this delay by adjusting the transmission time.

6. Send a new probing sequence based on the the compensated uplink clock phase. Check uplink timing offset from step 1. If it is zero, synchronization is declared.

6.4.1.2 Interference During Initialization

The unsynchronized new user accessing the system may cause inter–channel interference (ICI) because the output of the MCD produced from a non–synchronous uplink has a non–zero value at the other channels' sampling instant [35]. The amount of the interference on different channels is characterized in [35]. This ICI is a function of the timing offset. The maximum ICI is about 15 dB lower than the normal signal amplitude for the adjacent channels. In Fig. 6.30, four FDMA channels (numbered 1 to 4) are processed by the on–board processor, without windowing on the inputs and the phase change from previous symbol is $\pi/2$ for this channel. The third channel suffers a fixed timing offset of $0.15T$. The situation for correct timing for all channels is also given in this plot for easy comparison. In this figure, the detected signal magnitude is normalized to one when timing is correct. The sampling instants are in multiple integers of 1.055 according to the parameters used in the simulation. A 20% signal amplitude drop for the third channel can be observed. This

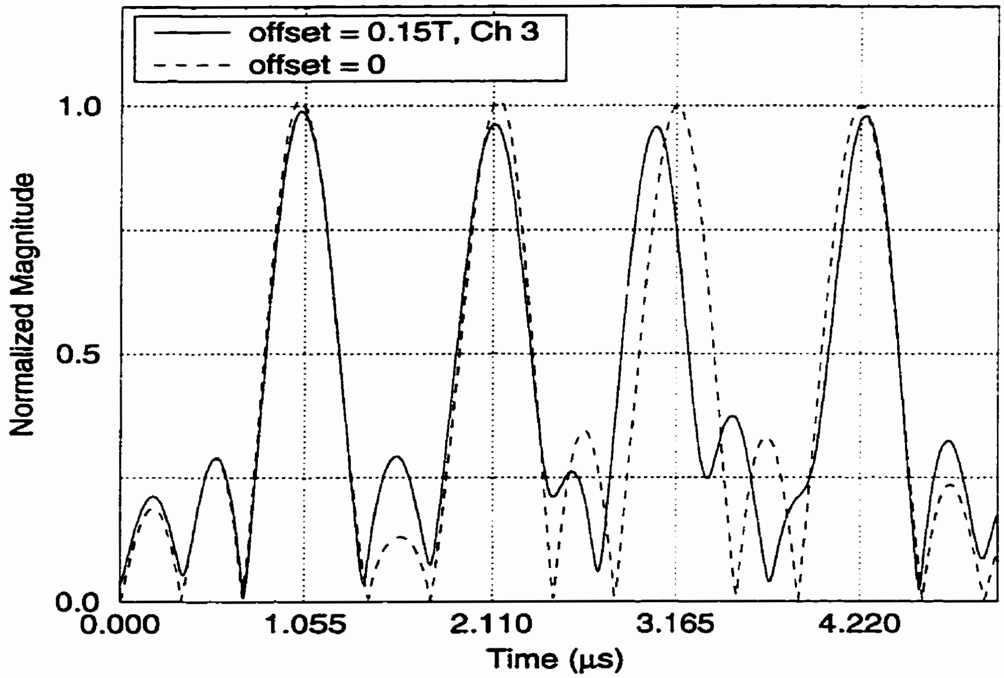

Figure 6.30: ICI caused by Timing Offset

ICI is a function of the timing offset, the number of active channels, and the phase changes, therefore, at some point it is large enough to cause to interference to other users [35].

It is shown that the ICI can be reduced by applying a windowing function on the input signal in time domain before it is processed by MCD in [35]. In the system simulation, a non–windowed MCD is used, for a simpler timing–magnitude relationship. In the real system, a windowing function should be used at the input to the MCD in order to minimize the interference to the other users.

6.4.2 Downlink Simulation

The simulation model of the downlink transmitter/receiver pair as shown in Fig. 6.1 consists of a signal source, a pulse shaping filter, a noise generator, the carrier phase tracking function, the timing tracking function, the differential encoder/decoder, the matched filter, and the decision circuit. It is studied through the BER performance. The downlink simulation and subsequent uplink simulation in section 6.4.3 serves the purpose of testing the

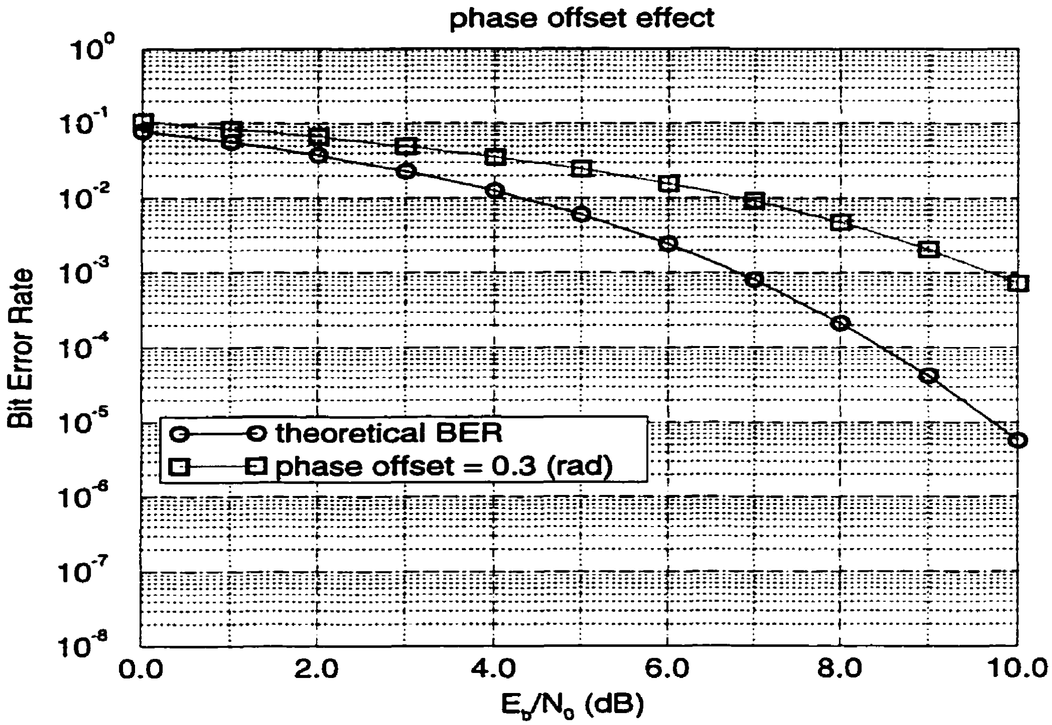

Figure 6.31: BER with Constant Phase Offset

different parts of an integrated system for the synchronization of a terminal to a processing satellite receiver. Results show that the simulated BER, when phase and timing tracking are used, is almost identical to the BER calculated from the theoretical equation in [38]. Also studied here are the degradation of the BERs by a constant phase or timing offset. In Fig. 6.31, two BER curves are the optimal BER of a QPSK receiver and the BER with a phase offset of 17.2°. Perfect timing recovery is assumed in this plot and a differential encoder/decoder is not used. The encoder/decoder is not used because the purpose of this simulation is to examine the effect of carrier offset on the optimal QPSK receiver without the effect of a differential encoder/decoder. A 3 dB loss of SNR for $P_e = 10^{-3}$ is observed. A fixed timing offset also causes a SNR penalty. The result for fixed timing offset is given in Fig. 6.32. In this plot, the transmission is not differentially encoded and a perfectly recovered carrier is provided. The length of the testing sequence is selected in such a way that it guarantees the resulting BER within less than $0.2P_e$ with 95% certainty where the theoretical P_e is taken from the coherent detection scheme with a matched filter [22, 82].

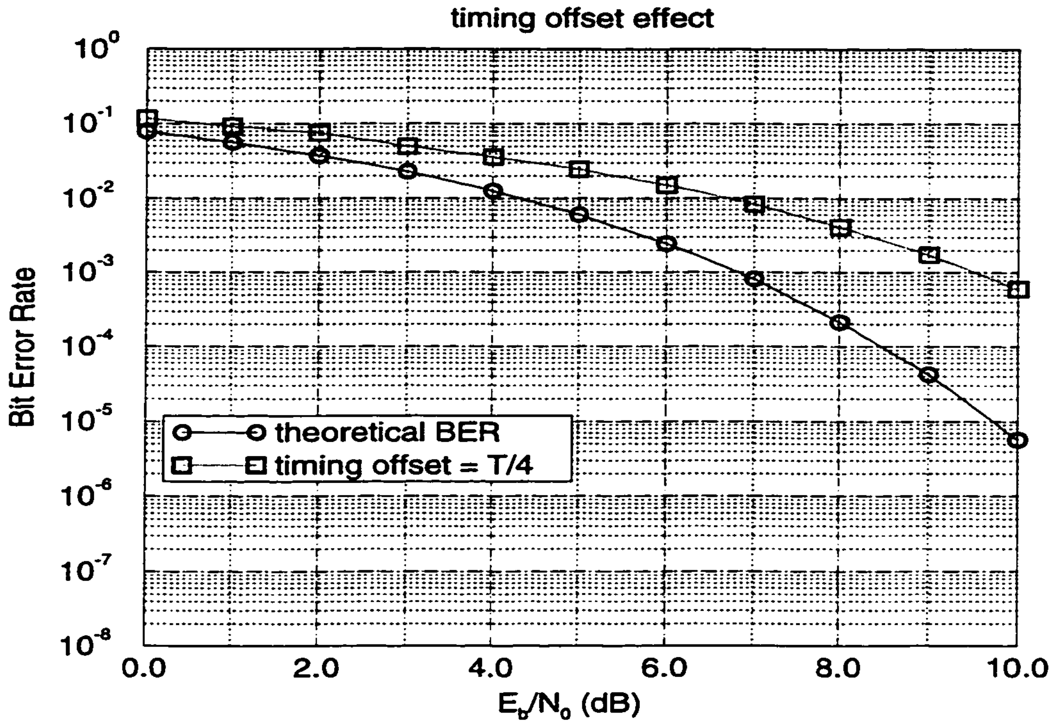

Figure 6.32: BER with Constant Timing Offset

Coherent detection is used in the ground terminal receiver because of its SNR gain over the differential detection. The carrier phase coherence is obtained by using a second order digital PLL. Differentially encoded QPSK is used to combat the phase ambiguity introduced by the PLL. If the BER of optimal receiver in AWGN is P_e, then considering only the effect of two consecutive errors on the differential decode process, the differentially decoded BER, P_{diff}, is given approximately by

$$P_{\text{diff}} = 2P_e - P_e^2. \tag{6.19}$$

The first term on the right side of (6.19) shows the effect of error propagation from the differential decoding process and the second term shows the effect of the errors on the erroneous signal. The usefulness of this approximate expression will be discussed shortly. The increase of the BER implies a loss of approximately 0.4 dB at an SNR = 8 dB associated with this detection scheme as shown in Fig. 6.33. This figure has three curves, the optimal BER is given as a baseline. The simulation is very close to the calculation using

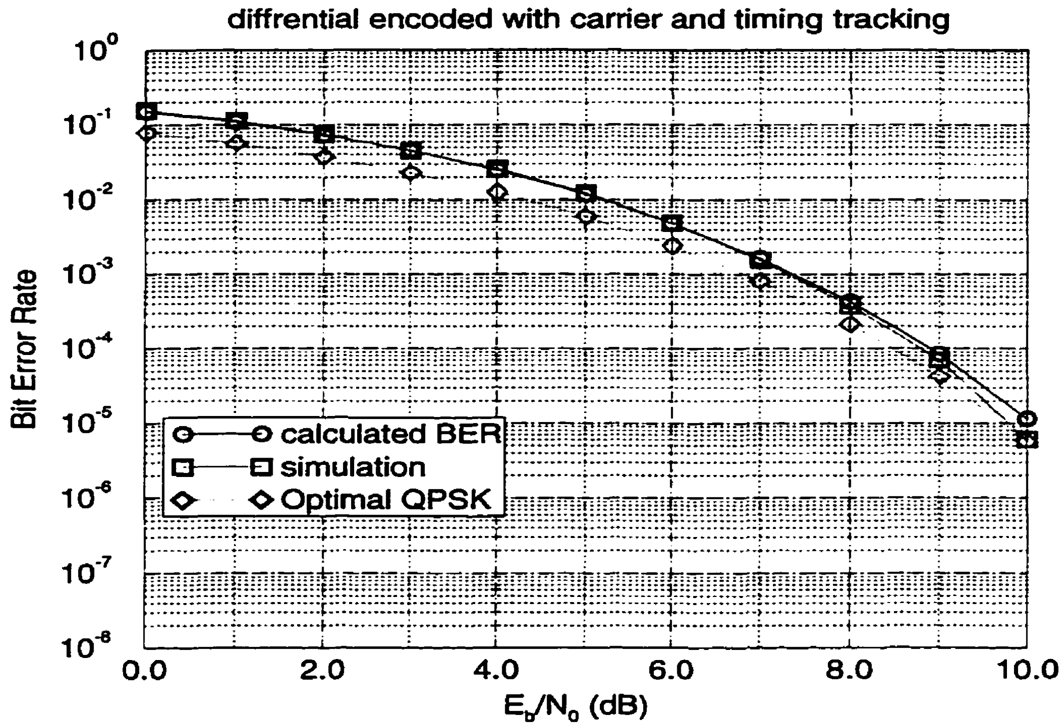

Figure 6.33: Operational BER in Downlink

(6.19). The conformity in the simulated BER with the calculation shows that simulation programs, especially the PLL and the timing recovery circuits are working as expected in this integrated downlink.

6.4.3 Uplink Simulation

The major difference of the uplink receiver from the downlink receiver is the use of a multicarrier demodulator (MCD). The matched filter on the downlink is replaced by a SAW based MCD to demodulate multiple channels at one time. Since the receiver clock phase, *i.e.* the sampling time, is fixed for this type of receiver, the transmitter must adjust its transmitting clock phase in order to have synchronized symbol timing at the receiver.

The simulated uplink including both the transmitter of the ground terminal and the receiver on–board the satellite consists of a signal source generator, a channel noise generator, a complex phase rotator, an MCD, and a decision–directed PLL. The channel introduces

AWGN to the signal. The phase rotator, which can be placed either at the transmitter end or the receiver end, emulates the unknown phase offset. Any phase offset must be applied before the signal enters the MCD in order to let the offset take effect on all the input signals. The simulated uplink channel is linear and the signal applied to MCD is not windowed.

The SNR loss caused by the fixed timing offset can be obtained from Fig. 6.34 for different amounts of offset. The calculated BER shows the best achievable BER with differential encoding. The BER with a $T/16$ offset of the timing phase shows about 0.5 dB SNR penalty for BER $= 10^{-4}$. From [35], only 0.2 dB of SNR penalty is expected when windowing function is used at the receiver, therefore, the other 0.3 dB of SNR penalty should be attributed to the non–windowing receiving of the uplink signal and imperfect carrier phase recovery. This penalty reflects the reduction of the effective SNR because of the timing offset. Timing offsets less than $T/16$ are regarded as `no-offset` due to the fact that our simulation has a minimum time resolution of $T/16$. From (4.18), not only the modulating phase but also an un–wanted phase will present at the output of the MCD at the sampling time because of a timing offset in the incoming signal. Therefore, phase tracking is required for proper demodulation of the uplink signals.

The fixed phase offset in the uplink carrier is tracked by a PLL following the MCD. The carrier frequency offset shifts the signal peak because it adds extra frequency to the designed operation frequency. From (3.1), if $\Delta\omega$ is added to ω, then a $\Delta t = \Delta\omega/\mu$ offset in time from designed signal peak is expected. The unwanted frequency offset can not be tracked by the subsequent PLL because the MCD does not pass this frequency information in the way the conventional receivers do. The carrier frequency offset results in the degradation of the BER performance because the frequency offset leads to a lower SNR and larger phase variance. The frequency synchronization is ensured by letting the uplink carrier lock to the recovered downlink carrier. The residual frequency offset will not cause any serious performance degradation when the uplink signal is frequency synchronized. In the simulation, the uplink carrier frequency is assumed perfectly synchronized to the

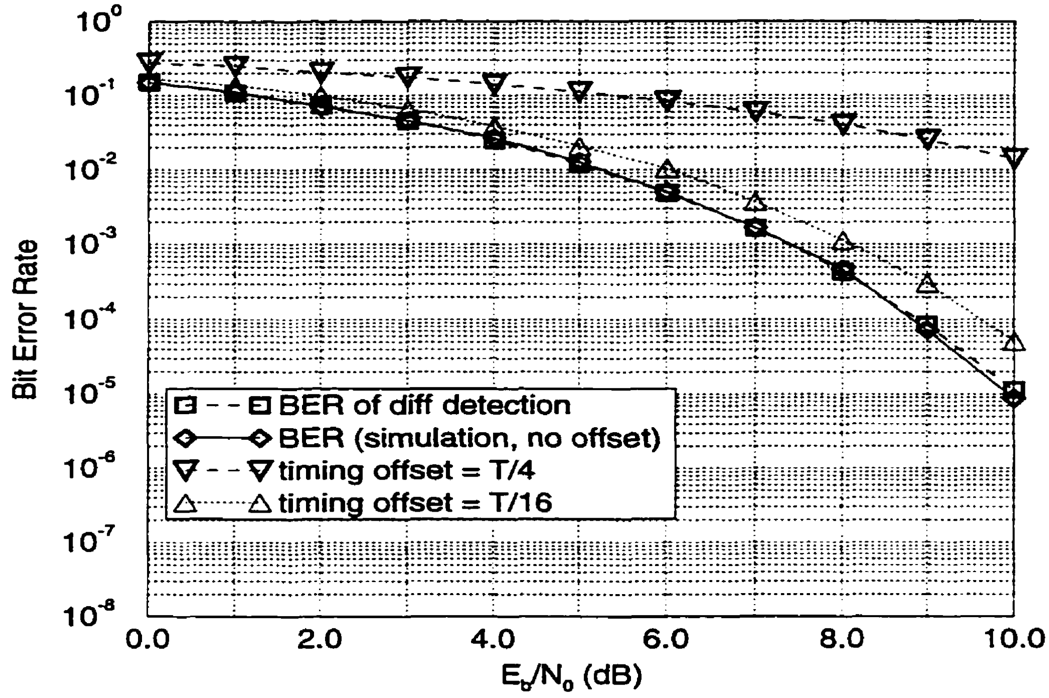

Figure 6.34: Operational BER in Uplink

satellite demodulator.

6.4.4 Complete System Simulation

The downlink and the uplink simulations are now discussed together to study the interaction between the uplink and the downlink. This is important because the uplink clock is coupled with the recovered downlink signal. The complete system operates as in the flow chart in Fig. 6.29 and as discussed in point form on page 148.

The interactions between the downlink and the uplink is revealed by Fig. 6.35, in which, the effect of the downlink SNR on the on–board estimate of the uplink signal amplitude is shown. In fact, it is the stability of the recovered clock that affect the timing performance of the uplink route. The stability of the recovered clock is then a dependent of the downlink SNR. To simulate this process, the correction of any timing offset of the uplink is *disabled* because the pdf of the estimate of a fixed timing offset is going to be studied. It is worth-

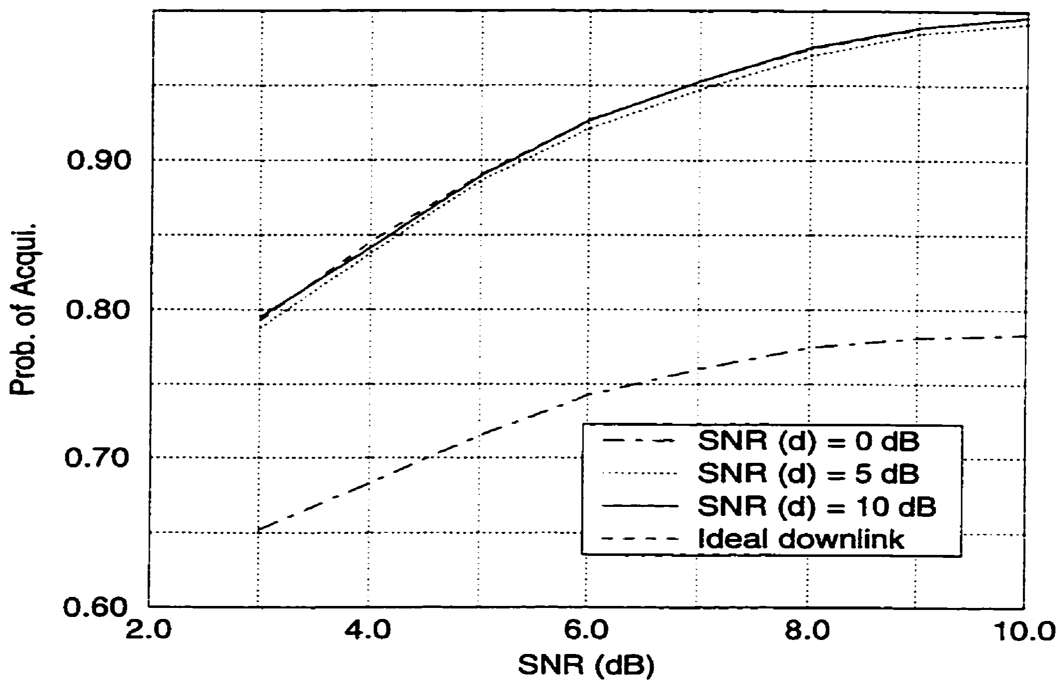

Figure 6.35: Interaction of Downlink and Uplink

while to note that though any change of the recovered downlink clock phase is passed to the uplink, the timing jitters are smoothed by the delay estimator because of the lowpass nature of the estimator.

In the simulation, the estimate is obtained from 100 uplink symbols. When the downlink SNR is 10 dB, the probability vs. SNR (uplink) is very close to the one shown in Fig. 6.13, where an ideal downlink (SNR $= \infty$), and therefore perfectly recovered clocks, is assumed. When the downlink SNR is 5 dB, the algorithm still provides good performance which is close to the ideal downlink case with less than 0.1 dB uplink SNR penalty can be noted in Fig. 6.35. But when the downlink SNR drops to 0 dB, the amplitude estimate can not yield correct signal amplitude estimate with sufficiently large probability. However, this level of SNR is not practical for a satellite system.

As illustrated in Fig. 6.14, a larger timing offset has negative effect on the proper magnitude estimation. A similar effect is noticed in Fig. 6.36 when the downlink clock is coupled with the uplink clock. Figures 6.35 and 6.36 show that though the uplink SNR is very important for the correct estimation of the uplink timing offset, an unstable recovered

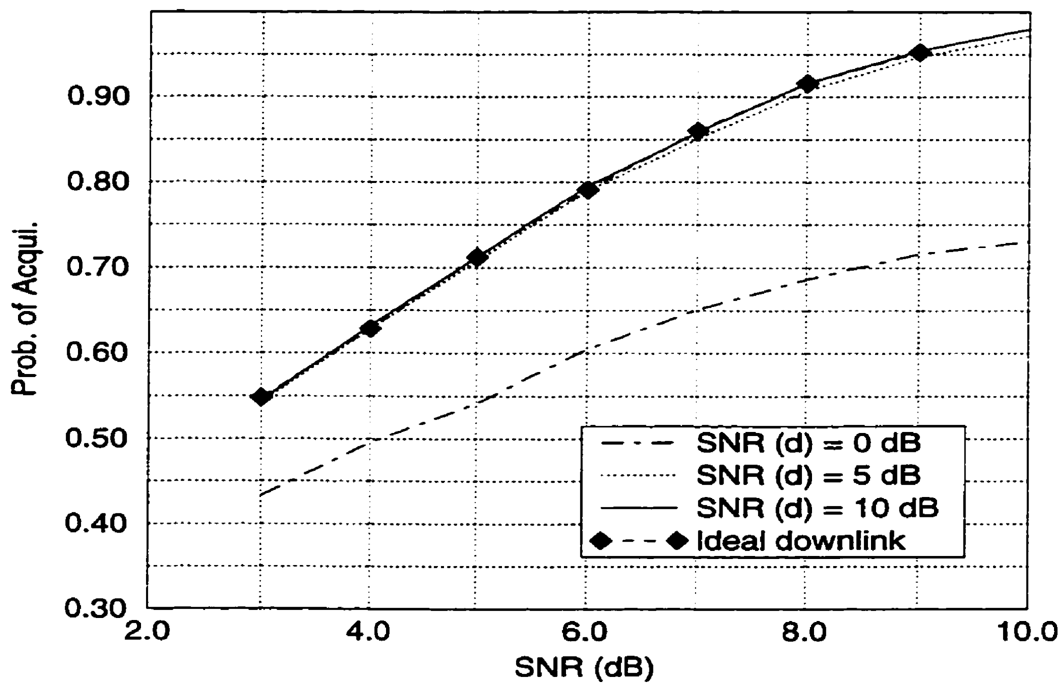

Figure 6.36: Large Offset reduces Efficiency

downlink clock will cause severe uplink performance degradation. From the simulation a downlink SNR larger than 5 dB is necessary to maintain the probability of making correct estimation of the uplink timing offset. With lower than 5 dB SNR in the downlink, the uplink timing offset can not be estimated efficiently using the algorithms presented in this thesis because of the excessive timing jitter in the recovered downlink clock.

Now Fig. 6.36 is compared with Fig. 6.35. It is easy to conclude that if the downlink SNR is larger than 5 dB and the uplink operating SNR larger than 8 dB, a 100–symbol probing sequence will provide a good estimate of the uplink timing offset using the algorithm presented in section 5.2.2 of Chapter 5. To be able to use lower SNRs in the uplink, a longer probing sequence is required. The performance given here is obtained during the process of link synchronization. This means that the recovered downlink clock has larger jitter than in the normal operation. Larger jitter in the downlink causes degradation of the performance of the uplink timing offset estimation. Larger jitter in the recovered downlink clock is introduced in the simulation with wider bandwidth (BW=1000Hz) of the loop filter of the timing recovery loop. The performance in terms of probability of the correct estima-

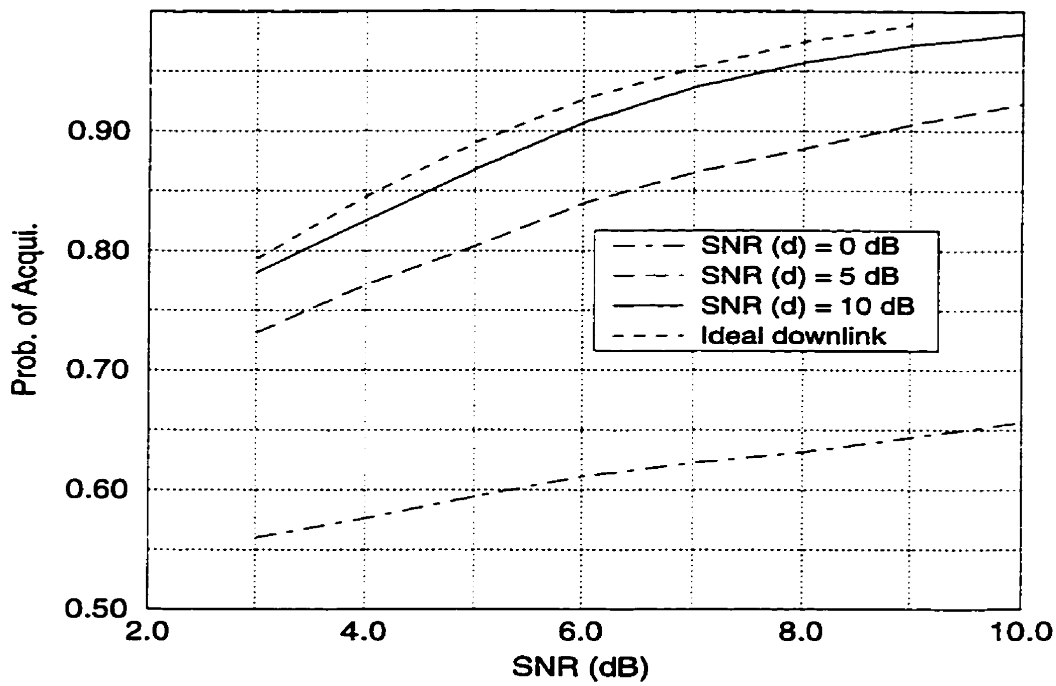

Figure 6.37: Wider Timing Loop BW degrades Uplink Estimation

tion with this bandwidth is given in Fig. 6.37. Compare the results in this figure with that in Fig. 6.35, where some degree of performance degradation for all the downlink SNRs, especially for the lower downlink SNRs, can be observed. The acquisition performance is evaluated in terms of the mean square error of the timing estimate as a function of probing sequence length with one–time correction can be found in Fig. 6.12 where the operating SNR is 10 dB. With the downlink SNR > 5 dB and the uplink SNR > 8 dB, one can expect the similar acquisition performance. No further simulation is necessary for the acquisition since the parameters have already been determined in the above discussion.

To obtain the BER performance, a complete system with initial carrier and timing offset is simulated. In the simulation, the timing offset in the uplink is originally set to $T/4$ with a multiple integer of T being ignored. Other timing errors will also be estimated using the delay estimate algorithm and hence be compensated on the uplink timing. The BER curve obtained here is for the case when timing is fully compensated by the estimation algorithm. The on–board estimator based on the DSAM successfully estimates this offset. The estimated amplitude is passed onto the ground terminal. The ground terminal receives

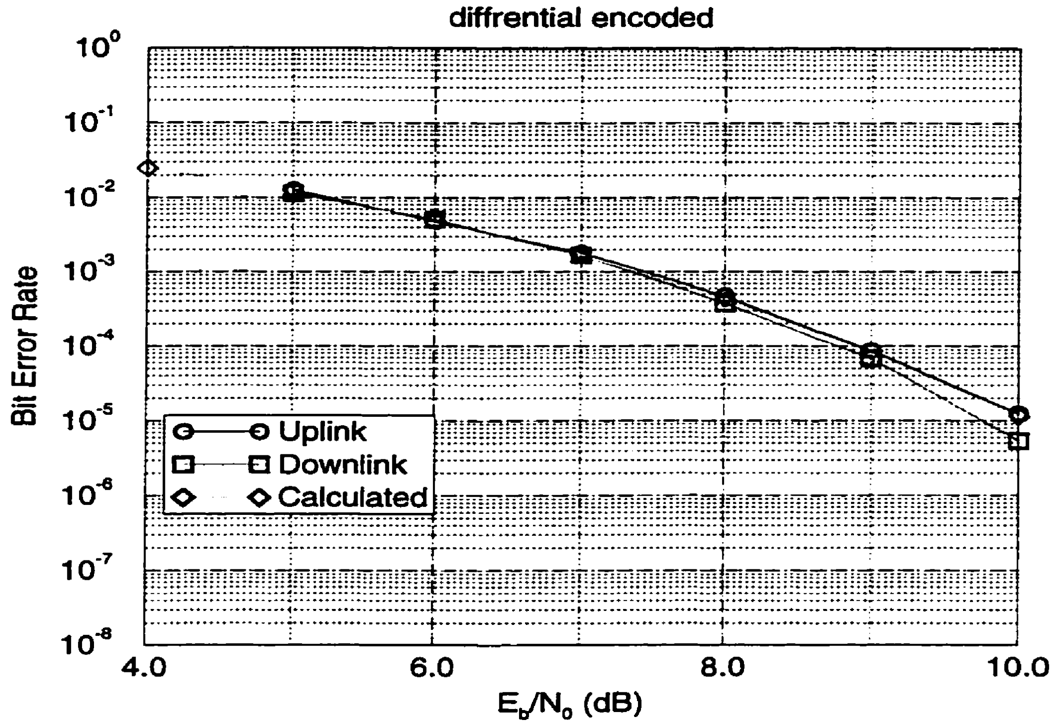

Figure 6.38: System Bit Error Rate for both Links

this information and adjusts the uplink clock phase using this information. Another round of timing offset estimate confirms the adjustment of clock phase of the ground terminal. The BER tests start after synchronization is declared. During the BER test, the satellite downlink signal source does not send uplink signal amplitude information. Therefore, no further uplink timing offset estimation is performed. During this BER test, the downlink SNR is extended to a wider range. Also, a wider range of SNRs are used in uplink BER tests. The same SNR applies to the downlink and the uplink for each test. The recovered downlink clock is stable for the whole testing period.

Fig. 6.38 shows the simulated BER performance of both the uplink and the downlink. The calculated BER is obtained from (6.19). Comparing this figure with the previous figures, figures 6.33 and 6.34, it is clear that the system performance is almost identical to those independent subsystems after the uplink and the downlink are coupled together for the purpose of synchronization. Frame–by–frame delay estimation is not necessary because of the discrete nature of this delay estimation algorithm when timing offset is a small fraction of the symbol period, it can not be picked up from the estimation. It is worthwhile to indicate that during the BER tests, any timing jitter in the recovered downlink clock is passed onto the uplink and these jitters will slightly increase the uplink BER. This conclusion is justified by Fig. 6.38 where all the uplink BERs are always slightly higher than the downlink BERs.

6.5 Summary

In this chapter, the sub–systems of a regenerative communication satellite system were simulated first. A complete system model then was simulated to study the interaction between a ground terminal and the processing satellite. The timing estimation results were compared with the theoretical ones given in Chapter 5 and the BER of both links under the normal operation condition were obtained.

Chapter 7

Conclusions

This chapter presents a summary of previous chapters. Conclusions are also given. Finally, possible further work on the uplink delay estimation of the processing satellite system is outlined.

7.1 Summary

In Chapter 1, the advantages of using a processing satellite in the communication systems were explained. Satellite systems using different earth orbits are briefly compared. The geosynchronous orbit is chosen for the processing satellite system to be studied. The FDMA/TDM configuration is specified as the basic system access scheme and the methodology of using computer simulation as a testing tool for the theoretical analysis was presented.

Chapter 2 specified the ground terminals used in this processing satellite system. The new feature of such a terminal is that its uplink transmitter carrier and clock is controlled by the ground terminal receiver. These signals contain information from the system master clock which resides in the satellite.

The configuration of the communication payload of the processing satellite was described in Chapter 3. The considerations of how the different functions are arranged were explained in this chapter. The on–board processors using SAW devices were examined to facilitate the derivation of a possible approach to delay estimation methods.

Chapter 4 presented the fundamental theory developed in this thesis. The transmitter timing recovery concept was illustrated. This timing recovery mechanism is very useful when synchronization of received signals is required at the receiver before they enter the demodulator. Maximum likelihood estimation theory was also briefly reviewed. One of the two propagation delay estimation methods derived from the MLE theory in this thesis, namely delay estimation through BER monitoring, or the estimated probability method (EPM), was analyzed and simulated. EPM was proved to be possible approach to uplink delay estimation but it is not very efficient when the system SNR is relatively high.

In Chapter 5, variations of the ground terminal estimation and the on–board estimation of the detected uplink signal amplitude method (DSAM) were compared in terms of estimation accuracy. The on–board estimation approach was chosen as the one for detailed study because of its better acquisition performance. Different lengths of probing sequences and different number of quantization levels were compared in terms of the resulting pdfs of the estimated signal amplitudes. A four–bit quantizer was chosen as the compromise between required downlink bandwidth and estimation accuracy. One hundred symbols are considered sufficient as the probing signal length at an operating SNR of 10 dB. A much longer sequence is required for the EPM at the same SNR.

In Chapter 6, a complete simulation model of the processing satellite system discussed in previous chapters was presented. Individual functions in the block diagram of Fig. 6.1 were explained. The implementation problems and the performance of the individual functions were illustrated. The system initialisation process was given and the interactions between the downlink and the uplink were shown by computer simulation. The simulated BER performance was compared with the results of a theoretical analysis.

7.2 Conclusions

It is concluded that

1. The BER can be used as a timing error measurement on the satellite uplink. The amount of the offset can be estimated from this measurement when the on–board bit decision is solely related to the timing offset. The MLE principle applies to this estimation method. For higher SNRs, EPM can not be used efficiently.

2. An efficient propagation delay estimation method, which estimates the uplink detection amplitude, derived from MLE theory, was obtained for the AWGN environment. From Chapter 4, the EPM requires 1000 symbols to reach an acquisition probability of 0.5 while the DSAM requires only 100 symbol to reach a similar probability as shown in Fig. 5.11 with SNR = 5dB. With a higher SNR, the DSAM becomes far more accurate than the EPM as shown in Table 5.7.

3. On–board processing of the uplink signals, which uses non–coherent combining, to obtain an uplink signal power estimate was presented. The non–coherent combining allows timing recovery before the on–board carrier is recovered. The algorithm presented here does not require third party delay information for uplink synchronization.

4. The estimation method can be simulated in a complete processing satellite system. The probing signal with length of 100 symbols was proved workable by the simulation. A longer sequence must be used if probing signal power is restricted to a very low level in order to reduce the interference to other channels. The acquisition time is $100T \times 2$ seconds plus two round–trip delays between satellite and a ground terminal where T is the symbol period of the probing sequence. The second round estimate is used to confirm the initial timing estimate.

5. The amount of residual timing offset as the result of delay compensation from using the algorithm presented in this thesis depends on the number of the discrete clock

phases (number of samples) given in one symbol period. In the simulation, a $T/16$ time resolution was used. From the simulation, an offset within $T/16$ causes a 0.5 dB SNR penalty for BER = 10^{-4}.

6. A stable recovered downlink clock is essential in keeping the uplink delay estimation algorithms from failure as illustrated in section 6.4.4. This is because the uplink clock is controlled by downlink clock. Although in the simulation a downlink SNR of 10 dB is used, it was shown in Fig. 6.35, to maintain a jitter-free recovered downlink clock a low SNR of 5 dB can be used. Transmitter timing recovery is proved to be possible when a stable master clock is provided to the transmitter.

7. A fixed carrier phase offset in the uplink demodulation can be tracked by a subsequent PLL but the carrier frequency of the uplink signal must be synchronized since any remaining offset in frequency is regarded as designed offset of the FDMA uplink. System performance may suffer from this frequency offset. Simulation included the fixed phase offset recovery for the uplink and fixed frequency offset recovery for the downlink. The uplink carrier frequency offset was assumed to be zero in the system simulation.

7.3 Suggestions for Future Work

Several topics related to this project could be studied in the future.

1. Use of a DSP implementation for the sub–systems in the overall system is required to find the effect of word length required for the component implementations. The computer simulation in this thesis uses floating point numbers for the most part. The fixed point simulation would be a closer one to the real digital implementation when the restricted word length is considered.

2. A fading channel should be considered since signal fading is inevitable for a mobile communication environment and therefore, a simple AWGN channel model is not good enough to describe the complete characteristics of the propagation path.

3. The windowing effect on the delay estimation algorithm should be examined more carefully because the current estimation algorithm is based on the non–windowing receiver and with the SNRs used in the simulation for initial synchronization, the ICI to other users might be high [35]. A windowed transform reduces ICI with a penalty of about 1 dB in SNR. It is expected that the algorithm presented here will work in a windowing environment but the relationship between timing offset and detected amplitude will not be linear [35]. Following the approach given in section 4.3.1 and using equations given in [35], one should be able to establish the relationship and use it for the purpose of delay estimate.

4. More realistic satellite and terminal models which include amplifier non–linearity and on–board filtering of input signals should be considered.

5. The effect of the coupling of recovered downlink carrier and uplink carrier should be studied because the proper relationship between the uplink carrier and the on–board frequency down converter must be established for correct MCD operation. The effect of imperfect downlink carrier recovery on the delay estimation algorithm should be studied.

6. The case of using a non–averaged on–board amplitude estimate should be further examined. This will reduce the on–board processor complexity and thus reduce the cost of the satellite.

Appendix A

Of Multiple Access

A.1 Multiple Access Schemes

The uplink access is based on FDMA in the whole thesis. A TDMA can be used on top of FDMA to further increase the system capacity. Multiple users with lower data rate share one frequency channel through the time multiplexing. The resulting FDMA channel data rate is not changed.

An example of such an FDMA/TDMA uplink scheme is shown in Fig. A.1. In this figure, it is assumed that four users, each with a data rate of 16Kbps, share one frequency channel, that is four users use f_i to access the satellite processor in sequence. Let one downlink TDM sub–frame represents one TDMA frame formed from the uplink FDMA channels, then the TDM frame contains four TDM sub–frames. This TDM frame, which contains all the users in the system, is four symbol period of the 64Kbps FDMA channel since the data rate of the users is four times lower than 64Kbps in this example. Each user occupies one time slot in this downlink frame. Relationship between the uplink users and the downlink frames is shown in Fig. A.2. In four consecutive TDM sub–frames, four users using the same FDMA channel occupy the corresponding time slots in each of the TDM sub–frames respectively. The #1 of u_j in Fig. A.2 indicates that this is the first symbol of

TDMA user j, where $j = 1, 2, 3, 4$, of the FDMA frequency f_i. Thus, each TDMA user must know its slot position in one of four TDM frames. Each downlink TDM frame represents one uplink FDMA/TDMA frame.

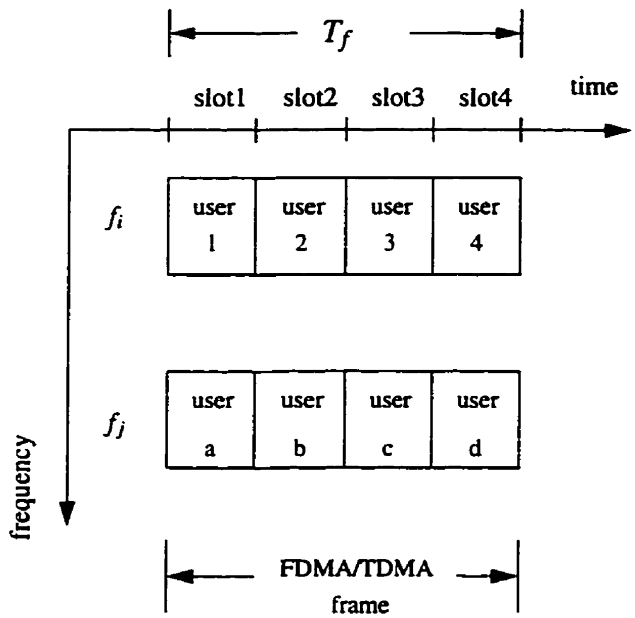

Figure A.1: FDMA/TDMA Uplink Scheme

In the FDMA/TDMA access case, users require only the same synchronization stability as for the FDMA access. This is a consequence that each TDMA user transmits at the peak rate of 64 kbps. The on–board demodulator is transparent to the nature of the uplink FDMA/TDMA access. Such users must only know their positions in the TDM frame shown in Fig. A.2. For geographically separated terminals sharing the same frequency through TDMA, the uplink propagation delays may be different. Also the carrier phase may not be the same for these TDMA users. Estimations must be performed on individual terminals when such a scenario applies. If all the delays of the accessing terminals are estimated at one time period, then a large memory is required on–board to keep all the information.

The delay estimation algorithm described in this thesis, though derived from pure FDMA uplink, is applicable to the hybrid FDMA/TDMA with only some minor changes.

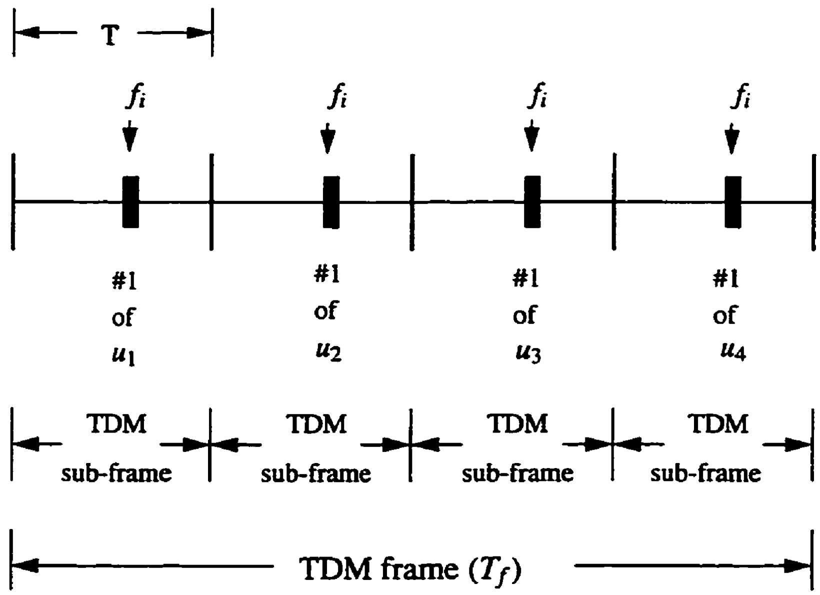

Figure A.2: TDMA Users in Downlink TDM Frame

The most significant change is the sampling of the uplink signal of a specific channel must be interleaved since individual channel does not appear in every uplink symbol period as TDMA is used. When the uplink signal is sampled properly, the delay estimation process described in this thesis can be used directly. As an example, consider Fig. A.2, if only samples from user 1 (u_1) are taken to perform timing offset estimate and the result is sent to u_1 then the process is exactly the same as described before. Users in other slots are untouched. It is possible to perform estimate on all users simultaneously if samples are stored on–board for this purpose.

Appendix B

Efficiency of the Delay Estimate from the Sample Bit Error (BER) Estimate

In this appendix a derivation of the CRB is given for the delay estimate in (4.55) when the estimate for the probability of error p is efficient. The concept was suggested and partially developed by one of the examiners of the thesis, Professor S. D. Blostein. It provides one explanation of why the BER estimate is inferior to the amplitude estimate for time delay given in Chapter 4.

Starting with (4.55) with the delay estimate denoted as $\widehat{D}$

$$\widehat{D} = |\lambda| = \frac{1 - KQ^{-1}(p)}{2} \equiv g(\widehat{p}) \tag{B.1}$$

where $K = \sigma/(A_k T)$ is a constant and $Q(x)$ is the Q function defined in (4.28). Recall that we have an efficient estimate of p, $\widehat{p}$, that satisfies the CR bound

$$\mathrm{Var}(\widehat{p}) = \frac{p(1-p)}{N}. \tag{B.2}$$

The estimate of D defined as a function of $\widehat{p}$ as given in (B.1) is an MLE due to the invariance property of MLEs [84]. Its variance, assuming $\widehat{D}$ is unbiased, is

$$\begin{aligned}
\mathrm{Var}(\widehat{D}) &\geq \frac{\left(\frac{dg}{dp}\right)^2}{-E\left\{\left[\frac{d^2 \ln p_{\mathbf{R}|A}(\mathbf{r}|a)}{da^2}\right]\right\}} \\
&= \left(\frac{dg}{dp}\right)^2 \mathrm{Var}(\widehat{p})
\end{aligned} \tag{B.3}$$

where $\mathrm{Var}(\widehat{p})$ from (B.2) is $p(1-p)/N$. Though it is noted that the estimate of $\widehat{D}$ is biased, it is still possible to evaluate the right hand side (RHS) of (B.3) to give a possible explanation of why the BER estimate is inferior to the amplitude estimate method given in Chapter 5. From (B.1), regarding $\widehat{p}$ as p,

$$\frac{dg}{dp} = -\frac{K}{2}\frac{d}{dp}Q^{-1}(p). \tag{B.4}$$

The above equation can be simplified as shown below.

From the definition of $Q(u)$ in (4.28),

$$Q'(u) = \frac{d}{du}Q(u) = -\frac{e^{-u^2/2}}{\sqrt{2\pi}}. \tag{B.5}$$

Since $u = Q^{-1}(p)$,

$$\frac{d}{dp}Q^{-1}(p) = \frac{du}{dp} \tag{B.6}$$

and as $Q(u) = p$,

$$\frac{dQ(u)}{dp} = 1. \tag{B.7}$$

By the chain law for the differentiation

$$\frac{dQ(u)}{dp} = \frac{dQ(u)}{du}\frac{du}{dp} \tag{B.8}$$

and hence, from (B.5) to (B.8)

$$\frac{d}{dp}Q^{-1}(p) = \frac{1}{Q'(u)}. \tag{B.9}$$

Therefore, from (B.4),

$$\frac{dg}{dp} = -\frac{K}{2}\frac{1}{Q'(u)}. \tag{B.10}$$

Use of (B.5) with the above equation, (B.10), one gets the result for the differentiation term in (B.4), when it is squred as

$$\left(\frac{dg}{dp}\right)^2 = \frac{K^2 \pi \exp(u^2)}{2}. \tag{B.11}$$

This is the multiplication factor on the CRB of $\widehat{p}$ for the lower bound to the variance of the estimate of D in (B.3). As $K = \sigma/(A_k T)$ and $\sigma^2 = N_0 T/2$ for the SAW processor, $K^2 = N_0/(2\overline{E}_k)$, where $\overline{E}_k = A_k^2 T$, the energy per symbol related to amplitude A_k at the SAW output. Thus in final form, as $u = Q^{-1}(p)$

$$\left(\frac{dg}{dp}\right)^2 = \frac{\pi N_0}{4\overline{E}_k}\exp([Q^{-1}(p)]^2) \tag{B.12}$$

and in (B.3)

$$\mathrm{Var}(\widehat{D}) \geq \frac{\pi N_0}{4\overline{E}_k}\exp([Q^{-1}(p)]^2)\,\mathrm{Var}(\widehat{p}). \tag{B.13}$$

As a minimum requirement, to get $\mathrm{Var}(\widehat{D}) \geq \mathrm{Var}(\widehat{p})$ in (B.13), where $\mathrm{Var}(\widehat{p})$ is the CR bound for $\widehat{p}$, the RHS of (B.12) should be set to unity. To get some numerical results, the following examples are considered. For $p = 1.35 \times 10^{-3}$, $Q^{-1}(p) = 3$ and it is found that $\overline{E}_k/N_0 \approx 38$dB to get $\mathrm{Var}(\widehat{D}) \geq \mathrm{Var}(\widehat{p})$. For $p = 10^{-2}$, 22 dB is required and for $p = 0.1$, the requirement is 6 dB. For all except the large value of $p = 0.1$, these are high values of SNR that are not practical in the satellite case. As such, this may partially explain why the BER method is inferior to the amplitude method to estimate uplink time delay in our application.

References

[1] T. E. Bell, "Telecommunications," *IEEE Spectrum*, vol. 31, no. 1, pp. 22–25, Jan. 1994.

[2] D. Larson, "Wireless technology: How test fits in," *Microwave Journal*, vol. 37, no. 1, no. 1, no. 1, pp. 63–86, 1994.

[3] V. O. K. Li and X. Qiu, "Personal communication systems (PCS)," *Proceedings of The IEEE*, vol. 83, no. 9, pp. 1210–1243, September 1995.

[4] B. Miller, "Satellites free the mobile phone," *IEEE Spectrum*, vol. 35, no. 3, pp. 27–35, March 1998.

[5] J. Ventura-Traveset, I. Stojkovic, F. Coromina, J. Benedicto, and F. Petz, "Key payload technologies for future satellite personal communications: A European perspective," *International Journal of Satellite Communications*, vol. 13, no. 1, pp. 117–135, Mar.–Apr. 1995.

[6] R. K. Jurgen, "Broadcasting with digital audio," *IEEE Spectrum*, pp. 52–59, March 1996.

[7] F. Davarian, "Earth–Satellite propagation research," *IEEE Communications Magazine*, vol. 32, no. 4, pp. 74–79, April 1994.

[8] M. Johnson, "Europe prepares for WRC–95: Mobile satellite service issues," *IEEE Communications Magazine*, vol. 33, no. 9, pp. 124–127, January 1995.

[9] S. Yoshida, "A digital coherent receiver suitable for land–mobile satellite communications," *IEEE Transactions on Vehicular Technology*, vol. 44, no. 4, pp. 771–778, November 1995.

[10] J. M. R. Salis and L. M. D. Rio, "Phase synchronization in a satellite–mobile channel," *International Journal of Satellite Communications*, vol. 13, pp. 1–10, Jan.–Feb. 1995.

[11] M. Shahid, S. K. Barton, and S. J. Shepherd, "A comparative study of nondata-aided symbol timing recovery techniques for digital satellite communications," *3rd European Conference on Satellite Communications*, pp. 160–164, November 1993.

[12] E. Del Re, "A coordinated European effort for the definition of a satellite integrated environment for future mobile communications," *IEEE Communications Magazine*, vol. 34, no. 2, pp. 98–104, February 1996.

[13] W. W. Wu, E. F. Miller, W. L. Pritchard, and R. L. Pickholtz, "Mobile satellite communications," *Proceedings of the IEEE*, vol. 82, no. 9, pp. 1431–1448, September 1994.

[14] A. J. Viterbi, "The evolution of digital wireless technology from space exploration to personal communication services," *IEEE Transactions on Vehicular Technology*, vol. 43, no. 3, pp. 638–644, August 1994.

[15] J. N. Pelton, "Space segment technologies for the 21st century: Key challenges for national satellite systems," *Conference Proceedings of ICC'91*, pp. 1103–1107, 1991.

[16] N. P. Secord and C. Loo, "Simulation study of an on–board satellite group demodulator based on the multistage transmultiplexer," *Conference Proceedings of Globecom'92*, pp. 717–721, 1992.

[17] C. R. Carter, "Survey of synchronization techniques for a TDMA satellite–switched system," *IEEE Transactions on Communications*, vol. COM–28, no. 8, pp. 1291–1301, August 1980.

[18] S. B. C. Molinari and G. Tartara, "On board demodulation in multicarrier TDMA satellite systems," *Conference Proceedings of ICC'88*, pp. 499–503, June 1988.

[19] F. Takahata *et al.*, "A PSK group modem for satellite communications," *IEEE Journal on Selected Area in Communications.*, vol. SAC-5, no. 4, pp. 648–661, May 1987.

[20] C. Loo and M. Umehira, "Performance estimation and design of group demodulator for satellite FDMA/TDM transmission," *Conference Proceedings of Globecom'89*, pp. 1110–1114, 1989.

[21] N. Zhang, "Global synchronization of a FDMA/TDM processing satellite communication system," Master's thesis, Queen's University, August 1992.

[22] D. R. Smith, *Digital Transmission Systems*. Van Nostrand Reinhold, 2nd ed., 1993.

[23] C. W. Sundberg and N. Seshadri, "Digital cellular systems for North America," *Conference Proceedings of Globecom'90*, pp. 533–536, 1990.

[24] K. B. Fielhauer, "Using RF channel simulators to test new wireless designs," *RF design*, no. 1, no. 1, pp. 56–60, 1994.

[25] N. Zhang, "A regenerative processing satellite system." Ph.D. proposal, Queen's University, May 1994.

[26] A. Malarky and M. Shaw, "SAW technology for on–board processing in military satellite communications," *Canadian Conference on Electrical and Computer Engineering*, pp. 28.2.1–28.2.4, September 1990.

[27] J. F. Purchase, "The new space race," *Via Satellite*, vol. X, no. 11, pp. 30–41, November 1995.

[28] A. Hills and D. B. Johnson, "A wireless data network infrastructure at Carnegie Mellon University," *IEEE Personal Communications*, vol. 1, pp. 56–63, February 1996.

[29] F. M. Gardner, "A BPSK/QPSK timing–error detector for sampled receivers," *IEEE Transactions on Communications*, vol. COM–34, no. 5, pp. 423–429, May 1986.

[30] K. K. M. Hung, "Design and test of a regenerative satellite transmultiplexer," Master's thesis, Queen's University, May 1993.

[31] T. T. Ha, *Digital Satellite Communications*. McGraw–Hill, Inc., 2nd ed., 1990.

[32] C. Loo and M. Umehira, "A note on chirp fourier transform and its application to group demodulation," *15th Biennial Symposium on Communications at Queen's University of Kingston*, pp. 172–175, May 1990.

[33] M. D. Shaw, N. D. J. Miller, and D. H. Warne, "SAW chirp filter technology for satellite on–board processing applications," *International Journal of Satellite Communications*, vol. 7, pp. 263–282, 1989.

[34] M. A. Jack, P. M. Grant, and J. H. Collins, "The theory, design, and applications of surface acoustic wave fourier-transform processors," *Proceedings of The IEEE*, vol. 68, no. 4, pp. 450–468, April 1980.

[35] N. P. Secord and C. Loo, "Analysis and measurement of timing error effects in a SAW–based group demodulator," *IEEE Transactions on Communications*, vol. 45, no. 10, pp. 1179–1182, October 1997.

[36] P. D. Santis and P. S. Yeung, "On–board demultiplexing of unrestricted FDMA traffic," *Proceedings of the 9th International Conference on Digital Satellite Communications*, pp. 327–334, May 1992.

[37] C. Loo and M. D. Shaw, "Performance analysis and measurement of a SAW–based group demodulator for on–board processing in communications satellites," *International Journal of Satellite Communications*, vol. 11, pp. 243–252, 1993.

[38] J. G. Proakis, *Digital Communications*. McGraw–Hill, 2nd ed., 1989.

[39] J. J. Spilker, Jr., *Digital Communications by Satellite*. Englewood Cliffs, New Jersey: Prentice–Hall, Inc., 1977.

[40] L. E. Franks, "Carrier and bit synchronization in data communication – a tutorial review," *IEEE Transactions on Communications*, vol. COM–28, no. 8, pp. 1107–1121, August 1980.

[41] H. L. Van Trees, *Detection, Estimation, and Modulation Theory*. Part I, John Wiley & Sons, Inc., 1968.

[42] Z. Sheng, *Probability and Statistics (in Chinese)*. ZheJiang Publishing House, 1979.

[43] J. Y. C. Cheah, "Frequency reference in VSAT," *IEEE Transactions on Communications*, vol. 42, no. 2/3/4, pp. 233–236, February/March/April 1994.

[44] C. A. Williams and P. T. Mathiopoulos, "Symbol timing recovery techniques for digital wireless personal telecommunication systems," *IEEE Pacific Rim Conference on Communications, Computers and Signal Processing*, vol. 1, pp. 64–67, 1993.

[45] S. Sheth and F. Harris, "Timing and carrier recovery techniques in dsp based digital receivers," *1994 IEEE MILCOM Conference Record*, vol. 2, pp. 639–643, 1994.

[46] N. C. Beaulieu and S. C. White, "A lower bound on the mean square error of symbol timing recovery for NRZ rectangular signals," *IEEE Transactions on Communications*, vol. 43, no. 7, p. 2183, July 1995.

[47] H. Meyr, M. Oerder, and A. Polydoros, "On sampling rate, analog prefiltering, and sufficient statistics for digital receivers," *IEEE Transactions on Communications*, vol. 42, no. 12, pp. 3208–3214, December 1994.

[48] J. W. M. Bergmans, "Efficiency of data-aided timing recovery techniques," *IEEE Transactions on Information Theory*, vol. 41, no. 5, pp. 1397–1408, September 1995.

[49] K. Kiasaleh and W. Lindsey, "Time and frequency transfer between master and slave clocks," *IEEE Transactions on Communications*, vol. COM–38, no. 10, pp. 1900–1912, Oct 1990.

[50] H. Meyr and G. Ascheid, *Synchronization in Digital communications*, vol. 1. John Wiley & Sons, Inc., 1990.

[51] R. D. Gaudenzi, T. Garde, and V. Vanghi, "Performance analysis of decision–directed maximum–likelihood phase estimators for M–PSK modulated signals," *IEEE Transactions on Communications*, vol. 43, no. 12, pp. 3090–3100, December 1995.

[52] G. Karam, I. Jeanclaude, and H. Sari, "A reduced–complexity frequency detector derived from the maximum–likelihood principle," *IEEE Transactions on Communications*, vol. 43, no. 10, pp. 2641–2650, October 1995.

[53] L. E. Miller and J. S. Lee, "Error analysis of time delay estimation using a finite integration time correlator," *IEEE Transactions on Acoustics, Speech and Signal Processing*, vol. ASSP–29, no. 3, pp. 490–496, June 1981.

[54] M. Wax, "The estimate of time delay between two signals with random relative phase shift," *IEEE Transactions on Acoustics, Speech and Signal Processing*, vol. ASSP–29, no. 3, pp. 497–501, June 1981.

[55] K. Anvari, "An algorithm for combined receiver sample timing and frequency offset estimation," *RF design*, no. 3, no. 3, pp. 30–45, 1994.

[56] W. C. Lindsey and W. C. Hagmann, "Network synchronization," *Proceedings of The IEEE*, vol. 73, no. 10, pp. 1445–1467, October 1985.

[57] W. C. Y. Lee, *Mobile Communications Design Fundamentals*. John Wiley & Sons Inc., 2nd ed., 1993.

[58] J. E. Padgett, C. G. Günther, and T. Hattori, "Overview of wireless personal communications," *IEEE Communications Magazine*, vol. 33, no. 1, pp. 28–41, January 1995.

[59] A. J. Viterbi, "A vision of the second century of wireless communication," *Microwave Journal*, vol. 38, no. 10, pp. 64–72, October 1995.

[60] P. W. Baier, P. Jung, and A. Klein, "Taking the challenge of multiple access for third–generation cellular mobile radio systems — a European view," *IEEE Communications Magazine*, vol. 34, no. 2, pp. 82–89, February 1996.

[61] P. P. Nuspl *et al.*, "Synchronization methods for TDMA," *Proceedings of The IEEE*, vol. 65, no. 3, pp. 434–444, March 1977.

[62] P. Robertson, "A generalized frame synchronizer," *Conference Proceedings of Globecom'92*, pp. 365–369, 1992.

[63] N. Celandroni, E. Ferro, *et al.*, "Design and implementation of a flexible, software based TDMA system," *Conference Proceedings of Globecom'92*, pp. 693–699, 1992.

[64] F. Ananasso and E. Del Re, "Clock and carrier synchronization in FDMA/TDM user–oriented satellite systems," *Conference Proceedings of ICC'87*, pp. 1473–1477, June 1987.

[65] F. Ananasso and G. Pennoni, "Clock synchronous multicarrier demodulator or multi–frequency TDMA communications satellite," *Conference Proceedings of ICC'90*, pp. 1059–1063, April 1990.

[66] P. T. Traynor, "SAW – based joint group demodulation of frequency shift keyed and differential phase shift keyed signals," Master's thesis, Queen's University, March 1990.

[67] C. Loo, "Performance analysis of a SAW based group demodulator for on–board processing communications satellites," *Conference Proceedings of Globecom'89*, pp. 1351–1354, 1991.

[68] C. Loo, "Performance analysis of SAW–based group demultiplexer for on–board processing communications satellites," *IEEE Transactions on Communications*, vol. 41, no. 7, pp. 1112–1116, July 1993.

[69] F. Ananasso, "Review of SAW devices and their signal processing applications in space communications," *International Journal of Satellite Communications*, vol. 7, pp. 231–262, 1989.

[70] P. M. Bakken and A. Ronnekleiv, "SAW–based chirp Fourier transform and its application to analogue on–board signal processing," *International Journal of Satellite Communications*, vol. 7, pp. 283–293, 1989.

[71] N. Zhang and P. J. McLane, "Global synchronization of a FDMA/TDM processing satellite communication system," *1993 Canadian Conference on Electrical and Computer Engineering*, pp. 417–423, 1993.

[72] J. G. Proakis and D. G. Manolakis, *Introduction to Digital Signal Processing*. Macmillan, 1st ed., 1988.

[73] M. K. Simon, "Nonlinear analysis of an absolute value type of an early–late gate bit synchronizer," *IEEE Transactions on Communications Technology*, vol. COM–18, no. 5, pp. 589–596, Oct 1970.

[74] B. Koblents, "Asynchronous timing recovery in m-PSK mobile satellite modems," Master's thesis, Queen's University, July 1992.

[75] A. N. D'Andrea and M. Luise, "Optimization of symbol timing recovery for QAM data demodulators," *IEEE Transactions on Communications*, vol. 44, no. 3, pp. 399–406, March 1996.

[76] A. E. Payzin, "Analysis of a digital bit synchronizer," *IEEE Transactions on Communications*, vol. COM–31, no. 4, pp. 554–560, April 1983.

[77] A. Papoulis, *Probability, Random Variables, and Stochastic Processes*. McGraw–Hill, 2nd ed., 1984.

[78] S. Ross, *A First Course in Probability*. Macmillan Publishing Company, 3rd ed., 1988.

[79] W. H. Tranter and K. L. Kosbar, "Simulation of communication systems," *IEEE Communications Magazine*, vol. 32, no. 7, pp. 26–35, July 1994.

[80] K. S. Shanmugan, "Simulation and implementation tools for signal processing and communication systems," *IEEE Communications Magazine*, vol. 32, no. 7, pp. 36–40, July 1994.

[81] B. D. Woerner, J. H. Reed, and T. S. Rappaport, "Simulation issues for future wireless modems," *IEEE Communications Magazine*, vol. 32, no. 7, pp. 42–53, July 1994.

[82] R. W. Kerr, "Coherent detection of interleaved cpfsk on various shadowed mobile satellite channels," Master's thesis, Queen's University, August 1989.

[83] F. M. Gardner, *Phaselocked Techniques*. John Wiley & Sons, Inc., 2nd ed., 1979.

[84] S. Kay, *Fundamentals of Statistical Signal Processing: Estimation Theory*. Prentice–Hall, Inc., 1993.

IMAGE EVALUATION TEST TARGET (QA-3)

150mm

6"

APPLIED IMAGE, Inc
1653 East Main Street
Rochester, NY 14609 USA
Phone: 716/482-0300
Fax: 716/288-5989